PhD School in Physics and Astrophysics
PhD thesis
Cycle XXXVIII

Optical Quantum Communication for power systems and smart grids

Supervisor	**Prof. Alessia Allevi**
Co-supervisor	**Dr. Marco Lamperti**

PhD Candidate	Silvia Cassina

October 30, 2025

University of Insubria
Department of Science and High Technology

E per tutti i ragazzi e le ragazze
Che difendono un libro, un libro vero
Così belli a gridare nelle piazze
Perché stanno uccidendo il pensiero
...
Perché le idee sono come farfalle
Che non puoi togliergli le ali
Perché le idee sono come le stelle
Che non le spengono i temporali
Perché le idee sono voci di madre
Che credevano di avere perso
E sono come il sorriso di dio
In questo sputo di universo

– Roberto Vecchioni

Introduction

In the last century, electrical power systems have become more and more complex. Nowadays, they do not only allow the power supply to the final users. In fact, the implementation of smart grids allows to share consumption data as well, so that the power supply can adapt to the user's exact requirements, reducing waste.

Such a modernization raises the bar of the demanded performance such as ultra-low latency, high reliability, and robust protection against interference and cyber-attacks, since the energy resources are distributed according to a real-time monitoring.

In this context, optical quantum communication represents a very powerful resource to fulfill the security requirements thanks to the possibility to exploit quantum states of light and intrinsic physical security (e.g., the no-cloning theorem) in the already available fiber-optic infrastructure. In particular, the use of coherent states has been demonstrated to be a suitable solution thanks to the fact that they are easy to generate and robust to propagation losses.

In recent years, several quantum communication technologies have been developed. We recall integrated quantum photonic platforms supporting quantum key distribution (QKD) and quantum networking which are advancing towards real-world deployment. [1]

These technologies might be based on different detection solutions, such as single-photon detectors (giving access to the so-called discrete variables) [2] or interferometric schemes, of which the most famous is the standard homodyne detector (that allows to encode and decode on continuous variables) [3]

Recently, the capability to resolve photon numbers has attracted researchers' interest because it gives access to more sophisticated measurement schemes beyond simple "click/no-click" detectors. [4]

This thesis presents a proof-of-principle experimental investigation into a homodyne-like quantum receiver for optical communication, finally aimed to be integrated into power-system environments. In particular, this device is based on photon-number-resolving (PNR) detectors, namely Silicon Photomultipliers (SiPMs)[5]. Unlike standard homodyne

---

[1] [1] Wei Luo et al., *Light: Science & Applications*, p. 175 (12), (2023)

[2] [2] Thu Ha Dao et al., , p. 8 (vol. 12), (2024)

[3] [3] Stefano Pirandola et al., *Advances in optics and photonics*, pp. 1012–1236 (12), (2020)

[4] [4] Jan Provazník et al., *Opt. Express*, pp. 14839–14849 (28), (2020)

[5] [5] Silvia Cassina et al., *EPJ Quantum Technology*, p. 4 (8), (2021)

detection (which uses a strong local oscillator and linear photodiodes to measure continuous quadratures), the proposed scheme exploits the discrete nature of PNR outputs to access phase information via the photon-number difference at the two output ports of a balanced interferometer. Previous theoretical work has shown that PNR-based receivers can outperform standard homodyne detection in certain regimes, such as in hybrid QKD protocols using coherent states. [6]

The contributions of this thesis are listed below by chapter content.

- *Chapter 1* Theoretical introduction, to give the reader the basic concepts behind the experimental work.
- *Chapter 2* Implementation and characterization of a hybrid homodyne-like receiver with SiPMs as PNR detectors and application to a Binary Phase-Shift Keying (BPSK) modulation scheme. In this chapter, the quantitative evaluation of the mutual information between sender and receiver under controlled channel losses is presented, including the comparison with a simulated standard homodyne detector with matching parameters. Finally, a security analysis under the wiretap channel model, considering both individual and collective eavesdropping attacks, and assessing secret key generation rates under direct and reverse reconciliation, is performed.
- *Chapter 3* Upgrade of the Chapter 2 setup to generate a four-phase shift. Characterization of the limit of our technology in terms of phase noise. In this chapter, a first quantitative evaluation of the mutual information as a function of losses is presented, in comparison with BPSK and simulated standard homodyne with matching parameters.
- *Chapter 4* Investigation of wavelength compatibility with telecom fibers (C-band around 1550 nm) via an up-conversion stage that transfers the signal into the visible (∼ 620 nm) region for detection by SiPMs, while preserving photon-number statistics and phase information.
- *Chapter 5* The content of this chapter is not compliant with the rest of the thesis, since it contains the results obtained during the six-month period in Nice. In the InPhyNi laboratories I worked on the characterization of the quantum correlations of frequency combs generated in a silicon nitride micro-ring resonator at different intensity regimes.

In the context of smart grids, the integration of such quantum optical receivers is of relevant interest, in particular because the chosen detectors (SiPMs) are not sensitive to high-intensity magnetic fields. This opens the door to secure optical communication links between substations, control centers, and distributed resources. By combining PNR detection with a homodyne interferometric architecture, this work links continuous-variable quantum optics and photon-counting technologies. In a future perspective, this offers a practical solution to implement quantum-communication nodes for power systems.

---

[6] [6] Marco Cattaneo, Matteo G. A. Paris, and Stefano Olivares, *Phys. Rev. A*, p. 012333 (98), (2018)

The results demonstrate that the PNR-based homodyne-like receiver can achieve mutual information values comparable to the conventional homodyne detector when the local oscillator is sufficiently strong and the overlap visibility is controlled. Moreover, the up-conversion approach ensures compatibility with telecom wavelengths without sacrificing phase or photon-number fidelity. These outcomes support the suitability of such a compact, cost-effective quantum receiver based on SiPMs for power-system applications, even though there is some required optimization to achieve this final goal.

Contents

1 Theoretical background

This chapter is meant to introduce the reader to all the theoretical and experimental tools that are considered to be of use to understand this work. Even though this is an experimental project, some outlines of theory are given to better understand the procedure and the results. Among the exposed subjects, coherent states and their representation in the quadrature space have a fundamental role, as well as homodyne detection and our detection scheme based on photon-number-resolving (PNR) detectors. Moreover, a few pages will be dedicated to the description of Silicon Photomultipliers, the PNR detectors that have been exploited in all the experimental works reported in the further chapters. Finally, a short introduction of the nonlinear phenomena performed in the experiment is reported.

1.1 Outlines of Quantum Optics and Information Theory

1.1.1 Quantum optics

Quantum Optics is a branch of Quantum Mechanics, in which the electromagnetic field that typically represents light is not described as a continuous wave but as a non-classical object. The procedure of field quantization can be easily found in

---

[0] Background photo: Como Lake seen from Passeggiata Gelpi.

any Quantum Optics manual (I report here the textbook used in the lectures I followed [1]). Nevertheless, for the sake of clarity, here the main results are reported. The Hamiltonian description of the field is that of a harmonic oscillator

$$\hat{H} = \hbar\omega \left(\hat{a}^\dagger \hat{a} + \frac{1}{2} \right)$$

and its eigenstates are the so-called Fock States. Indeed, Fock states are the eigenstates to the Number operator $\hat{N} = \hat{a}^\dagger \hat{a}$, where $\hat{a}^\dagger$ and $\hat{a}$ are the creation and annihilation operators respectively, such that:

$$\hat{a}|n\rangle = \sqrt{n}|n-1\rangle$$

$$\hat{a}^\dagger|n\rangle = \sqrt{n+1}|n+1\rangle$$

$$[\hat{a}, \hat{a}^\dagger] = 1$$

$\hat{a}^\dagger$ and $\hat{a}$ are not self-adjoint operators.

1.1.2 Quadratures description

Starting from the creation and annihilation operators it is possible to define the quadrature operators,

$$\hat{X} = \hat{a} + \hat{a}^\dagger$$

$$\hat{P} = \frac{\hat{a} - \hat{a}^\dagger}{i}$$

$$[\hat{X}, \hat{P}] = 2i$$

Let's remark that $\hat{X}$ and $\hat{P}$ are self-adjoint operators, therefore physical observables. We can consider them like the dimensionless interpretation of the classical position and momentum, respectively. A system like this may require an infinite-dimensional Hilbert space to be described, for this reason they are called Continuous Variables (CV), and the spectrum of $\hat{X}$ and $\hat{P}$ is continuous.

1.1.3 Coherent states

Since the whole communication protocol described in this thesis is based on coherent states, here is a brief description of these states and their generation.

[1] [7] Cristpher C. Gerry and Peter L. Knight, *Cambridge University Press*, (), (2004)

Coherent states are considered to be quasi-classical states. They are the eigenstates of the annihilation operator

$$\hat{a}|\alpha\rangle = \alpha|\alpha\rangle \qquad \alpha \in \mathbb{C}$$

They are non-orthogonal states, meaning that their discrimination can be difficult; this is one of the reasons why they are considered to be suitable for quantum communication. Another reason is that they are very robust against losses and easy to generate in laboratory, since a laser beam is typically a coherent state.

The photon-number distribution of coherent states is Poissonian

$$P(n) = \frac{|\alpha|^{2n}}{n!} e^{-|\alpha|^2}$$

where the mean value is $|\alpha|^2$ and the variance is $\Delta^2 n = |\alpha|^2$. The last term represents the shot noise, namely intensity fluctuations due to the intrinsic quantum nature of light.

Coherent states can be propagated on the basis of Fock states

$$|\alpha\rangle = e^{\frac{-|\alpha|^2}{2}} \sum_{n=0}^{\infty} \frac{\alpha^n}{\sqrt{n!}} |n\rangle = e^{\frac{-|\alpha|^2}{2}} e^{\alpha \hat{a}^\dagger} |0\rangle$$

From this propagation it is possible to define the displacement operator $\hat{D}(\alpha) = e^{\frac{-|\alpha|^2}{2}} e^{\alpha \hat{a}^\dagger}$ such that $\hat{D}^{-1}(\alpha) = \hat{D}(-\alpha)$ that describes coherent states as displaced vacuum states, as is shown in Figure 1.1.

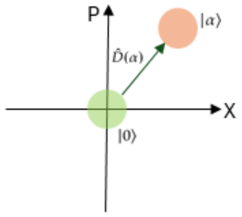

Figure 1.1: Displacement of the vacuum state to generate a coherent state.

1.1.4 Information Theory

A message is something that is used to code and share information, that can be a text, a sound, an image and so on. It might seem counterintuitive but the amount of information contained in a message is related to its uncertainty and randomness [2] [3] [4]. We can state that the subjects of information theory are random variables.

Going more into details, a message is composed of several fundamental units that hereon will be called A. We define as an alphabet ($\mathcal{A}$) the finite-dimensional ensemble of values a that A can take; $\mathcal{A} = \{1, \ldots, k\}$, each one with a certain probability $p_A(a)$

$$p_A(a) := p(a = A), \qquad a \in \mathcal{A}$$

2: [8] Thomas M. Cover and Joy A. Thomas, *John Wiley & Sons Inc.*, (), (2005)

3: [9] Gianfranco Cariolaro, *Springer International Publishing*, (), (2015)

4: [10] Stefano Olivares, *https://sites.unimi.it/olivares/*, (), (2021) In this description, $p_A(a)$ forms a probability distribution

$$\forall a \in \mathscr{A}, p_A(a) \geq 0, \sum_{a \in \mathscr{A}} p_A(a) = 1$$

But how can we quantify the information carried by one symbol A? Let's make some considerations about the information.

First of all, it just depends on the alphabet dimension and not on the nature of the symbol, i.e. $\mathscr{A} = \{0, 1\}$ can code the same information as $\mathscr{A} = \{'\text{white}', '\text{black}'\}$ because they have the same dimension. Moreover, as we have already mentioned, information is related to the randomness of a symbol: if A is always repeated equal to itself, the outcome of its measurement is already known, so it does not bring much information. Conversely a symbol that appears rarely will bring much more information. According to this line of thought, we can state that the amount of information a symbol carries $I(a)$ decreases as its probability $p_A(a)$ increases. Information is a decreasing function of $p_A(a)$.

$$I(a) = f[p_A(a)]$$

In the particular case in which $p_A(a) = 1$, we have $I(a) = 0$, as well as, when $p_A(a) = 0$, we have $I(a) = 0$. Finally, if x and y are two different symbols, independent from each other, information obtained by the two symbols should be the sum of the information obtained by each one:

$$f[x \cdot y] = f[x] + f[y]$$

To match all these requirements, Shannon introduced a logarithmic function that describes information.

$$I(a) := -\log_2 p(a)$$

where the base two describes the use of a binary symbol.

If we consider the statistical mean of this information description, we obtain

$$H(a) = \sum_{a \in \mathscr{A}} p_A(a) I(a) = -\sum_{a \in \mathscr{A}} p_A(a) \log_2 p_A(a) \tag{1.1}$$

that is the well-known Shannon entropy, measuring the uncertainty before knowing the value of A. It can be interpreted as the uncertainty of the transmitted symbol as well as the information obtained after its value is known.

In the case of a binary symbol, the Shannon entropy becomes

$$H_{bin}(p) = -p\log_2(p) - (1-p)\log_2(1-p)$$

where p and $1-p$ are the probability of the two outcomes. Intuitively, we expect to have the maximum information when the two outcomes have the same probability $p = 1-p = \frac{1}{2}$. In Figure 1.2 is reported a numerical simulation of the value of H_{bin} as a function of p: the blue curve represents the entropy function while the green circle indicates the maximum of the function, that occurs when $p = 0.5$, as expected.

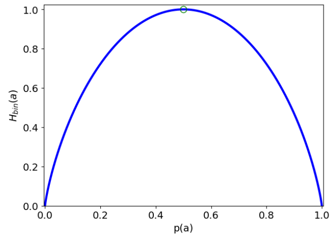

Figure 1.2: Simulation of binary entropy as a function of p.

Now that a generic description for information is given, let's consider two different random variables, X and Y. We want to know how the information on X is related to the information on Y. A graphic idea of the quantities that will be defined in the following lines is reported in Figure 1.3.

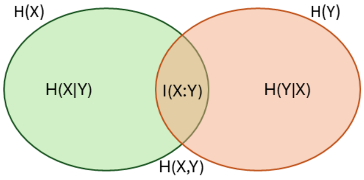

Figure 1.3: Graphic representation of mutual information.

The total entropy of the system, including both the variables, is defined as

$$H(X,Y) := -\sum_{x,y} p(x,y)\log_2(p(x,y))$$

and is called joint entropy.

If the outcome of Y is known while the one of X is not, the conditional entropy of X given Y is

$$H(X|Y) := H(X,Y) - H(Y) \tag{1.2}$$

This function gives a measurement of the uncertainty of X when Y is known. Finally, we want to define the information shared by the two variables, known as mutual information:

$$I(X:Y) := H(X) + H(Y) - H(X,Y) = H(X) - H(X|Y) \tag{1.3}$$

Since it is the information the two ensembles have in common, it must be the same for X and Y, so we can intuitively state that

$$I(X:Y) = I(Y:X)$$

so

$$H(X) - H(X|Y) = H(Y) - H(Y|X).$$

1.1.5 Communication channel and Holevo Bound

To perform communication, a sender, Alice, codes a message using an alphabet $\mathscr{A}$ and sends it through a channel to a receiver, Bob, that decodes the message using an alphabet $\mathscr{B}$. Both the alphabets are characterized by their symbol probability, respectively $p_A(a)$ and $p_B(b)$. The channel is also characterized by a certain transmittance probability p_C, so that

$$p_C = p(B = b|A = a)$$

In the case that the channel is noisy, there will be some uncertainty added to the input information. Let's define $I(A)$ as the *a priori* uncertainty on the input message and $I(A|B)$ the a posteriori uncertainty, meaning the residual uncertainty after Bob's decoding. The a posteriori uncertainty is described by the probability $p_{B|A}(b|a)$ that Bob's output is correct with respect to Alice's input, and the complementary probability $1 - p_{B|A}(b|a)$ that Bob obtains the wrong value. The information transmitted through the channel can be described as

$$\Delta I(A, B) = I(A) - I(A|B)$$

whose expectation values, as we have already seen, describe the information in terms of entropy.

$$I(A : B) = H(A) - H(A|B)$$

Conditional entropy can be interpreted as the loss introduced by the channel. In the case of a binary input {0,1 }, we can define a cross-transition probability δ, which represents the probability that the input signal flips during transmission $\delta = p(0|1) = p(1|0)$. Of course, $1-\delta$ represents the probability that the input does not flip. In this case, we can rewrite the conditional entropy as

$$H(A|B) = -\delta \log_2 \delta - (1 - \delta) \log_2 (1 - \delta)$$

Under the assumption of *a priori* equally probable symbols, $p_A(0) = p_A(1) = \frac{1}{2}$ we know that $H(A) = 1$, so

$$I(A : B) = 1 + \delta \log_2 \delta + (1 - \delta) \log_2 (1 - \delta)$$

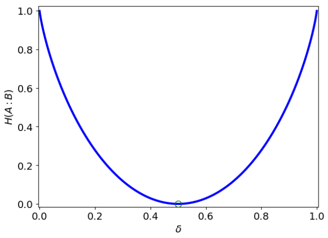

Figure 1.4: Graphic representation of $H(A : B)$ as a function of δ.

Also in this case, in Figure 1.4 is reported a simulation of the behavior of the mutual information as a function of the cross-over probability. Typically δ is considered to be fixed for a characterized channel. It is easy to observe that when $\delta = 0.5$ the mutual information decreases to zero, while the closer δ is to 0 or 1, the higher the mutual information. In general, the channel capacity is defined as the maximum mutual information that can be obtained on all the possible input probability

$$C := \max_{p_A} I(A : B)$$

As we have already mentioned, the mutual information depends on the measurements performed by Bob, and the maximum value that can be obtained through all the possible measures is named accessible information

$$H_{acc} := \max_{\{POVM\}} I(A : B)$$

But it is important to notice that this value is limited by the Holevo bound [5]

$$I(A : B) \leq \chi(A, B)$$

where $\chi(A, B)$ is the Holevo information between Alice and Bob. Its value depends on the considered quantum state. In this work these will be just coherent states.

1.1.6 Notions of Quantum Communication

In quantum communication the quantum states' properties are exploited to encode information. Even though there are some protocols that use entangled states, the most diffused schemes are based on non-commutative observables. In the case of continuous variables, these are the field quadratures. Among the several applications we will mention Quantum Key Distribution (QKD), that involves the use of a quantum channel to transmit a secret and secure key that the sender and receiver can use to decode a certain message. There are several security-proof protocols (such as BB84, E91, BBM92) whose detailed description can be easily found in the literature. Since in this work we limit to characterize the general suitability of our detector to QKD without introducing any specific protocol, here only a generic idea of the necessary steps is given[6].

- **State preparation** Alice prepares the state she wants

[5] [11] Alexander Semenovich Holevo, *Problemy Peredachi Informatsii*, pp. 3–11 (9), (1973)

[6] [12] Fabian Laudenbach et al., *Advanced Quantum Technologies*, p. 1870011 (1), (2018)

to send to Bob encoding information on the chosen alphabet. In the case of coherent states, she typically performs a Gaussian modulation.

- **Detection** Bob receives the state and measures the proper observable to obtain information. Typically, he has to choose between two variables that do not commute, so if he measures the one on which Alice has encoded information, he will more likely obtain the correct information, otherwise he has $\frac{1}{2}$ probability to get a correct measurement.
- **Sifting** using a classical channel the two parts delete the measurements performed on the wrong basis.
- **Parameter Estimation** the two parts select a random subset of the key and compare the outcomes. The subset will then be deleted from the key sequence. From this comparison they make an estimation of the channel noise, losses and mutual information. If the parameters do not match the standard for the protocol they are using, the channel is not considered secure because there may be a third part stealing information. In this case the communication is aborted.
- **Error Correction and Reconciliation** correction of the measurements performed. It is said to be direct in the case Bob corrects his bits according to Alice's prepared input, or reverse if it is Alice correcting her sequence according to Bob's measured output.
- **Confirmation** the two parts choose a hash function and check through an authenticated channel if they obtain the same output. If the hash values are different then the communication is not considered secure and will be aborted.

1.1.7 Notions of security and key generation rate

It has been mentioned in previous sections that the channel could be spied by a third part, an eavesdropper that we will call Eve. She has complete access to the quantum channel, so that she can manipulate and control it. On the other hand, she cannot intervene in the conversation between A and B, since they use an authenticated channel. Anyway, Eve can prepare ancilla states that can interact with the states sent by Alice, so that Eve can get some information as well. Let's also consider the idea that Eve could be provided with a quantum

memory that allows her to store the measured states.
Under this hypothesis there are three types of attack that she can perform to steal some information from the communication channel[7]:

- *Individual attack*
  In this case Eve performs a series of independent and identically distributed (i.i.d.) attacks, meaning that she prepares an ancilla state separately for each state that Alice sends to Bob. Then, she stores information so that she can measure the collected states separately after the sifting phase.
- *Collective attack*
  The procedure of this attack is similar to the individual one. Eve performs a series of i.i.d. attacks and stores the states in the quantum memory, but instead of performing several independent measurements, she makes an optimal collective measure of all the stored states after the post-processing phase.
- *Coherent attack*
  These are the most general attacks Eve can perform. In this case she does not make any i.i.d. attack, but she prepares a global optimal ancilla whose modes interact with the states sent by Alice. Again, she stores the unmeasured states in the quantum memory and performs a collective measure after the post-processing phase.

To better describe the communication between Alice and Bob it is important to introduce the mutual information between Alice and Eve, $I(A:E)$ in the case of direct reconciliation or the one between Bob and Eve, $I(B:E)$, in the case of reverse reconciliation. Another relevant quantity to be defined is the Key Generation Rate, which represents the useful secret information shared by Alice and Bob. It can be expressed as follows, in the case of direct and reverse reconciliation respectively.

$$\Delta I_{DR}(A:B) = I(A:B) - I(A:E)$$

$$\Delta I_{RR}(A:B) = I(A:B) - I(B:E)$$

In this work we have considered only individual and collective attacks. In the first scenario $I(A/B:E)$, namely Eve's gained information, has been calculated as the mutual information, while in the second case $I(A/B:E) = \chi(A/B:E)$

[7] [3] Stefano Pirandola et al., *Advances in optics and photonics*, pp. 1012–1236 (12), (2020)

information obtained by Eve corresponds to the Holevo information, namely the maximum amount of information that can be extracted from the ensemble of eavesdropper signals compatible with quantum mechanics laws.

1.2 Detection schemes

When dealing with field quadratures, a suitable detector that, in principle, enables to reconstruct the transmitted phase, must be able to collect information about the phase. Therefore, an interferometric scheme is required. The most common detector used in quantum CV communication protocols is the homodyne detector.

1.2.1 Homodyne Detector

A schematic representation of the detection scheme is shown in Figure 1.5, where an intense coherent field, usually called Local Oscillator (LO), is mixed at a beam splitter (BS) with another optical state (in our case another coherent state)[8] [9] [10]. The mentioned BS should be balanced, meaning that light is transmitted or reflected with the same probability ($\tau = 0.5$). Moreover, to have a proper overlap, the LO is supposed to have the same wavelength and spatio-temporal profile as the second input state. The evolution through the BS is given by

$$a \longrightarrow \hat{U}^\dagger a \hat{U} = \frac{\hat{a} + \hat{b}}{\sqrt{2}} \equiv \hat{c}$$

$$b \longrightarrow \hat{U}^\dagger b \hat{U} = \frac{\hat{b} - \hat{a}}{\sqrt{2}} \equiv \hat{d}$$

where $\hat{U}$ is the BS evolution operator. The detectors placed in c and d will respectively receive $\hat{N}_1 = \hat{c}^\dagger \hat{c}$ and $\hat{N}_2 = \hat{d}^\dagger \hat{d}$, so that $\hat{N}_1 - \hat{N}_2 = \hat{a}^\dagger \hat{b} + \hat{b}^\dagger \hat{a}$. The LO is a coherent state, meaning $|\beta\rangle\langle\beta|$, $\beta = |\beta| e^{i\theta}$, and the signal is a generic state ρ, then

$$\langle \hat{N}_1 - \hat{N}_2 \rangle = \mathrm{Tr}[\rho \bigotimes |\beta\rangle\langle\beta| (N_1 - N_2)] = \beta\, \mathrm{Tr}[\rho x_\theta] = \beta \langle x_\theta \rangle$$

where x_θ is a generic field quadrature. The measurement of the output difference is related to the quadrature value. Experimentally, the only accessible measurements correspond

---

[8] [13] Frédéric Grosshans and Philippe Grangier, *Phys. Rev. Lett.*, p. 057902 (88), (2002)

[9] [14] Stefano Olivares et al., *Phys. Rev. A*, p. 050303 (87), (2013)

[10] [15] Stefano Olivares, *Physics Letters A*, p. 127720 (418), (2021)

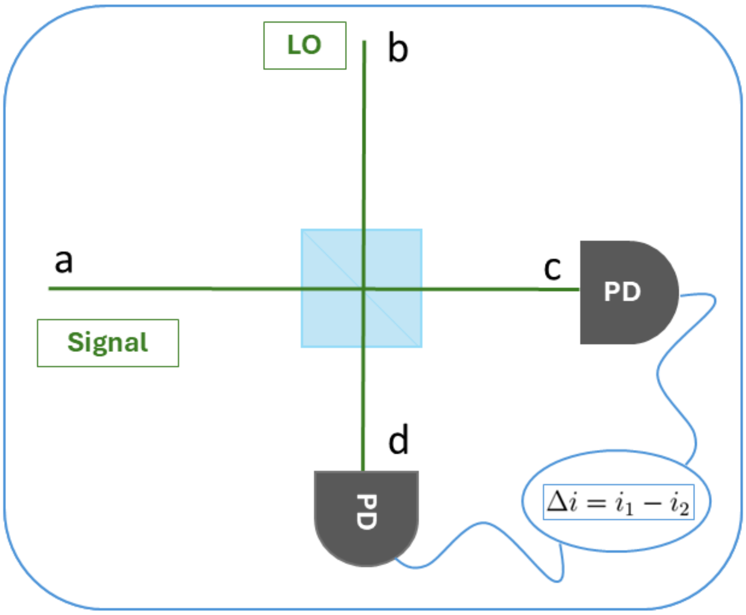

Figure 1.5: Sketch of a homodyne detector

to intensity, i.e. $\langle(\hat{N}_1 - \hat{N}_2)^2\rangle$, and this corresponds to $\beta^2\langle x_\theta^2\rangle$ only if $|\beta|^2 \gg \langle\hat{a}^\dagger\hat{a}\rangle$, that explains why the local oscillator must be more intense than the signal.

In the case of tomographic reconstruction, the signal difference is acquired at variance of the phase (experimentally by changing the optical path) of the LO. This gives access to the quadrature marginal probabilities that enable to reconstruct the optical state in the quadrature space.

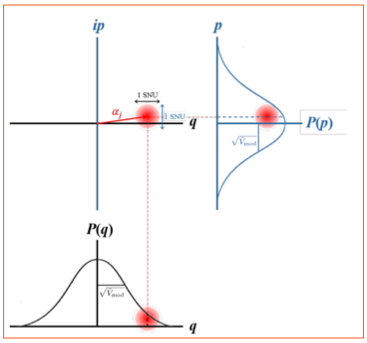

Figure 1.6: Representation of the marginal probability of fields quadratures.

1.2.2 Homodyne-like Detector

This detector is very similar to the one previously described, a schematic representation is reported in Figure 1.7[11] [12]. The main difference consists in the selected detectors, that are Photon-Number Resolving (a more detailed description of these devices is reported in the following section). The sensitivity of these devices also gives an upper limit to the intensity of the LO, that still must be greater than the signal[13] [14]. In the following Chapter, is reported our study of the suitable LO intensity so that the detector performs similarly

11: [16] Alessia Allevi et al., *International Journal of Quantum Information*, p. 1740016 (15), (2017)

12: **[DiMarioBecerra] DiMarioBecerra**

13: [17] Graciana Puentes et al., *Physical Review Letters*, p. 080404 (102), (2009)

14: [18] Gaia Donati et al., *Nature communications*, p. 5584 (5), (2014)

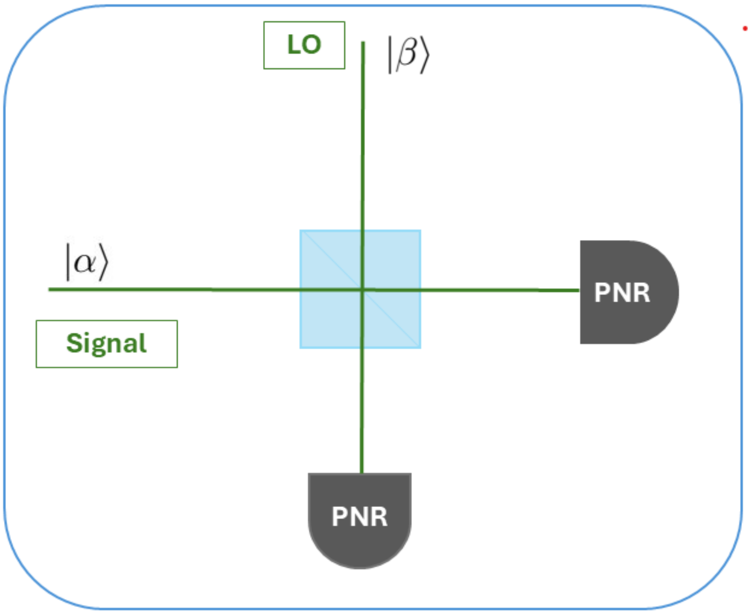

Figure 1.7: Sketch of a homodyne-like detector

to a homodyne one.
Another difference stands in the output of the detection scheme, that is no more the difference current of the detectors, but the current of each detector. Moreover each detector enables to reconstruct the output state statistics, that allows to investigate different properties of the state under exam.
With respect to the standard homodyne detector [15], information about the field quadratures is coded in the probability distribution of the difference of the two outputs. Let's consider two coherent input states, so also the BS outputs will be coherent, with corresponding mean values μ_c and μ_d. Let's define $\Delta = n_1 - n_2$ the difference of the number of photons measured at the two outputs. In this case, the probability distribution of Δ is the Skellam distribution[16]:

$$S_\Delta(\mu_c, \mu_d) = e^{-\mu_c} e^{-\mu_d} \left(\frac{\mu_c}{\mu_d}\right)^{\frac{\Delta}{2}} I_\Delta(2\sqrt{\mu_c \mu_d}), \qquad \Delta \in \mathbb{Z}$$

where $I_\Delta(x)$ is the first-type modified Bessel function. This detection scheme is the core of this work, the next chapter of this manuscript is fully dedicated to its experimental implementation and characterization, as well as ti the identification of the best processing solutions in the case of communication or discrimination protocols. The reader is addressed to that

[15] [19] Matteo Bina et al., *Optics Express*, pp. 10685–10692 (25), (2017)

[16] [20] John G Skellam, *Journal of the Royal Statistical Society Series A: Statistics in Society*, pp. 296–296 (109), (1946)

chapter to learn more about this receiver and the novel results achieved.

1.3 Detectors and acquisition chain

In this paragraph a general description of PNR detectors and a detailed one of the chosen devices and acquisition chain used in order to obtain suitable measurements is presented. As already mentioned above, the chosen PNR detectors for this project are Silicon Photomultipliers (SiPM).

1.3.1 Detecting Light

Detecting light means to convert photons in something measurable, typically electrical signals. In fact, photoelectric effect is the fundamental phenomenon that enables light measurement in the most common detectors. In such devices a photon of a suitable frequency can generate a free carrier by impinging on the metallic material. In principle, each photon is supposed to be destroyed and generate a free carrier, but in reality each detector is characterized by a certain probability η to detect a certain photon, depending on the wavelength, temperature and electronics. Commonly, η is called detection efficiency, and $0 < \eta < 1$. In quantum mechanics measurements require projector operators.[17] In the case of pure states, meaning states that can be described by the density operator

$$\hat{\rho} = |\psi\rangle\langle\psi|.$$

Measurements are performed by Projection Valued Measures (PVM). On the other hand, pure states are not so common to generate in laboratory, so one typically has to deal with mixed states, defined by the occupation probability of a set of states $|\psi_i\rangle$. In this case the density operator is described as

$$\hat{\rho} = \sum_i p_i |\psi_i\rangle\langle\psi_i|$$

These states require a different approach to measurement, represented by Positive-Operator Valued Measure (POVM),

[17] 17: [21] Matteo GA Paris, *The European Physical Journal Special Topics*, pp. 61–86 (203), (2012)

that is proportional to the square of the measurement operator

$$\hat{\Pi} = \hat{M}^{\dagger}\hat{M}$$

POVMs take into account the features of the detector used. In fact, let's consider a Geiger Mode (or On-Off) detector. These devices 'click' when they see light, but there is no proportionality between the input and the output signal. Considering η the detection probability, we write the POVM of such a detector in the case it does not click and in the case it does

$$\hat{\Pi}_{\text{off}} = \sum_{n=0}^{\infty}(1-\eta)^{n}|n\rangle\langle n|$$

$$\hat{\Pi}_{\text{on}} = \sum_{n=0}^{\infty}(1-(1-\eta)^{n})|n\rangle\langle n|$$

so that, if the detected light follows a photon number probability $P(n)$,

$$P_{\text{off}}(\eta) = \sum_{n=0}^{\infty}(1-\eta)^{n}P(n)$$

$$P_{on}(\eta) = \sum_{n=0}^{\infty}(1-(1-\eta)^{n})P(n)$$

A quite different approach is required in the case of PNR detectors, in which the output current is linearly proportional to the impinging light, therefore they allow to count the number of photons. Under the hypothesis to have a non-ideal detector, we want to calculate the probability to detect m photons when the device is lightened by n photons and the detection probability is η

$$\hat{\Pi}(m,n,\eta) = \sum_{n=m}^{\infty}\binom{n}{m}\eta^{n}(1-\eta)^{n-m}|n\rangle\langle n|$$

and so the detection probability becomes

$$P(m,n,\eta) = \sum_{n=m}^{\infty}\binom{n}{m}\eta^{n}(1-\eta)^{n-m}P(n)$$

that is a Bernoullian distribution, having mean value $\langle m\rangle = \eta\langle n\rangle$ and variance $\Delta m^{2} = \eta^{2}\langle n\rangle^{2} + \eta(1-\eta)\langle n\rangle$.

As widely explained in the following paragraph, even if the whole chosen detector is PNR, therefore characterized by the Bernoullian detection probability, the cells it is composed of work in Geiger mode, so it was worth mentioning both the descriptions.

1.3.2 Silicon Photomultipliers (SiPMs)

Silicon photomultipliers are electronic devices composed of cells. Each cell is nothing more than a Geiger-mode operated Single Photon Avalanche Photodiode (APD) kept over the breakdown threshold so that the output signal is no more proportional to the input one. This means that the energy of a single photon can generate an electron avalanche inside the cell. The reason why they are called cells rather than pixels is the fact that the device has no spatial resolution. In fact, as we were saying, each cell can generate an avalanche if a photon impinges on it. Therefore, according to the intensity of the light that illuminates the SiPM, a certain number of cells might "click" and generate an avalanche.

The cells are connected in parallel through a decoupling resistor, which is also used for quenching the generated avalanches. SiPMs are also called Multi-Pixel Photon Counter (MPPC) because all the APDs work simultaneously and the total output is proportional to the number of fired cells. In other words, the signals from the fired APDs are collected together at the same output simultaneously. Under the hypothesis of homogeneously lightened detector and that each cell is lit by one photon, the output is proportional to the field intensity; this is why SiPMs are considered to be Photon-Number-Resolving. More precisely the readout signal is the convolution of all the APDs' outputs [18] [19]. Among the several PNR detectors that are available on the market the reasons that brought the choice to SiPM are their high PNR capability (up to several tens of photons), their robustness and portability, the fact that they do not require cryogenic temperature to work and the fact that they can be considered low cost devices.

On the other hand, nothing is really perfect. Here are the main noise sources these detectors are susceptible to, but further there will be a discussion about the minimization of these sources [20].

With respect to the rest of the acquisition chain that is described in the following pages, the waveforms reported in this paragraph were collected using the DRS4 digitizer from Paul Scherrer Institute. The images are from a previous work,

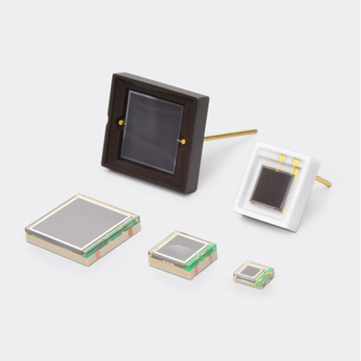

Figure 1.8: Picture of the model of SiPM used. Credits to Hamamatsu Photonics

[18] [22] Claudio Piemonte, *Nuclear Instruments and Methods in Physics Research Section A: Accelerators, Spectrometers, Detectors and Associated Equipment*, pp. 224–232 (568), (2006)

[19] [23] Ziraddin Sadygov, Azer Sadigov, and Sergey Khorev, *Physics of Particles and Nuclei Letters*, pp. 160–176 (17), (2020)

[20] [24] Marco Ramilli et al., *Journal of the Optical Society of America B*, pp. 852–862 (27), (2010)

since the digitizer has not been used to perform this experiment. The images are reported for a more clear explanation of the involved phenomena.

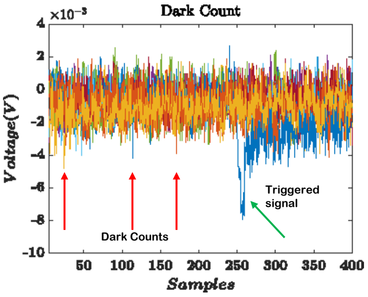

Figure 1.9: Dark count phenomenon on a set of waveform.

- **Dark counts (DC)**
  Thermal fluctuations might generate random avalanches even when there is no light impinging on the detector. As already mentioned, SiPMs are operated at room temperature, so the DC probability is higher with respect to cooled devices. It is important to keep in mind the randomness of this phenomenon, to better understand how it is overcome in our acquisition chain. In fact, DC is independent of a possible trigger, so its probability can be described as a Poissonian distribution:

  $$P_{DC} = \frac{\langle m_{DC} \rangle^m}{m!} e^{-\langle m_{DC} \rangle}$$

  where $\langle m_{DC} \rangle$ is the mean value of dark counts.

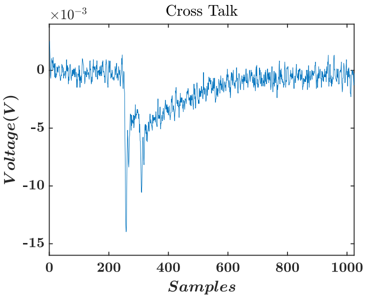

Figure 1.10: Cross-talk phenomenon on a waveform.

- **Cross-talk (CT)**
  This phenomenon describes the possibility that a generated avalanche triggers another avalanche in a nearby cell. In this case the second avalanche would represent a nonexistent detected photon. CT probability depends on the intensity of light on the sensor.
  To give a mathematical description of the phenomenon probability, let's call l the sum of cells triggered by light or DC, and k the total number of triggered cells, so that $k - l$ is the CT count [21]. If η is the probability of a cell to generate an avalanche, the CT probability can be written as

  $$C_{k,l}(\eta) = \binom{l}{k-l} \eta^{k-l} (1-\eta)^{2l-k}$$

  According to the timing, with respect to the light signal, CT can be simultaneous (prompt) or delayed. The first one is more rare but indistinguishable from the light signal, while the second can be easily observed on a waveform and mainly (not completely) excluded by choosing an appropriate integration gate.

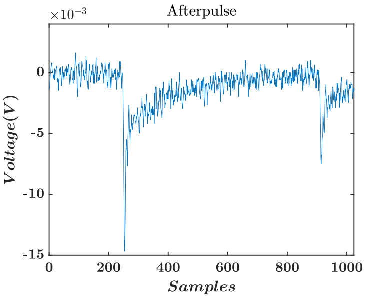

Figure 1.11: Afterpulse phenomenon on a waveform.

- **Afterpulse (AP)**
  This phenomenon is very similar to delayed CT but it is generated by ions trapped in the detector's layers. The main difference from CT is that AP has larger delay with respect to the light signal. According to the

[21] [25] Itai Afek et al., *Physical Review A—Atomic, Molecular, and Optical Physics*, p. 043830 (79), (2009)

same excluding strategy, AP results easier to avoid by choosing the correct integration gate. Therefore, in our case, it is considered to be negligible with respect to the other drawbacks.

- **Pile-up**

  It is a significant phenomenon in the case of a very intense field to be detected. We have already mentioned that each cell generates an output that corresponds to one photon, but what happens when the light it received corresponds to more than that? Of course, we would be reconstructing the light statistics by underestimating the incident light.

  The most diffused description of this phenomenon is given by the probability distribution of x free cells out of N total cells, when the detected output measures $\langle m \rangle = \eta \langle n \rangle$,

$$P(x) = \sum_{j=x}^{N} (-1)^{j-x} \binom{j}{x} \binom{N}{j} \frac{x}{j} (1 - \frac{j}{N})^{\eta n}$$

1.3.3 Acquisition chain

Considering all the above-mentioned characteristics of the detectors, the acquisition chain was optimized in order to reduce all the spurious effects.

First of all, it is worth mentioning that, to measure light statistics in time, it is important that the light source is pulsed, so to count the number of photons contained in each pulse. Therefore all the sources employed in this work were pulsed, and, what is more important, the acquisition chain was always triggered to the laser source.

The main reason why, apart from making the detection process faster, is the reduction of DC. In fact, DC is a random process; performing acquisitions triggered to the light source makes the probability to detect DC photons smaller. Let's give a description of the complete acquisition chain before going into details of how we reduced CT and pile-up effects.

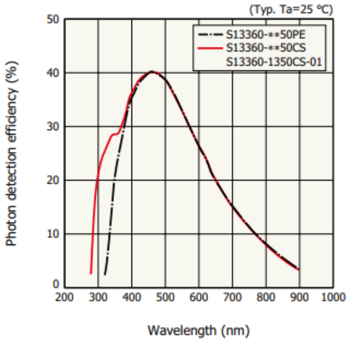

Figure 1.12: Quantum efficiency of the S1330-1350 SiPM detector, from Hamamatsu data sheet.

- **SiPM**

  The model chosen is MPPC S13360-1350CS from Hamamatsu Photonics. This company's devices are characterized by very low CT and DC with respect to other commercial items. The model in use has a surface of

1.3 mm x 1.3 mm, and each cell edge is 50 μm. In Figure 1.12 is reported the plot of the quantum efficiency as a function of the detected wavelength for this model, that has its peak in the green/blue region.

- **Power Supply and Amplification Unit (PSAU)**
  The detectors are connected to CAEN 5600 PSAU, that enables to power the devices and amplifies their signal at the same time. This model has two input and two output channels, each one with a dynamic range of $2V_{pp}$, therefore allows to use two SiPMs simultaneously. The embedded amplifier is a fast, inverting model with a settable range, going from 0 to 50 dB.
  All the measurements reported in this work were acquired by supplying the detector with 56 V and amplifying the acquired signal by 17 dB.

- **Analog integrator**
  In this specific case we used boxcar-gated integrators, more precisely the model SR250 from Stanford Research Systems. They consist of a circuit that, when closed, stores the electric charge in a capacitor. Once open, the capacitor discharges and enables saving the voltage value. The word 'gated' refers to the time gate in which the circuit is open to acquire, which can be set according to necessity. This is the acquisition chain stage that is triggered with the laser source. Boxcar-gated integrators add an extra gain to the acquired signal, that is still linear to the detected light. The maximum acquisition rate of the device is 10 kHz, that is the main limit to the laser source repetition rate.

The last device is the one that enables to keep delayed CT under control. In fact, by choosing an appropriate gate length (of the order of few nanoseconds) it is possible to exclude the avalanches generated by delayed CT without compromising the detected statistics. An integration gate between 10 ns and 15 ns has been demonstrated to be suitable for the aim[22]. As to prompt CT, there is not much that can be done but in our experience, for the chosen devices, its contribution is negligible. By adapting the acquisition chain, we succeeded in reaching DC values corresponding to $\sim 0.3\%$ and CT values lower than 1%. These parameters have been experimentally measured [23].
Eventually, pile-up is a critical phenomenon as well. The only

[22] 22: [26] Giovanni Chesi et al., , (), (2019)

[23] 23: [27] Alberto Sanvito et al., *Optics Express*, pp. 39846–39859 (32), (2024)

possible solution is to give attention to how light is spread on the sensor, so that it is as uniform as possible. In our case light is collected by multimode optical fibers that are directly connected to the SiPM mount, so that the output of the fiber is as close as possible to the SiPM. We have observed using a CCD camera that for a few μm distance there are no structures in the beam. Then, of course, it is important to control the intensity of light. The empirical experience with this acquisition chain led us to work with a mean value of less than 10 photons with the PSAU amplifier gain of 17 dB. In this condition, the reconstructed photon number histograms do not display any nonlinearity (that can be a consequence of the chain saturation as well) or underestimation. The acquired data are then divided by the overall gain and binned so that to every measurement corresponds an integer number. The re-binned histogram is known as pule height spectrum, an example in reported in Figure 1.13.

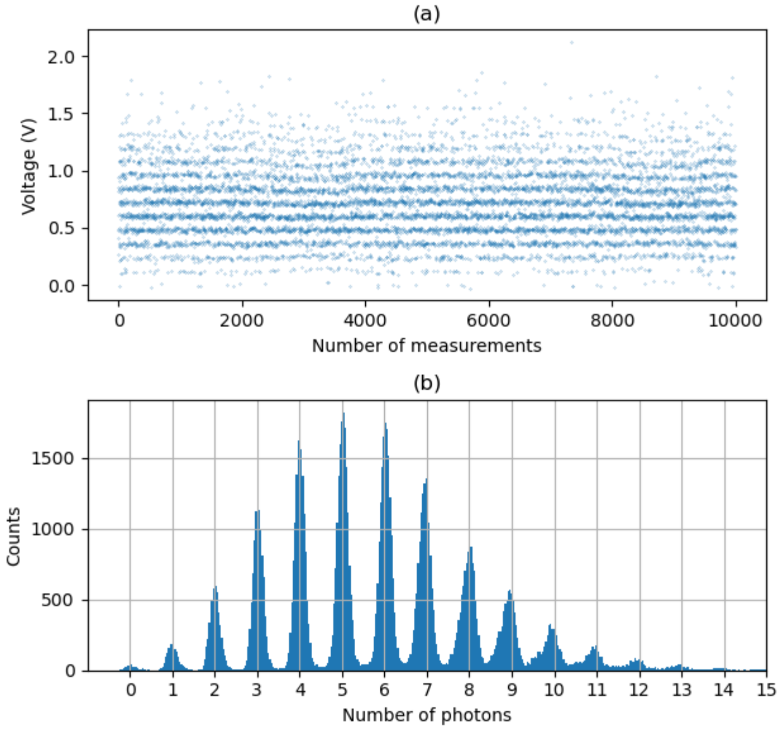

Figure 1.13: An acquired trace (top plot) and the corresponding pulse height spectrum (bottom plot).

1.4 Nonlinear Optics

[24] The last part of this chapter is dedicated to nonlinear optics. In the third chapter it is reported a characterization of SiPMs to reconstruct a manipulated beam at 1550 nm. As can be

24: [28] Robert W. Boyd, *Academic Press*, (), (2008)

observed in Figure 1.12, SiPMs are not sensitive to light in the infrared region. That's why we built an up-conversion system that preserves the nature of the state to be detected. Specifically, we generated a white-light continuum (WLC) and an optical parametric amplifier (OPA) to generate the infrared beam, while a sum-frequency generation (SFG) was performed to enable the detection. More details are reported in the dedicated chapter.
Similarly to the introduction to quantum optics, also all the demonstrations of the subject under exam are easy to find in the literature. Therefore we will give just the main results to help the reader better understand the relevant phenomena.

Nonlinear optics studies phenomena that manifest as a modification of the optical properties of a material due to the presence of light. So the main ingredients to observe such phenomena are an intense light field and a suitable material, typically birefringent. The material can be described through the macroscopic polarization

$$P = pN$$

where N is the number of atoms / molecules per unit volume composing the material and p is the dipole momentum of a single molecule. The macroscopic polarization can be seen as the sum of a linear and nonlinear contributions, and can be generally expanded as a Taylor series

$$P = P_L + P_{NL} = \epsilon_0 \chi E + \epsilon_0 \chi^{(2)} E^2 + 4\chi^{(3)} E^3 + \ldots$$

where $\chi^{(1)}$ is the linear susceptibility, $\chi^{(2)}$ and $\chi^{(3)}$ the second- and third-order nonlinear susceptibilities and E is the electric field of the input electromagnetic wave. As the order of the nonlinear phenomenon increases, it requires a higher light intensity to be observed. Nonlinear optical phenomena, such as SFG and OPA, respect energy and moment conservation.

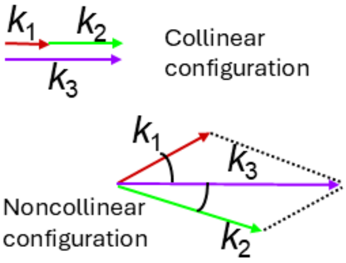

Figure 1.14: Phase matching representation.

Specifically they can be expressed under the definition of frequency matching

$$\omega_3 = \omega_1 + \omega_2$$

and phase matching

$$\vec{k_3} = \vec{k_1} + \vec{k_2}$$

where ω is the light frequency and $\vec{k}$ is the wavevector.

1.4.1 Sum Frequency generation (SFG) and Difference Frequency Generation (DFG)

This phenomenon describes the generation of a third field at the output of the nonlinear material, given two different inputs. In fact, if the input field is described as

$$E = a_1 e^{-i\omega_1 t} + a_2 e^{-i\omega_2 t} + c.c.$$

it is possible to substitute this expression in the second-order nonlinear polarization to obtain

$$P_{NL}^{(2)} = \epsilon_0 \chi^{(2)} E^2$$

$$\begin{aligned} P_{NL}^{(2)} = \epsilon_0 \chi^{(2)} \big[& a_1^2 e^{-2i\omega_1 t} + a_2^2 e^{-2i\omega_2 t} + 2a_1 a_2 e^{-i(\omega_1+\omega_2)t} + \\ & 2a_1 a_2 e^{-i(\omega_1-\omega_2)t} + c.c. \big] + 2\epsilon_0 \chi^{(2)} \left(|a_1|^2 + |a_2|^2 \right) \end{aligned}$$

where each term corresponds to a different nonlinear phenomenon. While the first two terms are, respectively, the second harmonics of the input fields, the third represents the generation of a field oscillating at a frequency that is the sum of the input frequencies

$$E = a_3 e^{-i\omega_3 t} + c.c.$$

with $\omega_3 = \omega_1 + \omega_2$. Analogously, the fourth term represents the difference-frequency generation, meaning the generation of a field oscillating at a frequency that is the difference of the input frequencies $\omega_3 = \omega_1 - \omega_2$. The last term represents the nonlinear phenomenon of optical rectification, that has not been exploited in this work.

From an operative point of view, these phenomena are not generated all together, but it is possible to choose the one to realize by changing the geometry of the interaction and the polarization of the light fields. The more decisive part is the tuning of the nonlinear material, meaning tuning the crystal lattice (e.g. by tilting the crystal or changing its temperature) so that the phase matching condition changes properly.

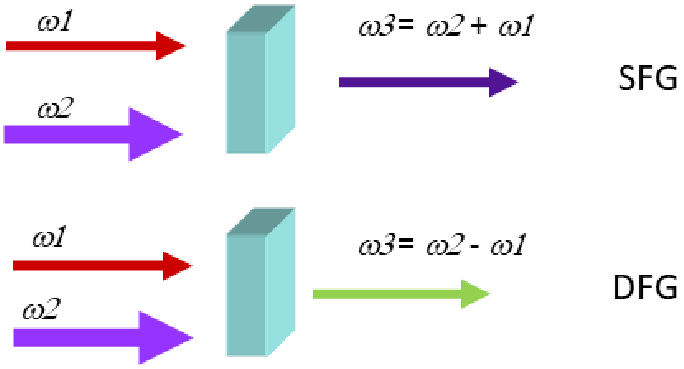

Figure 1.15: Sketch of SFG and DFG process.

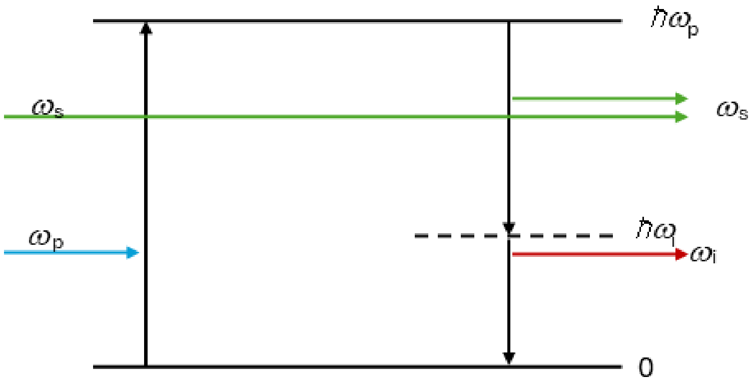

Figure 1.16: Sketch of an OPA.

1.4.2 Optical Parametric Amplifier (OPA)

If the input signal ω_1 is less intense than the input signal ω_2, where $\omega_1 < \omega_2$, it is possible to perform a proper nonlinear interaction to amplify the signal. In the standard description of this phenomenon, the more intense input is called pump and its frequency is ω_p while the less intense field is called signal, with frequency ω_s. The process they undergo can be imagined as a specific case of DFG. In fact, in this case the nonlinear process will make the pump beam weaker and amplify the signal. There will be also the generation of an idler signal, so that $\omega_i = \omega_p - \omega_s$. A schematic representation of the processes involved in an OPA is reported in Figure 4.4. The typical configuration for OPA is the collinear one, but as a consequence of the birefringence-induced walk-off, the superposition inside the material could be non-optimal. Therefore, a noncollinear configuration introduces a further degree of freedom that allows to obtain larger gain. The latter is the configuration that has been realized in the laboratory and that is reported in the fourth chapter of this thesis.

1.4.3 White Light Continuum (WLC)

Differently to the other described phenomena, White Light Continuum (WLC) is a third-order nonlinear ($\chi^{(3)}$) process[25]. It is a threshold process, meaning that the light field is required a minimum energy to generate such a phenomenon. Usually, ultrashort pulses are used to produce WLC, because they are very narrow in time domain (for example their duration is less than 200 fs) and, therefore, broad in the frequency domain (for example, converted in wavelength, ~ 20 nm). So all the pulse energy is concentrated in a short time. A typical WLC generation scheme requires to focus the optical beam. This will increase the fluence in the nonlinear material even more. In this condition, the phenomenon of self-phase modulation causes the enlargement of the beam spectrum. At the same time, the pulse undergoes the pulse-splitting phenomenon and the two splits (a reddish and a bluish one) propagate in the medium in opposite directions (in the pump reference frame). The velocity difference between the peak and the tail of the pulse, due to the different wavelengths, causes an optical shock that broadens the pulse spectrum. The overall output spectrum is typically asymmetric, as a consequence of self-steepening effect that the sub-pulses experience.

We have already mentioned that there is a minimum power required to generate such a phenomenon. In the case of Gaussian beams it is expressed as[26]

$$P_{cr} = \frac{3.77\lambda^2}{8\pi n_0 n_2}$$

being $n_0 = \sqrt{\chi^{(1)}}$ and n_2 the nonlinear refractive index coefficient, so that, given a certain intensity I, the refractive index is $n = n_0 + n_2 I$.

[25] A. Dubietis, A. Couairon, *Ultrafast Supercontinuum Generation in Transparent Solid-State Media*, Springer Briefs in Physics

[26] [29] John H Marburger, *Progress in quantum electronics*, pp. 35–110 (4), (1975)

Realization of a Hybrid Receiver

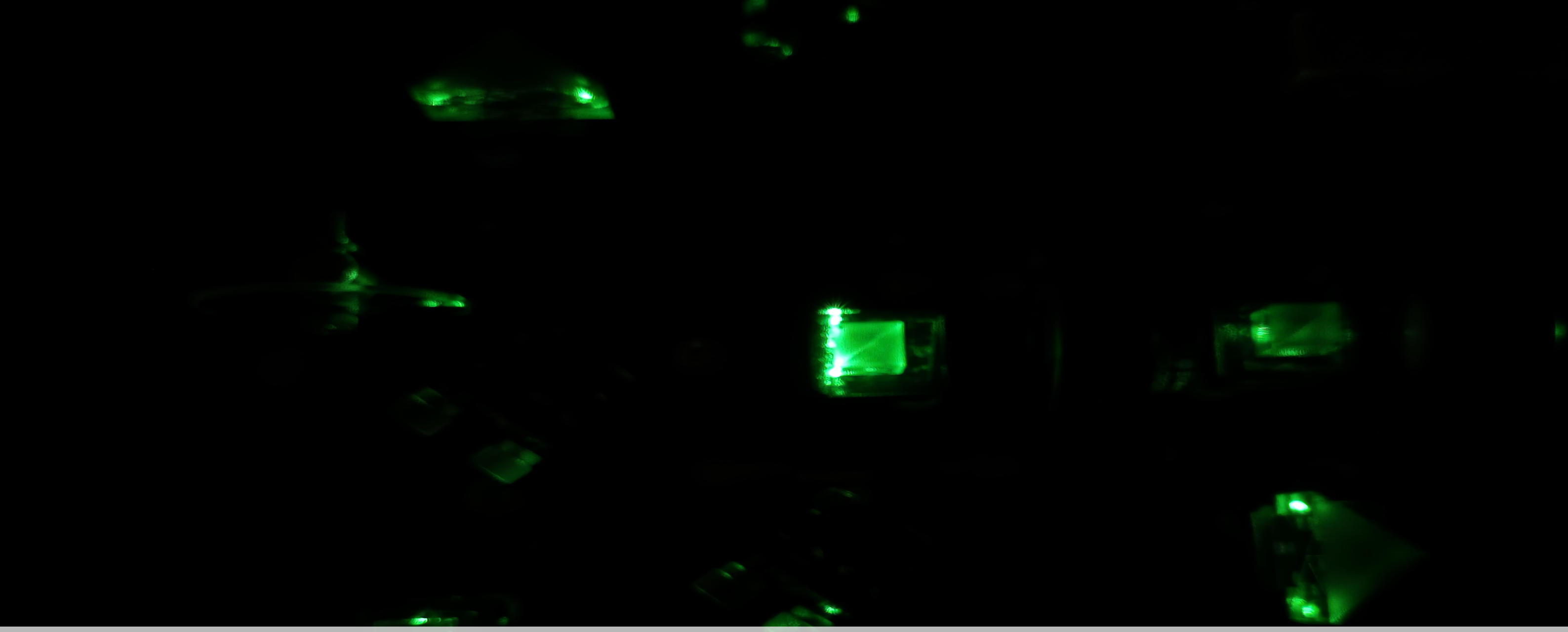

2 Realization of a Hybrid Receiver

In this chapter the first part of the original work is presented: the experimental realization of the Homodyne-Like detector described in the previous chapter and the optimization of the output analysis according to the desired application. The theoretical part has been developed in collaboration with Professor Stefano Olivares, from the University of Milan, and his PhD student Michele Notarnicola. Some of the results of this work are published in Optics Express [1] and Physics Letters A [2].

2.1 Theoretical development

In this part, we experimentally realize and demonstrate the suitability of our SiPM-based interferometric detector [3] in the context of quantum communication, based on the comparison of the theoretical and experimental behavior as well as on the comparison with a simulated standard homodyne detector having the same experimental parameters.

To perform a proof-of-principle demonstration, we choose a simple binary codification in phase, usually addressed as Binary Phase-Shift Keying (BPSK)[4] [5] [6] [7]. As suggested by the name, information is coded in the phase shift of a coherent state, in particular, after a first experimental evaluation (reported in this chapter), we consider a shift of π. Let's remark that such a phase coding means to have a bright

1: [27] Alberto Sanvito et al., *Optics Express*, pp. 39846–39859 (32), (2024)

2: [30] Silvia Cassina et al., *Physics Letters A*, p. 130403 (541), (2025)

3: [16] Alessia Allevi et al., *International Journal of Quantum Information*, p. 1740016 (15), (2017)

4: [31] János A Bergou, *Journal of Modern Optics*, pp. 160–180 (57), (2010)

5: [32] Carl W Helstrom, *Journal of Statistical Physics*, pp. 231–252 (1), (1969)

6: [33] Shuro Izumi et al., *Physical Review A—Atomic, Molecular, and Optical Physics*, p. 042328 (86), (2012)

7: [34] Christian R Müller and Christian Marquardt, *New Journal of Physics*, p. 032003 (17), (2015)

---

[0] Background photo: Mach-Zendher interferometer.

interference fringe on one output and a dark fringe on the other one. The phase change will just switch the two outputs. In this framework, we code the classical symbol $k = 0, 1$ in the state $|\alpha_k\rangle$ where

$$|\alpha_k\rangle = |\alpha e^{i\pi(k+1)}\rangle, \qquad\qquad k = (0,1)$$

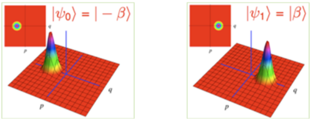

Figure 2.1: Representation of a binary phase shift.

so that $|\alpha_0\rangle = |\alpha e^{i\pi}\rangle = |-\alpha\rangle$ encodes the bit '0' and $|\alpha_1\rangle = |\alpha e^{2i\pi}\rangle = |\alpha\rangle$ encodes the bit '1'. Let's remark that the phase shift does not involve any energy change, so that for both the states the mean number of photons $|\alpha|^2$ is preserved. So, if Alice codes her bit into the state $|\alpha_k\rangle$, the state Bob will measure will be $|\sqrt{T}\alpha_k\rangle$, where T represents the channel transmissivity. The phase shift can be considered free of energy charge, but the transmission channel might be affected by losses.

As we have mentioned in the previous chapter, the detection scheme involves the interaction of the state sent by Alice with another, more intense, coherent state. We define $|z|^2$ the mean value of the local oscillator. In quantum optics, it is well-known that if the BS inputs are coherent states, the outputs will be coherent states as well [8]. So the output that will be measured by the detectors will be characterized by a Poissonian distribution

$$P_n(\mu|\alpha_k) = \frac{\mu^n}{n!}e^{-\mu}$$

however, in this case, we need to distinguish between the transmitted and reflected outputs according to the signal input:

$$\mu_k^{(t)} = \frac{1}{2}\left(\sqrt{T}\alpha^2 + z^2 + 2\xi\sqrt{T}\alpha_k z\right)$$
$$\mu_k^{(r)} = \frac{1}{2}\left(\sqrt{T}\alpha^2 + z^2 - 2\xi\sqrt{T}\alpha_k z\right)$$

In this definition we have introduced the visibility term $\xi < 1$, that depends on the experimental overlap at the BS. All the premises introduced so far give the context to the following characterization. In fact, according to how we choose to deal with the output of the detector, the detection probability will be different. As we have widely discussed in the previous chapter, the strategy used to calculate the probability will affect the entropy, and so the information that can be shared. In this work we consider three possible solutions for the acquired signal manipulation, that will lead to different

[8] [15] Stefano Olivares, *Physics Letters A*, p. 127720 (418), (2021)

results. Mutual information is the figure of merit selected in this work to characterize the behavior of the detector.

2.1.1 Weak Field (WF) strategy

In this hybrid detection scheme the output current of each SiPM is acquired separately. Therefore, we have access to the probability distribution on the two BS arms, this means that on the transmitted arm there will be n photons, and the one on the reflected one there will be m photons, both characterized by a Poissonian probability distribution. Since the outputs are considered independently from each other, given a state $|\alpha_k\rangle$, the conditional probability is given by a bivariate Poissonian distribution,

$$P_{WF}(n,m|\alpha_k) = P_n(\mu_k^{(t)}|\alpha_k)P_m(\mu_k^{(r)}|\alpha_k)$$

Shannon's entropy

$$H = -\sum p \log_2 p$$

Mutual information

$$I(X:Y) = H(X) - H(X,Y)$$

According to the definition given in the previous chapter, we can calculate the corresponding conditional entropy just by substituting this probability distribution. We are interested in the final definition of the mutual information that in this scenario becomes

$$\begin{aligned} I_{WF}(A;B) &= H\Big[\sum_{k=0,1} q_k p_{WF}(n,m|\alpha_k)\Big] - \sum_{k=0,1} q_k H[p_{WF}(n,m|\alpha_k)] \\ &= \sum_{n,m=0}^{\infty}\Big[\sum_{k=0,1} q_k p_{WF}(n,m|\alpha_k)\log_2\big(q_k p_{WF}(n,m|\alpha_k)\big)\Big] \\ &\quad + \sum_{k=0,1} q_k\Big[\sum_{n,m=0}^{\infty} p_{WF}(n,m|\alpha_k)\log_2 p_{WF}(n,m|\alpha_k)\Big] \end{aligned} \tag{2.1}$$

where we have defined q_k the *a priori* probability of the symbol $k = 0,1$.

2.1.2 Homodyne-Like (HL) strategy

In this scenario we make the detector work exactly like a standard homodyne one, so that the only difference will be the discrete nature of the detectors' output. Like in the standard case, information is coded in the difference of the two output currents, that in this case will correspond to the difference of the photons detected by the two detectors, Δ.

We have already introduced the Skellam distribution, which represents the photon-number difference distribution.

$$p_{HL}(\Delta|\alpha_k) = \sum_{m=0}^{\infty} P_{m-\Delta}(\mu_k^{(t)}|\alpha_k) P_m(\mu_k^{(r)}|\alpha_k) = S_\Delta(\mu_k^{(t)}, \mu_k^{(r)})$$

Similarly to the previous case, from this probability we can calculate the related conditional entropy, to finally obtain the mutual information. In the case of HL strategy it reads:

$$\begin{aligned} I_{HL}(A;B) &= H\Big[\sum_{k=0,1} q_k p_{HL}(\Delta|\alpha_k)\Big] - \sum_{k=0,1} q_k H[p_{HL}(\Delta|\alpha_k)] \\ &= -\sum_{\Delta=-\infty}^{\infty} \Big[\sum_{k=0,1} q_k p_{HL}(\Delta|\alpha_k) \log_2 \big(q_k p_{HL}(\Delta|\alpha_k)\big)\Big] \\ &\quad + \sum_{k=0,1} q_k \Big[\sum_{\Delta=-\infty}^{\infty} p_{HL}(\Delta|\alpha_k) \log_2 p_{HL}(\Delta|\alpha_k)\Big] \end{aligned} \tag{2.2}$$

where, again, q_k represents the *a priori* probability of the symbol $k = 0, 1$.

2.1.3 Binary State Discrimination (BDS) strategy

Let's suppose that the state we call $|\alpha_0\rangle$ is the one with the dark fringe on the transmitted output and state $|\alpha_1\rangle$ has the dark fringe on the reflected output. In general, we can say that the detector on the transmitted arm will measure n photons, and the one on the reflected one will measure m photons. If we define the difference $\Delta = n - m$, we can distinguish the detected state according to its sign. In fact, if $\Delta > 0$ the bright fringe will be on the transmitted arm, meaning we are measuring the state $|\alpha_0\rangle$, otherwise, for $\Delta < 0$ we will be measuring the state $|\alpha_1\rangle$. In the rare case in which $\Delta = 0$ the state will be randomly assigned. In this context, we can define the conditional probabilities

$$p_{BDS}(0|\alpha_k) = \sum_{\Delta>0} p_{HL}(\Delta|\alpha_k) - \frac{p_{HL}(\Delta = 0|\alpha_k)}{2}$$

$$p_{BDS}(1|\alpha_k) = 1 - p_{BDS}(0|\alpha_k)$$

Exactly as explained for the previous cases, defining q_k the *a priori* probability of the symbol $k = 0, 1$, it is possible to calculate the mutual information in this scenario,

$$\begin{aligned}I_{BDS}(A;B) &= H\big[\sum_{k=0,1} q_k p_{BDS}(j|\alpha_k)\big] - \sum_{k=0,1} q_k H[p_{BDS}(j|\alpha_k)] \\ &= -\sum_{j=0,1}\big[\sum_{k=0,1} q_k p_{BDS}(j|\alpha_k)\log_2\big(q_k p_{BDS}(j|\alpha_k)\big)\big] \\ &\quad + \sum_{k=0,1} q_k \big[\sum_{j=0,1} p_{BDS}(j|\alpha_k)\log_2 p_{BDS}(j|\alpha_k)\big]\end{aligned} \tag{2.3}$$

Due to the non-orthogonality of the coherent states, the discrimination between the coded states is nontrivial, meaning that there is a non-null probability to infer the wrong symbol.

The reader will note that the three strategies require a different manipulation of the acquired data. According to the data processing inequality, the more the data are processed, the more information is lost[9]. So we can expect that WF strategy will give more information than HL strategy, which will give more information than BDS strategy[10]:

$$I_{WF}(A;B) \geq I_{HL}(A;B) \geq I_{BDS}(A;B)$$

Truth be told, in the scenario of BPSK, in absence of energy variation, WF and HL strategies lead to the same result in terms of mutual information. An intuitive explanation of this result is the fact that, by performing WF detection, we obtain the outcome (n, m). This corresponds to measure both the difference $\Delta = n - m$ and the sum $\sigma = n + m$ currents. The joint probability $P(\sigma, \Delta|\alpha_k)$ contains the same amount of information on the encoded signal as $p_{WF}(n, m|\alpha_k)$. We can rewrite $P(\sigma, \Delta|\alpha_k) = P_{HL}(\Delta|\alpha_k) f(\sigma, \Delta)$ where $f(\sigma, \Delta)$ is a suitable function independent of α_k so that $\sum_\sigma f(\sigma, \Delta) = 1$. Accordingly, information on the signal phase is only carried by the difference photocurrent, and, after straightforward calculation, we get $I_{WF}(A;B) = I_{HL}(A;B)$.

2.1.4 Application to communication

The final part of this work involves the characterization of this detector under the assumption of a pure-lossy channel. In this context, we include the presence of an eavesdropper who has full access to the channel losses, but has no ability to manipulate the coded states [11].

9: [8] Thomas M. Cover and Joy A. Thomas, *John Wiley & Sons Inc.,* (), (2005)

10: [35] Michele N Notarnicola and Stefano Olivares, *arXiv preprint arXiv:2405.14310,* (), (2024)

11: [36] Ziwen Pan et al., *Physical Review Applied*, p. 024044 (14), (2020) We assume that Eve has the same hybrid detector, but with perfect overlap, $\xi_E = 1$. We will first simulate the case of individual attacks, where information obtained by Eve is the mutual information calculated according to the selected strategy. In the case of direct reconciliation the mutual information is calculated between Eve and Alice, while in the case of reverse reconciliation it is calculated with respect to Bob's information.

Key Generation Rate

$$\Delta I = I(A;B) - I(E;A/B)$$

Secondly, we will consider the collective attack scenario, only in reverse reconciliation since it is the one that best preserves the security of the communication. In this context, the mutual information between Bob and Eve is given by the Holevo information and should be properly calculated for each strategy.

Given T, the channel transmittance, the signal that Bob will measure is $T|\alpha\rangle$, while the one Eve has access to is $(1-T)|\alpha\rangle$. In general, the Holevo information for this scenario reads[12] [13]

Von-Neumann Entropy

$$S[\rho] = -\mathrm{Tr}[\rho \log_2 \rho]$$

$$\chi(B:E) = S(\rho_E) - S(\rho_{E|B})$$

where

$$\rho_E = \sum_k q_k |\sqrt{(1-T)}\alpha_k\rangle\langle\sqrt{(1-T)}\alpha_k|$$

We can calculate the conditional entropy for each signal processing strategy. In the case of WF, we define

$$p^B_{WF}(n_B, m_B) = \sum_k q_k p^B_{WF}(n_B, m_B|\alpha_k)$$

and so

$$S_{WF}(E|B) = \sum_{n_B, m_B} p^B_{WF}(n_B, m_B) S[\rho_{E|(n_B, m_B)}]$$

where

$$S[\rho_{E|(n_B,m_B)}] = \frac{1}{2p^B_{WF}(n_B, m_B)} \sum_{k=0,1} p^B_{WF}(n_B, m_B|\alpha_k)|\sqrt{(1-T)}\alpha_k\rangle\langle\sqrt{(1-T)}\alpha_k|$$

The equivalence of WF and HL strategies holds also for the calculation of KGR under collective attack condition. In fact, $\rho_{E|(n_B,m_B)} = \rho_{E|\Delta}$ where $\Delta = n_B - m_B$, and so

$$S_{WF}(E|B) = S_{HL}(E|B)$$

[12] [6] Marco Cattaneo, Matteo G. A. Paris, and Stefano Olivares, *Phys. Rev. A*, p. 012333 (98), (2018)

[13] [37] Michele N Notarnicola et al., *New Journal of Physics*, p. 103014 (25), (2023)

Finally, we consider the case of BDS strategy. Similarly to the WF case, we define

$$p^B_{BDS}(j) = \sum_k q_k p^B_{BDS}(j|\alpha_k)$$

so that

$$S_{BDS}(E|B) = \sum_{j=0,1} p^B_{BDS}(j) S[\rho_{E|j}]$$

with

$$S[\rho_{E|j}] = \frac{1}{2p^B_{BDS}(j)} \sum_{k=0,1} p^B_{BDS}(j|\alpha_k) |\sqrt{(1-T)}\alpha_k\rangle\langle\sqrt{(1-T)}\alpha_k|$$

2.2 Experimental Setup and Data Acquisition

In this section we give a schematic description of the experimental setup realized in the laboratory.
The setup is developed in bulk optics until the detection phase, where the light is collected by optical fibers, a schematic representation is reported in Figure 2.2. The light source is the built-in second harmonic of a Yb:KGW pulsed laser. The pulse duration is about 190 fs, and the output wavelength is 515 nm. The source is operated at a repetition rate of 5 kHz. Since the first part of this work is the proof-of-principle characterization of the detector, we chose to use a wavelength to which the detector is very sensitive.
The setup is basically a Mach-Zehnder interferometer: the laser light is split at a first balanced BS, so that one arm will be manipulated as the signal and the other one will be the

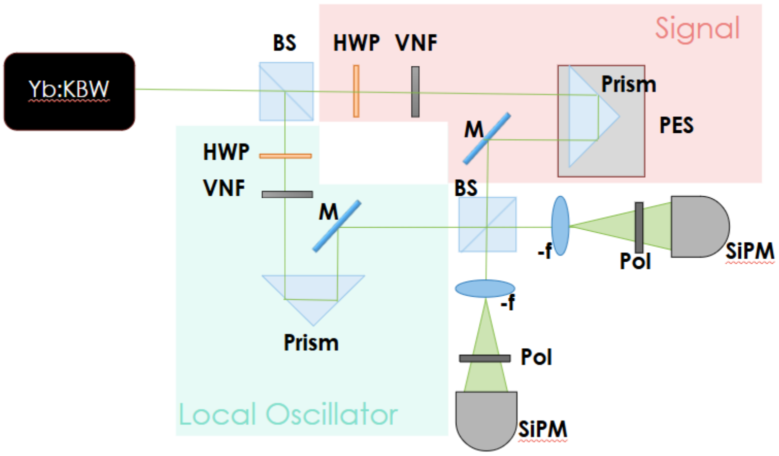

Figure 2.2: Sketch of the experimental setup.

LO. Then, the two light beams are recombined at the second BS, where they interfere. A piezo-electric movement allows to slightly change one arm's length so that it is possible to perform measurements at variance of the phase as well as set the condition for $|\alpha\rangle$ or $|-\alpha\rangle$. The model mounted in the setup performs a 17.4 μm shift with a difference potential of 150 V. On both arms a half-wave plate and a neutral density variable filter are placed. These allow to balance the signal and LO outputs and change the intensity of the beams, in order to find the optimal mean value for the LO or to simulate losses along the channel by attenuating the signal.
At the second balanced BS outputs two pinholes are placed to exclude the side fringes before light is collected by two multimode fibers (1 mm core) and detected by SiPMs.
Since the acquisition chain is the same for all the experimental works reported in this manuscript, it has been widely described in the introductory chapter. Therefore the reader is referred to Section 1.3.3.
During the acquisitions the operating voltage of the SiPMs was 56 V, the amplifier gain was set, in this case, at 24 dB and the boxcar integration gate was set at 15 ns.
For each mean value reported in the following section, a series of 10^5 pulses was acquired.

2.3 Experimental Results

2.3.1 Phase characterization

The first characterization performed was related to the phase control. Fixed a certain mean value for the signal and the LO, the piezo-electric stage was controlled by an external voltage supplier with a sensitivity of 0.1 V, so that we could acquire measurements by changing the voltage difference by steps of 0.5 V. Such a voltage difference corresponds to a movement of about 6 nm. To ensure a visibility as good as possible, in this characterization the signal and the local oscillator have similar mean values, i.e. 16.5 mean photons each. First of all, we observe the statistical distributions of the two outputs, that are supposed to be Poissonian. In Figure 2.3 are reported the two outputs of the detectors in an optimal condition, so that the first channel collects a bright fringe (in fact, the mean value is $\langle m \rangle = 12.28$ photons) and the second channel acquires a dark one ($\langle m \rangle = 1.55$ photons).

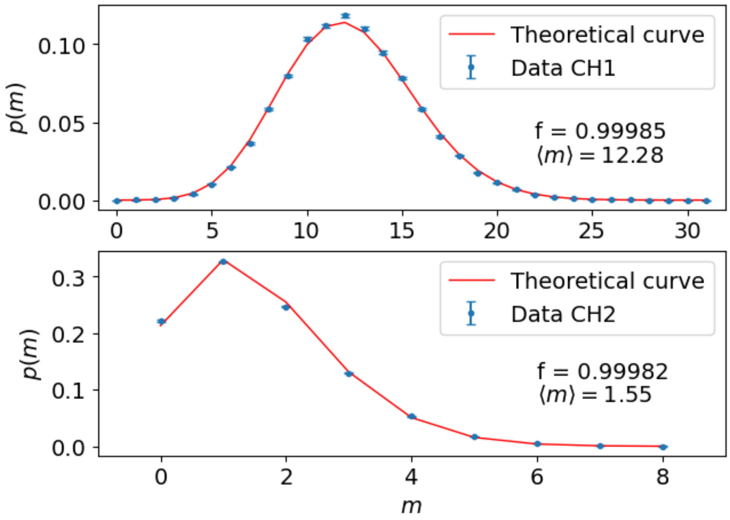

Figure 2.3: Outputs probability distribution.

In the two plots we present the experimental probability distributions of the number of collected photons, shown as blue dots, and the theoretically expected distribution, represented by the solid red line. The latter is a Poissonian distribution having the same mean value as the experimental one. To quantify the agreement of the data to the theory, we use the fidelity, defined as:

$$f = \sum_n \sqrt{P_{exp}(n) P_{th}(n)}$$

where $P_{exp}(n)$ and $P_{th}(n)$ are the probability distribution of the experimental and theoretical distribution, respectively. The closer this value is to 1, the better the two curves agree. To the best of our experience a good agreement is given by $f > 0.999$, that corresponds to the chosen benchmark in this thesis. As we can see in Figure 2.3, both the curves respect this criterion, so we can state that the output state is coherent, as expected.

The same measurement can be performed by slightly changing the optical path of one of the two arms of the interferometer. The modification of the optical path induces a shift in the fringes, which is measured as a variation in intensity. In Figure 2.4 are reported the mean values as the piezo-electric stage moves from an initial position by steps of 6 nm. The plot reports both the detectors' outputs: the first channel is represented in blue dots while the second channel is represented in red dots. According to theory the behavior is similar to a cosine squared function.

Some deviations from expectation, that can be observed for certain values, are due to mechanical vibrations external to the laboratory that could not be avoided, as well as the non linear response of the piezo to the input voltage variation. Nevertheless, the overall behavior allows us to perform the detector characterization.

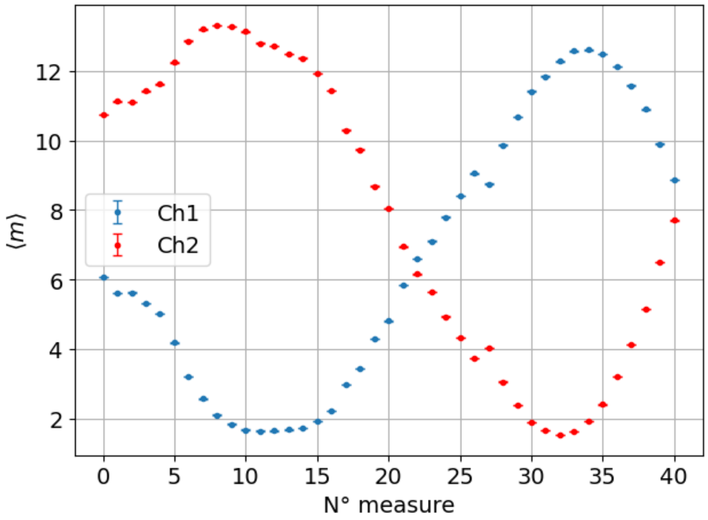

Figure 2.4: Mean values of the measurements acquired by shifting the phase.

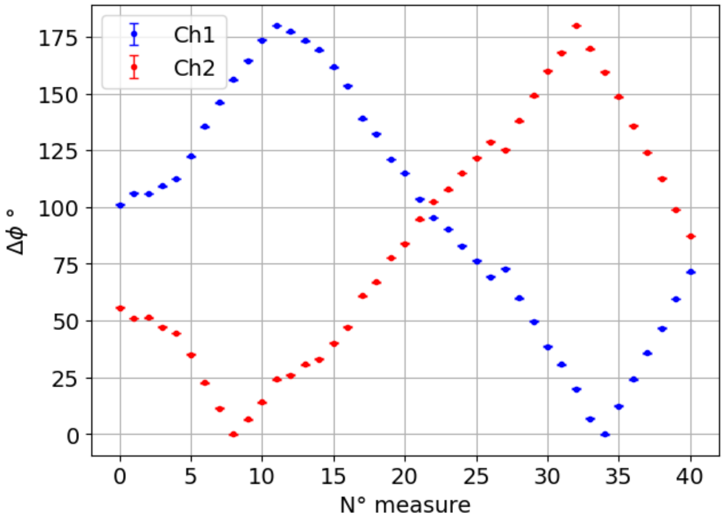

Figure 2.5: Retrieved phase for each measurement.

In fact, we can translate the intensity acquisition into a phase description as reported in Figure 2.5. Here we notice that a phase shift of $k\pi$, where k is an integer number, corresponds to the condition in which one detector is placed on the dark part of a fringe and the other on the brightest part.

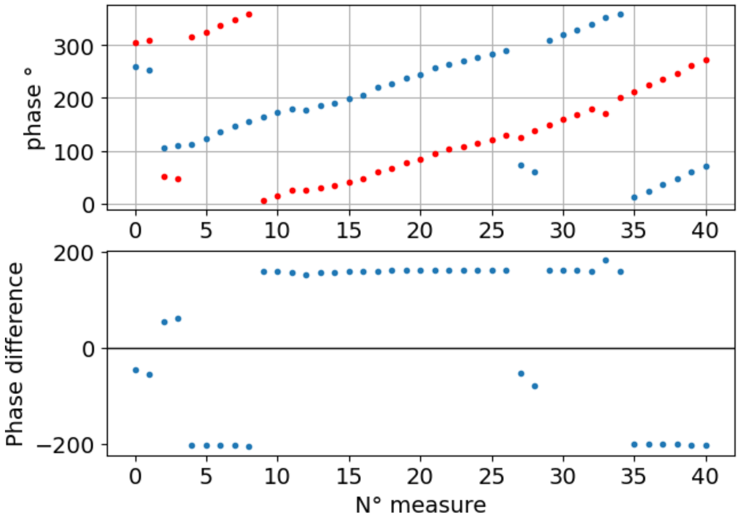

Figure 2.6: Measured relative phase from the initial position and difference of phase between the two BS outputs.

In the upper plot of Figure 2.6 are reported the phase-shift values (considered from the initial position) on the interferometric arms, estimated from the initial condition, for each acquisition represented in Figure 2.4. Again, blue dots correspond to the first channel, while red dots correspond to the second channel.
A typical phase difference of π between the two outputs is expected because of the BS behavior, as shown in the lower plot of Figure 2.6, where the phase difference of the two arms is represented for every acquisition.

2.3.2 Skellam distribution

At this point, it is worth investigating the photon-number difference distribution, expected to correspond to the Skellam distribution. In Figure 2.7 an example of experimental photon-number difference distribution is plotted. This corresponds to the case in which the first channel collected a bright fringe and the second channel a dark one. Blue dots represent the photon-number difference of the measured data, while the red curve represents the theoretical distribution. Also in this case, the fidelity criterion suggests that data and theory are in agreement.

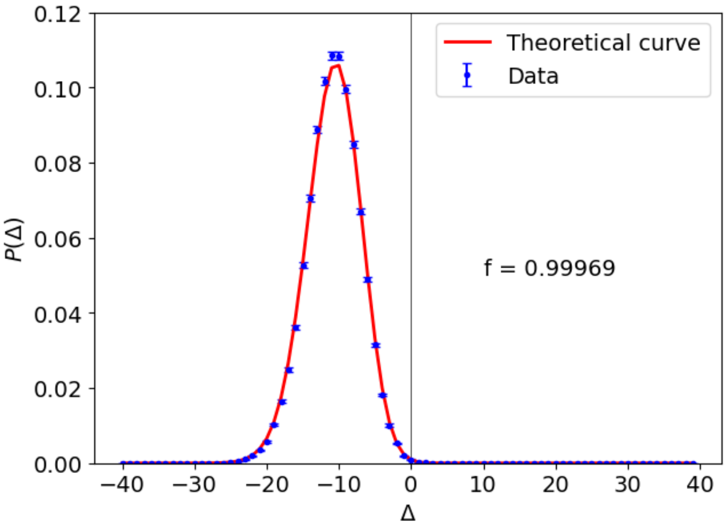

Figure 2.7: Photon-number difference distribution.

It is interesting to perform a further investigation on this matter, observing how the Skellam distribution changes as a function of the phase shift. This information plays a fundamental role in the case of the exploitation of HL strategy, since the discrimination of the state depends on this distribution. A possible overlap of the curve representing the state $|\alpha\rangle$ and the one representing $|-\alpha\rangle$ implies a certain error probability in the discrimination of the state. The larger the overlap, the greater the error probability. If we consider a phase shift of π, there will be a switch of the intensity of the two outputs, so that the Skellam distribution centered in a certain value $+\delta$ will shift to a symmetrical distribution having mean value $-\delta$, similarly to what is shown in Figure 2.8.

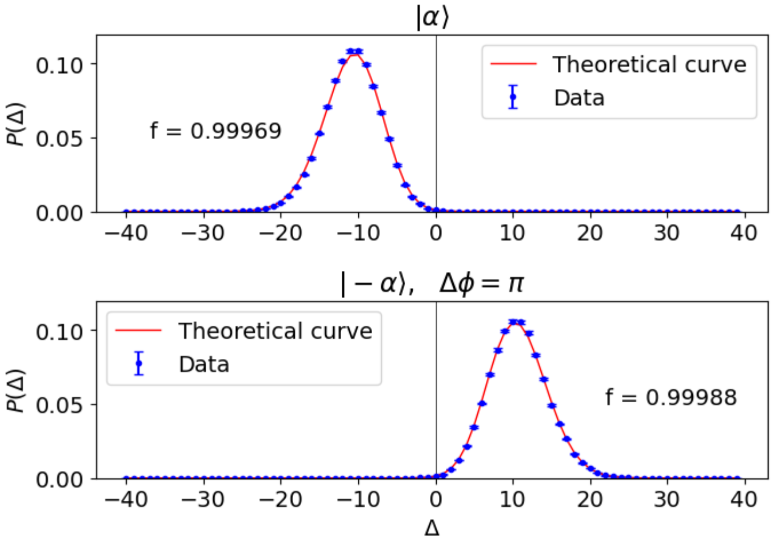

Figure 2.8: Skellam distribution for states $|\alpha\rangle$ and $|-\alpha\rangle$, when the external phase shift is π.

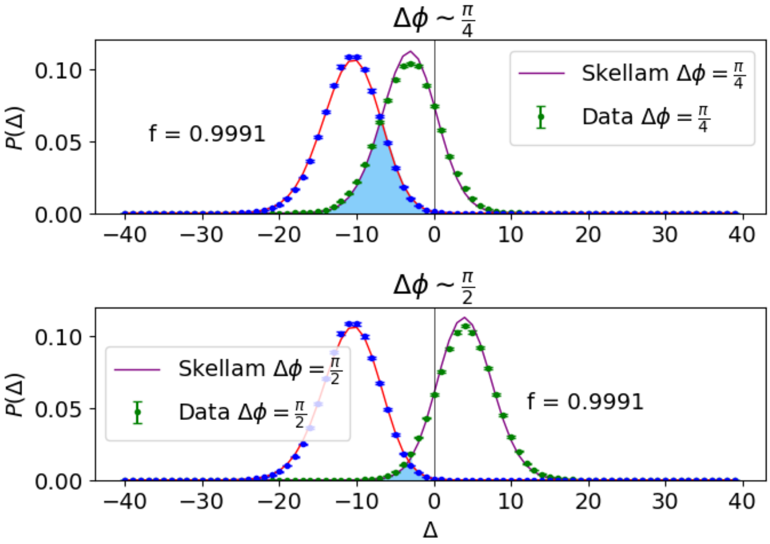

Figure 2.9: Skellam distribution for states $|\alpha\rangle$, $|\alpha\rangle$ shifted by $\frac{\pi}{4}$ and $|\alpha\rangle$ shifted by $\frac{\pi}{2}$.

Let's consider the same initial state, but with a phase shift different from π. For this specific initial state, increasing the relative phase starting from zero means moving the Skellam distribution from the negative part of the x axis to positive values.

This can be observed in Figure 2.9, where the same initial state $|\alpha\rangle$ as in Figure 2.8 is reported together with the state shifted by $\Delta\phi = \frac{\pi}{4}$ (first panel), and by $\Delta\phi = \frac{\pi}{2}$ (second panel). Once again, the solid curves (red and purple) represent the theoretically expected curves, while the dots (blue and green) represent the experimentally measured photon-number difference probabilities. The high values of fidelity prove the goodness of the theoretical model. The colored area under the shifted curves represents the probability to measure the wrong state, namely the error probability. To reduce the error probability, the BPSK was implemented by shifting the initial state by $\Delta\phi = \pi$.

2.3.3 Signal and Local Oscillator

Since the use of SiPMs imposes an upper limit to the intensity of the LO [14], in this section we study the behavior of the receiver at variance of the intensities involved in terms of mutual information $I(A; B)$. In this first part, we focus on the strategy that is more similar to the standard homodyne, namely the HL strategy.

In particular, given a certain signal intensity, we want to characterize the intensity required to the LO to obtain high

[14] [38] Stefano Olivares, Alessia Allevi, and Maria Bondani, *Physics Letters A*, p. 126354 (384), (2020)

values of mutual information. Therefore, we set the mean value of the signal equal to $\langle m_{sig} \rangle = 1.97$ photons and changed the intensity of the LO using a variable neutral density filter. The selected intensity covers a range between $\langle m_{LO} \rangle = 1.09$ and $\langle m_{LO} \rangle = 14.57$ photons. In Figure 2.10 are reported the mutual information obtained values. On the x axis is reported the ratio between the LO and the signal mean values. This choice allows us to have a general idea of the required proportion between the two fields.

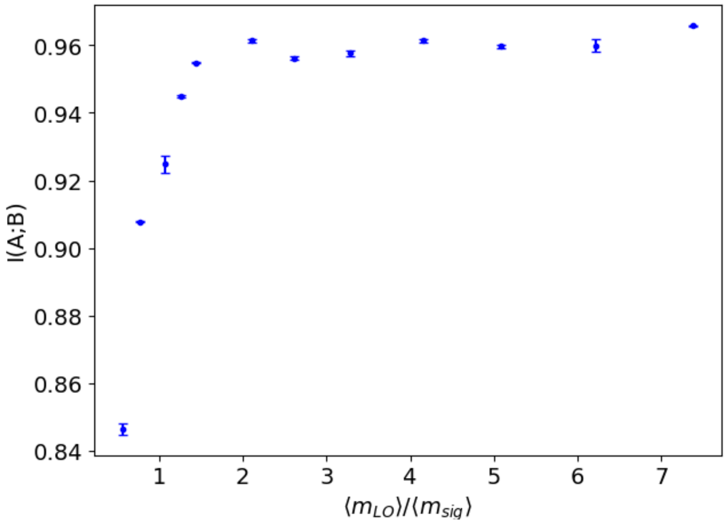

Figure 2.10: Mutual information as a function of the ratio of the LO and signal intensity. $\langle m_{sig} \rangle = 1.97$

As it can be observed from the image, the mutual information increases as the LO intensity increases until it shows an asymptotic behavior, where the limit for binary encoding is 1. In the first part of the plot, for x values lower than 3.5, we can observe some fluctuations probably due to the mechanical oscillations in the lab. From this study we deduce that a LO intensity that is at least four times the intensity of the signal is suitable to saturate the value of mutual information.

As mentioned at the beginning of the chapter, the beam propagation is in free space and there are some mechanical vibrations in the lab that cannot be controlled. This causes a modification of the overlap across the measurements. We describe the overlap as a function of the visibility, both the expected and the measured one. The theoretical visibility is defined starting from the mean values of the signal and the LO, and it reads as:

$$V_{th} = 2\sqrt{\frac{\langle m_{sig} \rangle \langle m_{LO} \rangle}{\langle m_{sig} \rangle + \langle m_{LO} \rangle}}$$

while the experimental visibility is obtained from the measurements of the light and dark fringes (at variance of the relative phase of the interferometer)[15]

$$V_{exp} = \frac{\langle m_{max} \rangle - \langle m_{min} \rangle}{\langle m_{max} \rangle + \langle m_{min} \rangle}$$

The overlap takes into account the discrepancies between the two visibilities [16]. In fact we can define $\bar{V} = \frac{V_{exp}}{V_{th}}$, so that the overlap reads as

$$\xi = \frac{\bar{V}}{2 - \bar{V}}$$

Taking this into account and trying to estimate the overlap during the measurements, we fix a signal intensity ($\langle m_{sig} \rangle = 3.07$), and measure the mutual information at variance of the LO intensity. In this case we compare the three different strategies to observe if the ratio value is preserved. The results are reported in Figure 2.11.

First of all we observe that the overlap range, which extends from 0.86 to 0.91, is the same for all the strategies. This is expected since its calculation requires the direct output of the detector, with the essential post processing to obtain the photon number (like the WF strategy). The two light-colored bands represent the expected range of mutual information taking into account the estimated overlap. The blue band represents BDS, while the green one represents WF. A further red band, representing HL, should have been plotted, but since it is exactly the same as the green one, their overlap would have made it harder to read the plot.

From Figure 2.11 we can first observe that the three strategies have a similar asymptotic behavior, consistent with the one presented in Figure 2.10. A suitable value of mutual information is reached for $\langle m_{LO} \rangle \sim 12$, meaning that the ratio $\frac{\langle m_{LO} \rangle}{\langle m_{sig} \rangle} \sim 4$, again consistent with the previous results.

Moreover, we observe that the data related to WF and HL strategies not only have the same behavior, but have very close values of mutual information, as predicted from theory. On the other hand, we can experimentally observe that, all else being equal, the larger data manipulation required to perform BDS strategy leads to lower values of mutual information. Also this result was theoretically expected.

[15] [39] Matthew T DiMario and Francisco E Becerra, *Physical review letters*, p. 023603 (121), (2018)

[16] [40] Michele N Notarnicola, Matteo GA Paris, and Stefano Olivares, *Journal of the Optical Society of America B*, pp. 705–714 (40), (2023)

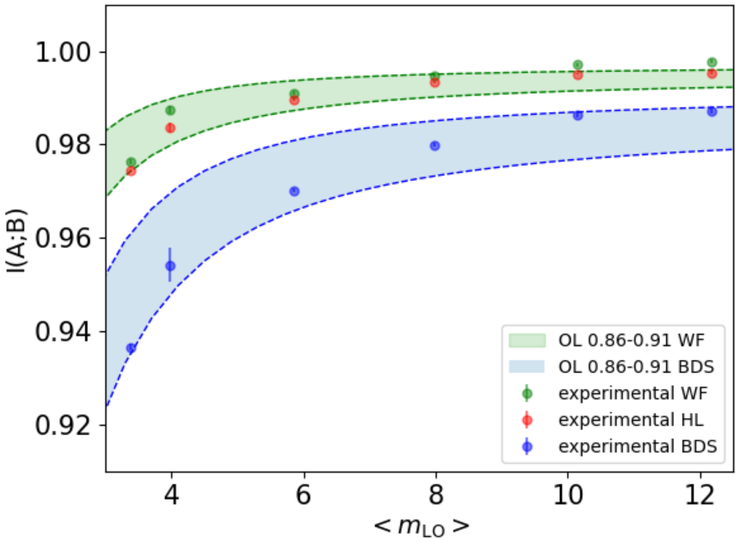

Figure 2.11: Mutual information as a function of the LO intensity in the case of WF (green), HL (red) and BDS (blue). $\langle m_{sig} \rangle = 3.07$

2.3.4 Introduction of losses

Once the signal and LO have been characterized in order to optimize the performance of the hybrid detector, we investigate its behavior by implementing some losses along the channel. To perform the experiment, the LO intensity was fixed at $\langle m_{LO} \rangle = 12.15$ photons and the initial signal intensity at $\langle m_{sig} \rangle = 3.20$ photons. To simulate the introduction of losses, the intensity of the signal was reduced using the variable neutral density filter in the setup. The minimum signal intensity collected was $\langle m_{sig} \rangle = 0.14$ photons. The overall losses, measured in dB, correspond to 13.44 dB.

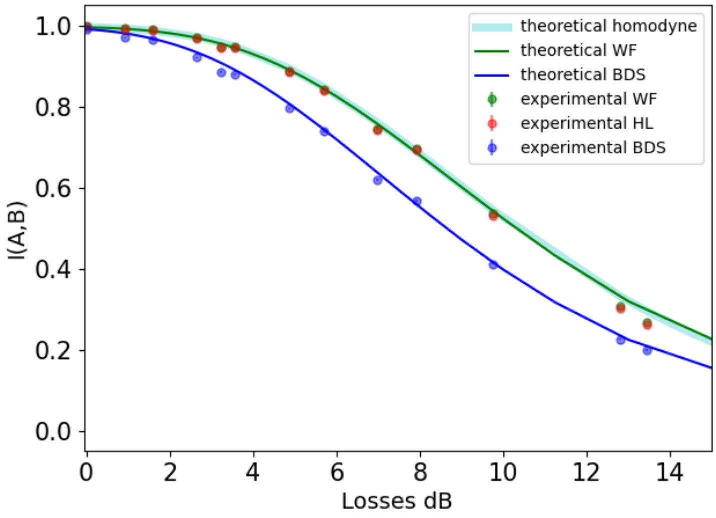

Figure 2.12:
as a functio
duced on the
of WF (green
(blue).

The experimental results are reported in Figure 2.12. The solid lines represent the theoretical behavior, while dots (green for WF, red for HL and blue for BDS) represent the experimental data. The estimated overlap in these measurements is $\xi = 0.94$, the theoretical curve has been calculated accordingly. Also in this figure we can observe the perfect agreement of the data related to WF and HL strategy, while BDS has a faster decrease.
In this context we decided to perform a simulation with a standard homodyne detector having the same characteristics, in terms of overlap, as the one we realized. In the plot it is represented by the light blue transparent line in agreement with the HL and WF results.
Also in Figure 2.12 the theoretical behavior of HL has been removed, being indistinguishable from the WF curve.

2.3.5 Towards communication

In this work we tried to give a first proof-of-principle of the suitability of this detector in the context of CV-QKD. In fact, under the assumption of a wiretap channel, we calculate and compare the mutual information shared by Alice and Bob, as well as the one gained by an eavesdropper Eve who has access to all and only the channel losses.
Basically, this is the same acquisition performed in the previous section, at variance of the neutral filter on the signal arm, but we assume that all the losses are collected by a third part. Since we have already shown that WF is, in principle, the processing strategy that allows to share more information, it is the only strategy we consider here. We can expect HL to perform accordingly, like in the previous analysis.
Let's first consider the scenario of individual attacks. In this case, the information acquired by Eve is the mutual information calculated in terms of Shannon's entropy. We consider both the direct and reverse reconciliation strategies, so that we can compare the two scenarios.
In panel (a) of Figure 2.13 are reported the values of mutual information obtained at variance of losses. The green dots represent the mutual information shared by Alice and Bob. If they chose to perform direct reconciliation, the information acquired by Eve is the mutual information between Eve and Alice, represented by the black dashed line. Conversely, if Alice and Bob perform reverse reconciliation, the

information gained by Eve is measured by the mutual information between her and Bob, shown as purple dashed line in the plot. Since we are not implementing any specific

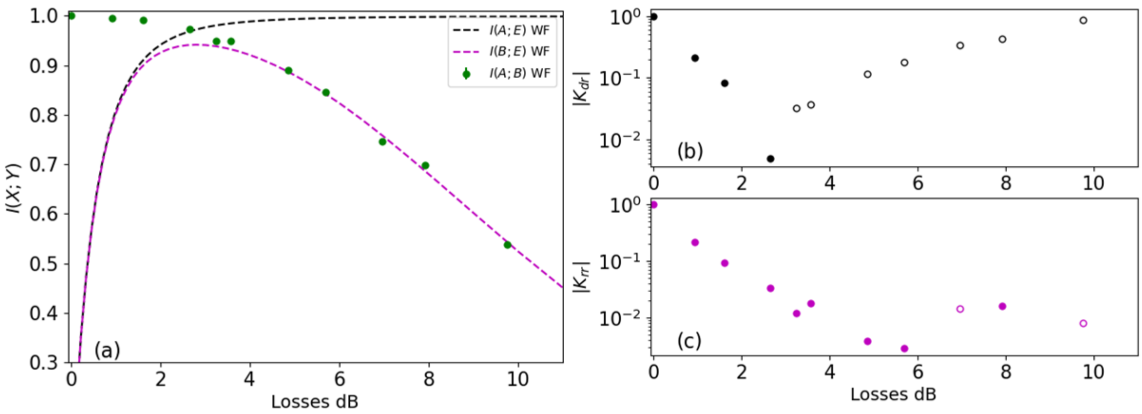

Figure 2.13: Individual Attack. (a): Mutual information shared by Alice and Bob (green dots), Alice and Eve (black line) and Bob and Eve (purple line) at variance of losses. (b) $|K_{DR}|$ as function of losses.(c) $|K_{RR}|$ as function of losses.

protocol, we are only interested in evaluating for which losses $I(A;B) > I(E;A/B)$. It can be observed by panel (a) that RR allows Alice and Bob to share more information than the one acquired by Eve for higher values of losses. To better observe this, we define a new quantity, K, that represents the normalized key generation rate.

$$K_{DR} = \frac{I_{WF}(A;B) - I_{WF}(A;E)}{I_{WF}(A;B)}$$

$$K_{RR} = \frac{I_{WF}(A;B) - I_{WF}(B;E)}{I_{WF}(A;B)}$$

The values of losses for which the above-mentioned condition is fulfilled is when $K > 0$. In panels (b) and (c) of Figure 2.13 are reported the absolute values of the normalized key generation rate for direct and reverse reconciliation respectively. The positive values are reported with full dots, while open circles represent the negative values. These plots highlight the better efficiency of reverse reconciliation with respect to the direct one. In fact, as predicted from theory, in the case of direct reconciliation the mutual information drops to zero for 3 dB of losses.

To conclude this analysis, we performed a comparison between the KGR (non normalized) obtained by the WF strategy and the one achieved with the standard homodyne detector. Both the curves are calculated from a numerical simulation. The results are reported in Figure 2.14, where the WF data are represented by dots and the homodyne behavior is the solid light line, green for direct and blue for reverse reconciliation respectively. We can observe that the green curves are in good agreement, while the blue ones have some discrepancies for high values of losses (~ 9 dB).

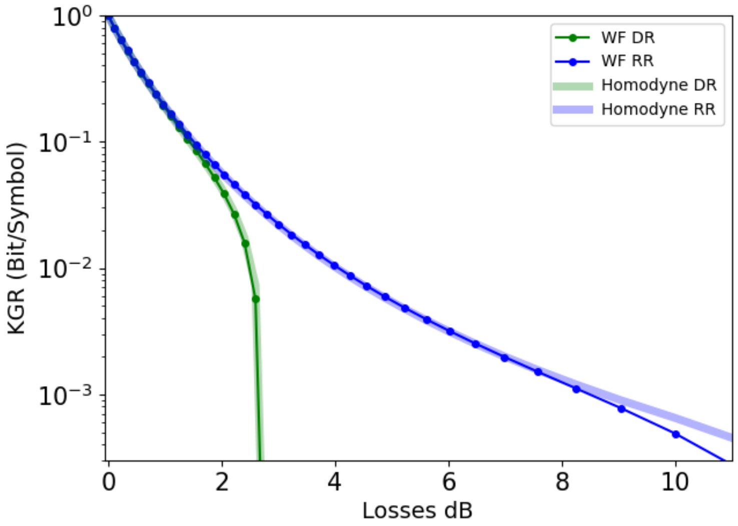

Figure 2.14: Key generation rate as a function of the losses introduced for WF and standard homodyne in the direct (green) and reverse (blue) reconciliation scenario.

The last part of this work involves the investigation of collective attacks from Eve. We decided to take into account the most effective reconciliation, that is the reverse one. We want to compare the same scenario in the case of WF strategy and BDS one. The mutual information between Alice and Bob is reported in panel (a) of Figure 2.15 as green dots in the case of WF strategy and blue dots for BDS one.

In this scenario the information stolen by Eve is represented by the Holevo information between Eve and Bob, $\chi(E;B)$. Of course, this is calculated according to the chosen post processing strategy, as mentioned in the theoretical description. In Figure 2.15 (a) the Holevo information is represented by the dashed lines, again green for WF and blue for BDS.

Also in this context we define the normalized KGR, that reads

$$K_{WF/BDS} = \frac{I_{WF/BDS}(A;B) - \chi_{WF/BDS}(E;B)}{I_{WF/BDS}(A;B)}$$

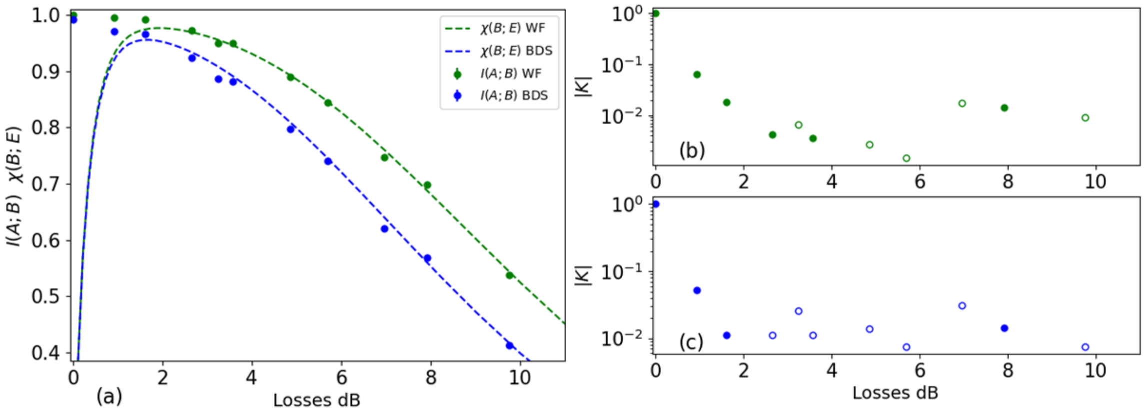

Figure 2.15: Collective Attack. (a): Mutual information shared by Alice and Bob (green dots WF, blue dots BDS), Mutual information shared by Eve and Bob (green dashed line WF, blue dashed line BDS) at variance of losses. (b) $|K|$ as function of losses for WF.(c) $|K|$ as function of losses for BDS.

In panels (b) and (c) are reported the absolute values of K in the case of WF and BDS, respectively. Again, full dots represent the positive values of K and open circles represent the negative ones.

From this figure we can observe not only that, given the same losses, BDS leads to lower values of $I(A;B)$ than WF, but also that K is positive for less than 2 dB of losses. In this scenario we can conclude that the WF is the best strategy for Alice and Bob to share information.

Finally, also in this case we perform a numerical comparison between the WF strategy and the standard homodyne. Again we compare the KGR of the two detectors as a function of losses. The results are reported in Figure 2.16, where purple dots represent the WF simulated data, while the light purple solid line represents the simulated homodyne detection.

We can observe that also in this case the two curves are in agreement. The comparisons with the standard homodyne detector enforce the belief of the suitability of this detector to quantum communication applications.

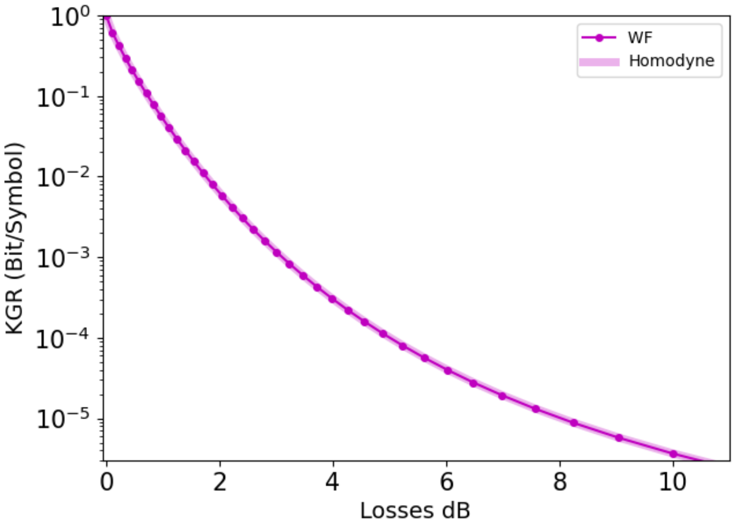

Figure 2.16: Key generation rate as a function of the losses introduced for WF (dots) and standard homodyne (solid line).

2.4 Conclusions

This is the first proof-of-principle experimental work that investigates the feasibility of a SiPM-based interferometric detector and its suitability in the context of quantum communication. We characterized the optimal phase shift for a BPSK protocol and defined the three possible post processing strategies (WF, HL, BDS) of the outputs. In terms of mutual information, we can say that the best strategy to use in a CV communication scheme is WF. We presented a first investigation of the detector under the wiretap channel hypothesis, and demonstrated the regime in which it allows to share information. Moreover, we used numerical simulations to compare the behavior of the WF strategy and that of the standard homodyne detector, showing that they are in nice agreement. These results suggest the suitability of the detection for actual communication schemes, perhaps based on more complex alphabets, even though a real experimental implementation has to be performed yet.

3 Through a four-phase coding

In this chapter we present the very last part of my PhD project. In fact, even though it is reported in the third chapter, this work began in July of my last year as a PhD student. This work is meant to be a starting point to generate a four-symbol alphabet based on phase displacement. In these pages the description of the experimental implementation and some preliminary results are shown.

3.1 Theoretical development

In the previous chapter, we have demonstrated the experimental realization of a hybrid interferometric detector based on SiPMs and characterized its performance using a binary alphabet. Such an alphabet, based on the use of two symbols, results in being robust to loss occurrence [1] but, on the other hand, less efficient in coding information. In fact, if we fix the size of an alphabet M [2] [3], the information in terms of bit per symbol is defined as

$$I = \log_2 M$$

It is obvious then that by increasing the alphabet size, the communication channel would increase its efficiency [4].
In this work we want to investigate the implementation of a four-phase alphabet. The aim is to verify whether it

1: [41] Matthew T DiMario et al., *npj Quantum Information*, p. 65 (5), (2019)

2: [42] Francisco E Becerra et al., *Nature Photonics*, pp. 147–152 (7), (2013)

3: [43] Francisco E Becerra, Jingyun Fan, and Alan Migdall, *Nature communications*, p. 2028 (4), (2013)

4: [44] Denis Sych and Gerd Leuchs, *New Journal of Physics*, p. 053019 (12), (2010)

---

[0] Background photo: Interferometric fringes.

is possible to increase the transmitted information using our hybrid detector. We attempted to double the coding alphabet, so to have four symbols. In this case the maximum information per symbol is 2 bits. Also in this context, we will be working with phase-shifted coherent states, but instead of applying a phase shift of π to the initial state, we apply three phase shifts of $\frac{\pi}{2}$. At difference with the states $|\pm\alpha\rangle$ reported in the previous chapter, here we introduce a fixed phase shift to all the four states. As represented in Figure 3.8, this allows to have four states always distinguishable on both quadratures [5].

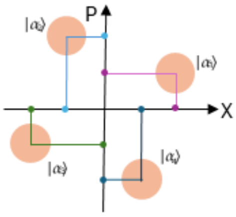

Figure 3.1: Sketch of the four states.

More specifically, we decided to introduce a phase shift of $\frac{\pi}{8}$. The work reported here is meant to represent the first steps towards a much more complex scheme, that mimics heterodyne detection. Namely, a double homodyne, that gives access to both the field quadratures. In fact, this is the only detection scheme suitable to discriminate states upon a phase and amplitude modulation. Of course, the main limit to such an implementation is the phase control and phase noise sensitivity of the system. In fact, since both phase and amplitude modulations are perceived by the detectors as an intensity variations, it is important to have the maximum possible control over these two variables used to encode our secret key [6].

In this work we present a first, maybe näive, generation of 4 phase-shifted coherent states and try to characterize the phase noise introduced in our setup, as a first progress in understanding the best operative procedure.

3.2 Experimental Setup and Data Acquisition

In this section we give a schematic description of the experimental setup realized in the laboratory.

As reported in Figure 3.2, the setup is developed in bulk optics. An exception is made for the detection phase, where the light is collected by optical fibers. The light source is a solid-state Becker & Hickl pulsed laser. The pulse duration is on the order of tens of ps, depending on the repetition rate, and the output wavelength is 515 nm. The built-in pulser gives access to quite high repetition rates (at least 20 MHz),

---

[5] [45] Michele N Notarnicola et al., *IEEE Transactions on Communications*, pp. 375–386 (72), (2023)

[6] [46] Giulio Colavolpe et al., *Journal of Lightwave Technology*, pp. 2790–2800 (29), (2011)

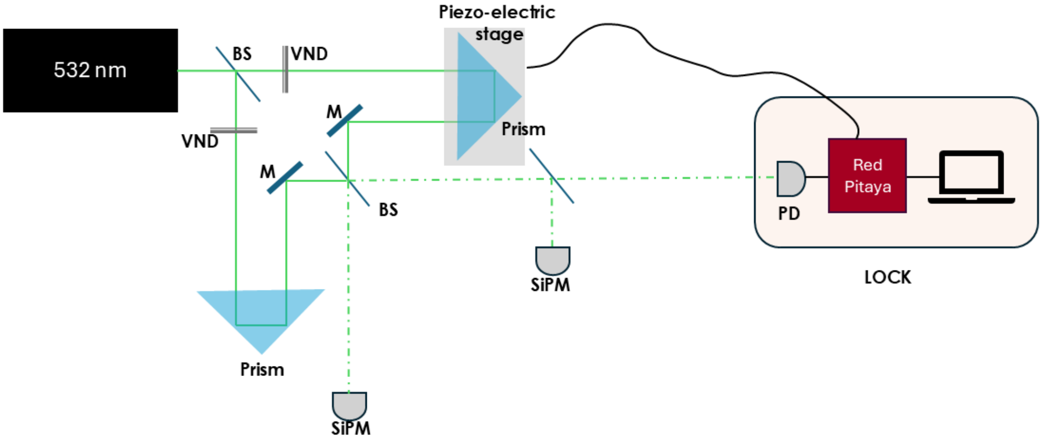

Figure 3.2: Sketch of the experimental setup.

that we have already explained to be too fast for our acquisition chain. To overcome this problem, we triggered both the laser source and the acquisition with an external pulse picker, so that the laser is operated at a repetition rate of 0.5 MHz and the acquisition is set to have a repetition rate of 5 kHz. We have verified that, despite the different repetition rates, the light emission and the acquisition happen simultaneously. The reason for this discrepancy stands in the fact that also the laser intensity, as well as the pulse duration, changes with the repetition rate. In the setup, as explained further, we introduced a feedback loop to stabilize the interferometer, and its setting requires a certain amount of light, which is generated by operating the laser at a high repetition rate (i.e. ≈ 1 MHz).

Also in this case we use a Mach-Zehnder interferometer to create the signal and LO beams and to make them interfere before the detection. At first, the laser light is split at a balanced BS, so that one arm will be manipulated as a signal and the other one will be the LO; the two light beams are recombined at a second BS. The intensities of the two fields are controlled through variable density filters.
The rectangular prism of one arm is placed on a micrometer stage, so that it can be used to optimize the interferometer, while the other is mounted onto a piezo-electric stage, con-

nected to a feedback system that preserves the setup stability. In fact, since in the previous experiment the uncontrolled experimental drifts were a great obstacle to the achievement of proper results, in this case we decided to lock the fringe phase. To do so, we used a Red Pitaya device, connected to a computer, where it was possible to monitor the fringe stability using a PID control [7] (actually our device was only provided with the proportional and integral controls). The input signal of this feedback system is given by the output of a photodiode placed on the transmitted arm of a third BS, as shown in Figure 3.2.

We also used this system to shift the phase from a generic ϕ to $-\phi$. In fact, by changing the sign of the proportional and integral parameters control, the two fringes would swap. This procedure was not precise enough, so some alignment adjustment was required.

To exclude side fringe contributions to the detection, two variable irises were placed in front of the two optical fibers (multimode, 1 mm core) connected to the SiPMs.

Once again, we remind the reader that the acquisition chain is fully described in Section 1.3.3 of Chapter 1, with the only difference of the external trigger used in this case. During these acquisitions the operating voltage was 56 V, the amplifier gain was set at 17 dB and the boxcar integration gate was set at 10 ns.

For each acquisition value reported in the following section, a series of $2 \cdot 10^5$ pulses was acquired.

3.3 Experimental Procedure and Results

3.3.1 Lock Characterization

Before performing the data acquisition and data analysis, we characterized the effectiveness of the lock procedure in terms of noise.

In Figure 3.3 we show a temporal trace of the fringe intensity acquired by the photodiode in the case the lock is turned off (left) or on (right). The comparison of these two plots allows us to see that the difference between the two traces is minimal; in fact, the intensity acquired with the lock is slightly less noisy than the other one.

This is just a first comparison to show the consequences of

---

[7] https://pyrpl.readthedocs.io/en/latest/

the lock on the intensity stability, even though we admit we expected a more effective performance.
To give a numerical evaluation of the noise, we chose to lock the fringes at an intensity that is half the measured maximum, 0.5 V. Once this condition was set, we calculated the mean value and the standard deviation upon three different measurements. In the case of unlocked fringes we obtained $\bar{m} = 0.53 \pm 0.07$, while the locked case gave $\bar{m} = 0.50 \pm 0.06$. Thus, the improvement provided by the lock is barely observable, but there is a physical reasons that explain this result: the piezo mount is quite heavy and its response is limited around 10 Hz, therefore it is forbidden to compensate higher frequency noise. Moreover the lock implemented allows to avoid experimental drifts by fixing the fringes mean value during each acquisition.
By knowing the intensity variation corresponding to a π phase shift, we could calculate the phase noise in both cases. This corresponded to 0.28 rad for the unlocked system and reduces to 0.24 rad when locked. This means that, even though a small improvement is observable, the phase noise is far from being negligible also when the lock is on. Conversely, it is quite relevant and will surely affect the state acquisition and reconstruction.

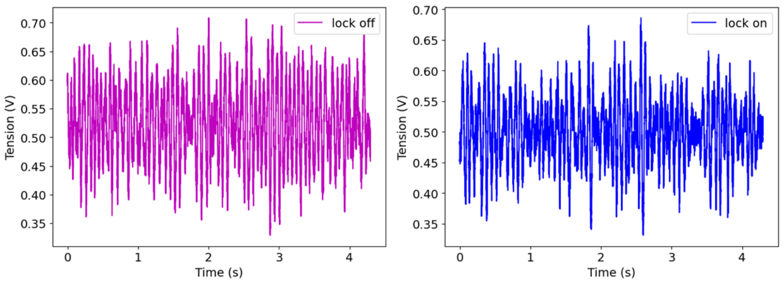

Figure 3.3: Temporal traces. **Left**: lock off. **Right**: lock on.

To better understand the lock behavior, using the Red Pitaya control, we acquire the spectra of the input signal with and without the lock, comparing it to the reference noise. The spectra reported in Figure 3.4 are obtained by averaging 10 temporal signals before the acquisition. The black line represents the reference, obtained by acquiring a coherent state (no fringes), while the cyan vertical line at 1 Hz has been drown to emphasize the saturation for lower frequencies. The

magenta line corresponds to the mean spectra of 10 unlocked interferometric signals while the blue line is the mean of 10 locked signal spectra.
Also from this image we can observe the minimal reduction

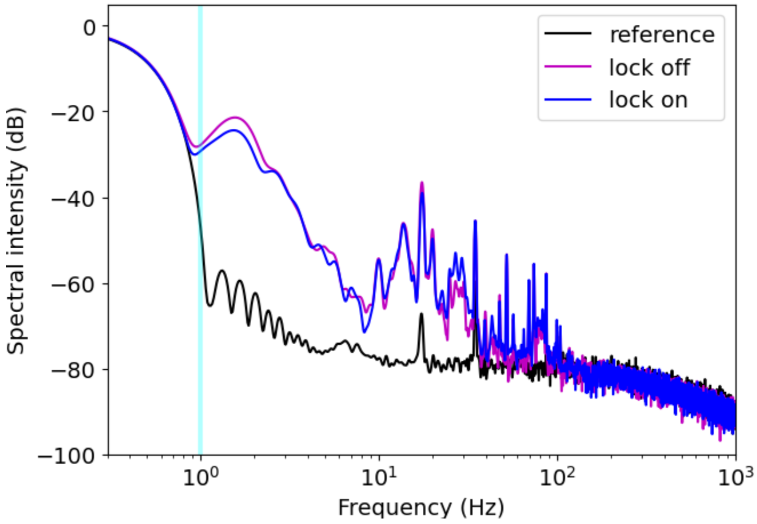

Figure 3.4: Acquired averaged spectra: reference (black line), unlocked (magenta line) and locked (blue line).

of noise introduced by the lock, but the locked spectra is still much above the reference noise. Moreover, this reduction is appreciable only along the region between 1 and 2 Hz. This is due to the fact that our system is quite slow, so it is capable of compensating only low frequencies. On the other hand, as a consequence of the fact that we are not measuring the feedback error signal, to which we have no access, but the photodiode output, the low-frequency region is saturated by the DC component.

To better understand the behavior of the lock at low frequency, we performed a spectral analysis of the acquired time signals, comparing the case of lock on and lock of to the same reference signal as before.
For every condition we acquired three time signals (acquisition time ~ 4 s). Each segnal has been subtracted of its mean value and Fourier-transformed.

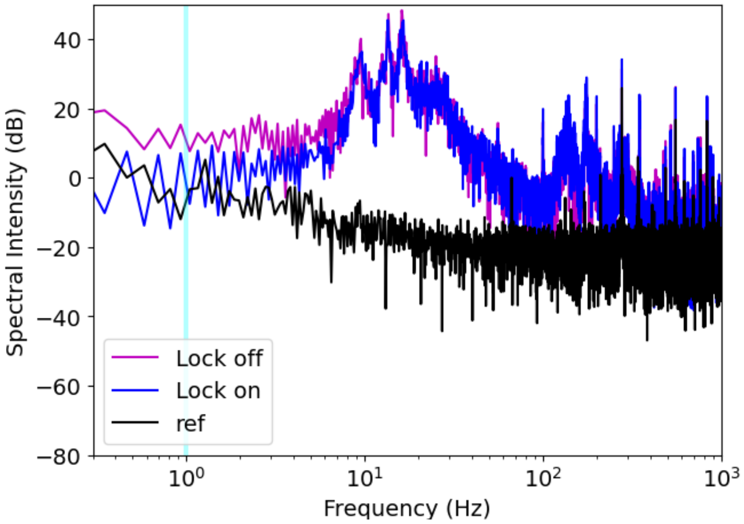

Figure 3.5: Calculated spectra: reference (black line), unlocked (magenta line) and locked (blue line).

In Figure 3.5 the average of the three Fourier transforms absolute values for each condition are reported. Also in this case the black line corresponds to the reference, the magenta line to the lock off condition and the blue line to the lock on configuration. A vertical cyan line is displayed to represent the 1 Hz frequency, so to ease the comparison with the previous plot. Also in this case we can observe the slowness of the lock device, that performs some noise correction only for frequency lower than 100 Hz. Moreover, we confirm that such a correction is not enough to approach the reference limit.

This characterization of the lock system shows the main limits of the equipment already present in the lab. In order to perform some real and precise multiphase encoding we need to minimize environment noise (table vibration, acoustic noise) and improve the piezo correction bandwidth, for example using a piezoelectric element directly glued to a small mirror, instead of a piezo-driven translation stage. Nevertheless, we want to perform a proof of principle in order to test our hybrid detector in a more complex scheme, being aware that the results could only be improved by more precise instruments. Even though the noise reduction induced is still not enough, we chose to use the lock during the measurements so that the experimental drifts are kept under control. The implementation of the feedback control device allowed to have more stable, even if too noisy, fringes.

3.3.2 Phase Characterization

To perform such a measurement, we first placed the detectors on the fringes representing one of the states $|\pm\alpha\rangle$. We acquired the mean values for the maximum and minimum of both states. These values allowed us to determine the expected intensity values for the desired phase shift, corrected for the imperfect visibility. To set the phase shifts (also from $|+\alpha\rangle$ to $|-\alpha\rangle$), we fixed different parameters of the PID control. This procedure alone was not enough to obtain the exact desired values, so some small adjustments in the setup were required for each measurement.

In this work we aim at comparing the results obtained using $|\pm\alpha\rangle$, shifted by π, and four states generated by applying to $|+\alpha\rangle$ the following phase shifts: $\phi_1 = \frac{\pi}{8}$, $\phi_2 = \frac{\pi}{2} + \frac{\pi}{8}$, $\phi_3 = \frac{3\pi}{2} + \frac{\pi}{8}$, $\phi_4 = -\frac{\pi}{8}$.

According to what we have already reported in the previous chapter, we fixed the LO intensity mean value and varied the signal mean value, being careful to always work in the homodyne limit.

Let's begin with reconstructing the Skellam distribution in the two cases. Here, we report the results for the most and the least intense signal. The most intense acquisition was collected with mean values $\langle m_{sig}\rangle = 4.13$ photons and $\langle m_{LO}\rangle = 12.43$ photons while the least intense one had $\langle m_{sig}\rangle = 1.78$ photons and $\langle m_{LO}\rangle = 12.79$ photons.

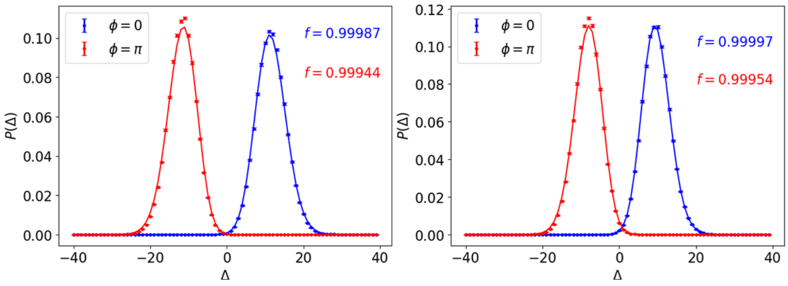

Figure 3.6: Skellam distribution of the states $|\pm\alpha\rangle$. Dots represent the experimental data, while solid lines are the theoretical curves. **Left**: $\langle m_{sig}\rangle = 4.13$, $\langle m_{LO}\rangle = 12.43$. **Right**: $\langle m_{sig}\rangle = 1.78$, $\langle m_{LO}\rangle = 12.79$.

The fact that one experimental distribution (the red one) is slightly higher than the other (the blue one) is a consequence of the fact that the maximum intensities measured by the two SiPMs are not equal; in fact, one device always measures a little bit more than the other. Nevertheless, this just slightly

affects the distribution reconstruction, which is still in agreement with the theoretical expectation.
The same analysis has been performed for the 4-phase shift, as shown in Figure 3.7. In the figure, the experimental data are represented as dots, while the theoretical expectations are displayed as solid lines. Also in this case, according to the fidelity test, the agreement between the curves is acceptable. By comparing Figure 3.6 and Figure 3.7, it is evident that the error probability increases with the number of phase shifts. This is the reason why it is necessary to improve the control on the phase setting and reduce the phase noise to the minimum. Even though the implementation of a double homodyne detector will largely increase the effectiveness of reconstructing the encoded state, because we would have state discrimination on both quadratures, the main constraint to this setup consists in its sensitivity to phase noise.

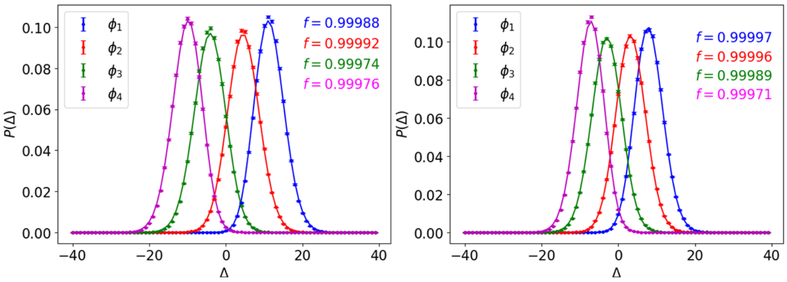

Figure 3.7: Skellam distribution for the ϕ_1, ϕ_2, ϕ_3, ϕ_4 phase shifts. Dots represent the experimental data, while solid lines are the theoretical curves. **Left**: $\langle m_{sig} \rangle = 4.13$, $\langle m_{LO} \rangle = 12.43$. **Right**: $\langle m_{sig} \rangle = 1.78$, $\langle m_{LO} \rangle = 12.79$.

3.3.3 Mutual Information

As a last characterization, similarly to what was reported in Chapter 2, we performed an analysis at variance of the signal value, simulating the introduction of losses along the channel. In this case we want to compare the experimental results with the theoretical expectation for the weak-field strategy and the corresponding standard homodyne behavior.
The analyzed dataset is composed of seven different signal intensities, each of which has been acquired in four measurements of $5 \cdot 10^4$ data. From each measurement we calculate the mutual information, then average it over the four repetitions.

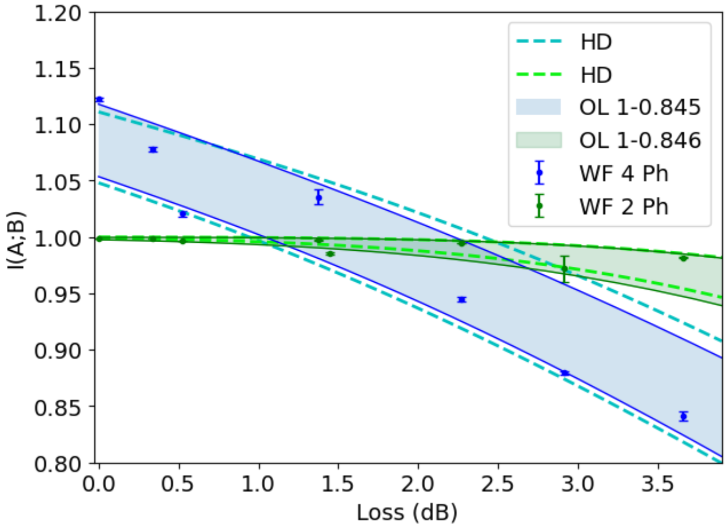

Figure 3.8: Mutual information as a function of losses in the case of BPSK (green) and 4-phase shift (blue). Solid lines represent the theoretical WF expectation; light thick lines the simulated homodyne behavior.

We compare the WF mutual information in the case of BPSK with π-phase shift to the case of 4-phase shift values. The results are shown in Figure 3.8, where BPSK is represented by the green data and the 4-phase shift by the blue data. We calculated the theoretical WF behavior, introducing the phase noise that characterizes our setup in the model. As a consequence of how we performed the measurements, and including some imperfections in the setup, similarly to what we did in Chapter 2, we added the term of overlap ξ. Since each measurement is characterized by a different overlap, we decided to show the theoretical curve for the higher ($\xi = 1$) and the lower ($\xi = 0.845$). We can observe that all the data are within the band delimited by these curves. In the plot, the theoretical curves are represented by the thin, dark solid lines (green and blue respectively). Furthermore, to complete the analysis, we performed a comparison with a simulated standard homodyne detector in both cases under the assumption of same phase noise and overlap as the WF theoretical curves.

From Figure 3.8 we can observe that, for loss values lower than 2 dB, the mutual information obtained by the 4-phase shift is higher than the one obtained with the BPSK. This result was already predicted in the first section of this chapter, even if the experimental limitations currently reduce the advantage of this strategy since the values of mutual information obtained are lower than expected. Such a behavior is expected also in the case of standard homodyne detection, as it can be observed from the plot.

In general, for low values of losses (in a standard fiber communication, generally corresponding to short distances) the 4-phase shift encoding performs better than a standard BPSK. Moreover, for shorter distances we can observe that the 4-phase WF technique performs better than the standard homodyne, being all the parameters the same.

3.4 Conclusions

We could describe this chapter as a characterization of the setup built to generate a 4-phase shift to encode information. The results of this characterization brought up the fact that there are some improvements required in the procedure and the equipment to perform a reliable and repeatable measurement. In particular, the current phase noise level is detrimental to the measurements. Nevertheless, even with all the experimental limitations, we managed to achieve a first characterization of the behavior of our WF detector in the case of 4-phase shift, comparing the results with the already studied BPSK and a simulated standard homodyne detector. The obtained results are promising and suggest that, upon some improvement, such an encoding could be suitably recognized by our detector that, under some conditions, could perform even better than the standard homodyne detector.

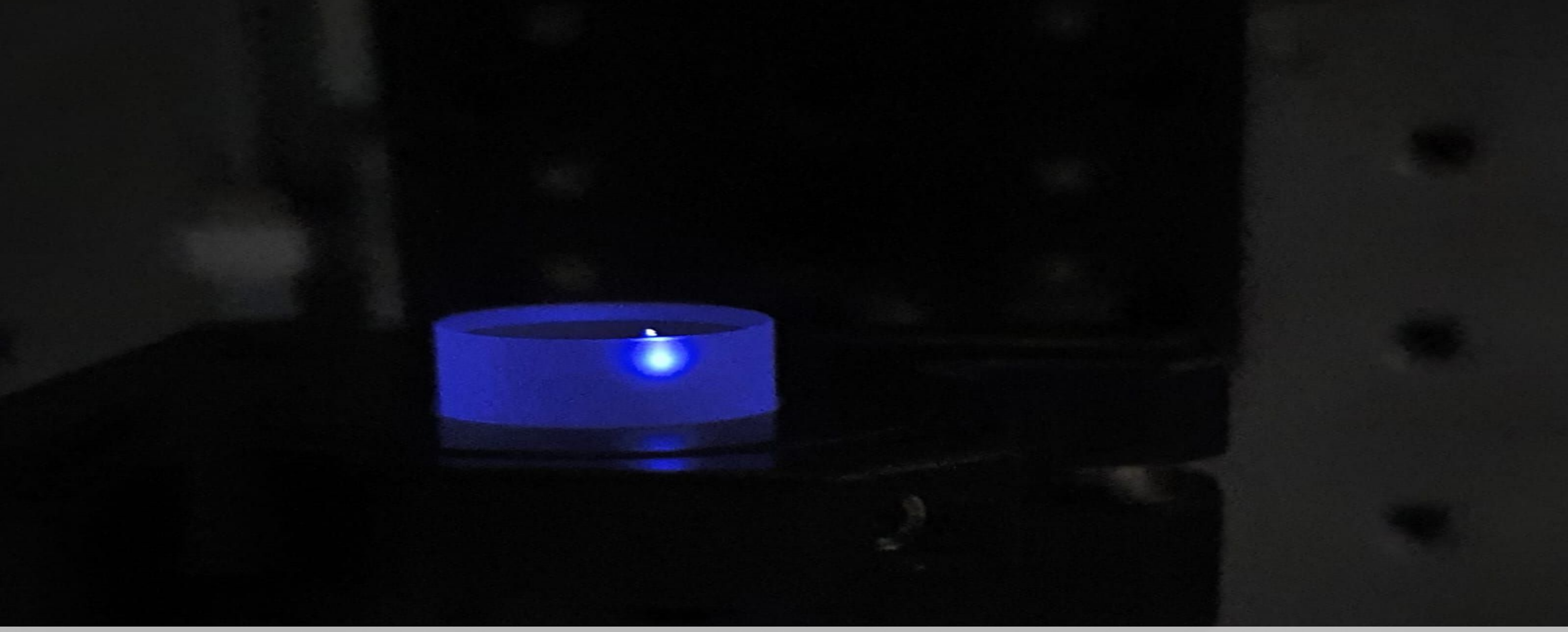

4 SiPMs at telecom wavelengths

In this chapter the realization of an up-conversion-based detector, that would allow the use of SiPMs at the standard fiber-compliant communication wavelengths, is reported. The results obtained have been collected in two different papers and submitted to APL Photonics and Optics Express, respectively.

4.1 Introduction

As the reader might have noticed, all the characterization of SiPMs in the communication context presented in the previous chapter has been performed using a visible laser source (515 nm). Of course, as long as we are performing proof-of-principle measurements this is no issue, but in order to evaluate the effective use of these devices in real applications we should ask ourselves whether the employed wavelengths are suitable for the current standard requirements. For instance, there are some examples of communication protocols, such as those for underwater communication, that exploit visible wavelengths because they are less absorbed in the propagation medium. These protocols typically exploit free-space propagation, since in some contexts it is not easy to place the infrastructures required for fiber communication. The maximum distance covered by this technology amounts to less than 100 m depending on the water cleanliness and,

---

[0] Infrared beam focused into a YAG crystal to generate WLC.

in general, is used to connect nearby underwater drones or buoys. Considering the wavelengths involved, typically in the blue-green range, and the detector efficiency in that spectral region, we could consider the application of our homodyne-like detector in such a context. On the other hand, this corresponds to a very small part of the communication scenario; the largest information travels worldwide through optical fibers and satellite transmission infrastructures. These exploit a different spectral region, that involves near and far infrared wavelengths. Focusing on the standard optical fiber communication, the spectral region typically exploited is the so-called C band, centered around 1550 nm [1] [2]. The basic idea of this work is to evaluate if our hybrid interferometric scheme based on SiPMs could be of use in this context. Off the top of one's head the answer should be no, since silicon is transparent to infrared (IR) wavelengths, therefore no avalanche is supposed to be generated in the detector. On the other hand, we could make use of nonlinear optical interaction to up-convert an IR beam to a wavelength the detectors are sensitive to [3] [4]. Ça va sans dire, that's exactly what we tried to do. We generated a pulsed coherent beam at around 1550 nm and, using a sum-frequency process, we converted it into a beam that preserves the same properties but is detectable by SiPMs. The reason why we chose sum-frequency generation as a nonlinear process is because it is demonstrated not to alter the statistical properties of the input signal, in contrast with other possible phenomena such as second-harmonic generation [5] [6]. In this chapter the theory of such phenomena is not reported, since it has already been presented in the first one. In the following section the results obtained from this characterization are shown.

4.2 Experimental Setup

The setup realized in this experiment is quite complex, since also the 1550 nm laser pulses needed to be generated. A first representation of the experimental setup is shown in Figure 4.1. The laser source is a Yb:KGW pulsed laser, with fundamental wavelength at 1038 nm and pulse duration of 190 fs. It is provided with tunable repetition rate and external harmonic module to generate second and third harmonics. First of all, we realized a telescope on the laser output to reduce the beam diameter by about one third and keep the

[1] 1: [47] WeiJun Zhang et al., *Science China Physics, Mechanics & Astronomy*, p. 120314 (60), (2017)

[2] 2: [48] Joe C Campbell, *Journal of Lightwave Technology*, pp. 109–121 (25), (2007)

[3] 3: [49] Enrico Pomarico et al., *Optics express*, pp. 10750–10759 (18), (2010)

[4] 4: [50] Kun Huang et al., *Photonics Research*, pp. 259–265 (9), (2021)

[5] 5: [51] JL Debethune, *Il Nuovo Cimento B (1971-1996)*, pp. 101–117 (12), (1972)

[6] 6: [52] Pavel Chmela, Zbigniew Ficek, and Stanislaw Kielich, *Czechoslovak Journal of Physics B*, pp. 509–528 (39), (1989).

beam suitably collimated. As already mentioned, the first part of the setup is aimed at the generation of telecom wavelength pulses, while the second part involves the up-conversion process and detection.

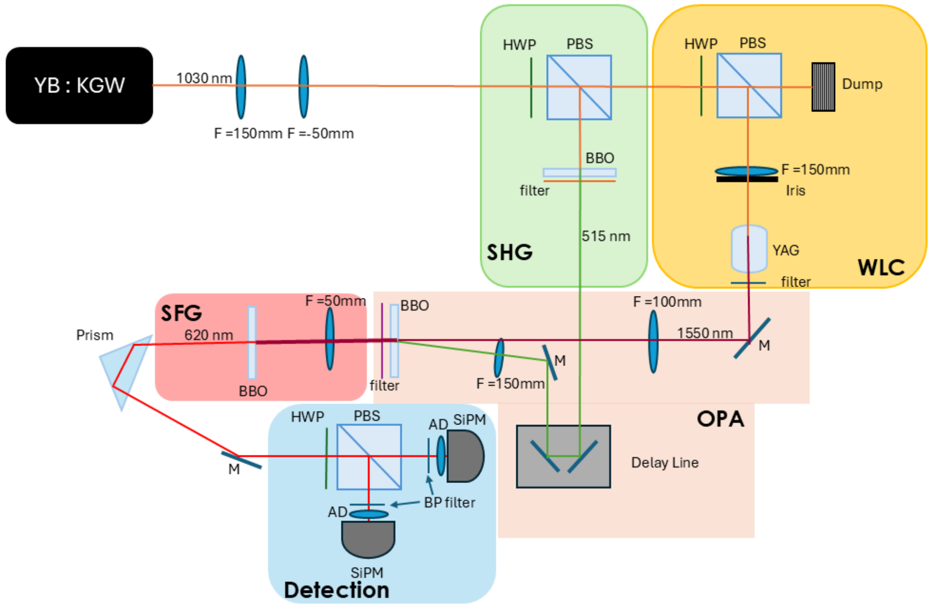

Figure 4.1: Sketch of the collinear experimental setup.

In order to generate C band pulses, we exploited a nonlinear $\chi^{(3)}$ phenomenon that is white-light continuum (WLC) generation . The realization of WLC [7] requires the laser beam to be suitably focused and spatially filtered in a 1 cm long YAG crystal. This is why in front of the crystal a lens (f=150 mm) and an iris are placed. The iris aperture is set by improving the generated spectrum. In order to measure the WLC spectrum we used two different spectrometers, the first one is the AvaSpec-ULS2048x64-EVO from Avantes, which is sensitive to the UV-visible region. The measured spectrum is reported in Figure 4.2.

The theory of all the nonlinear phenomena involved in this chapter is reported in Chapter 1.

[7] [53] Andrea Villa et al., *OSA Continuum*, pp. 2837–2844 (4), (2021)

However, since we are interested in the infrared region of the generated spectrum, we also used the MiniSpectrometer TG-NIR: C11482GA from Hamamatsu Photonic, which is sensitive to the NIR region. The acquired spectrum is reported in Figure 4.3. Here, we notice that the generation at the wavelength of interest, namely 1550 nm, is very low, for sure not sufficient to be manipulated and detected. Therefore, we decided to amplify it using an Optical Parametric Amplifier

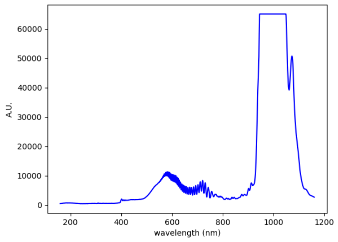

Figure 4.2: Visible spectrum of the generated WLC.

(OPA). To realize it, it was first necessary to generate the second harmonic (SHG) of the laser, in order to use it as a pump beam for the OPA. To this aim, we decided not to use the one provided by the builder, because it is limited to a maximum repetition rate of 3 kHz, that is its optimal setting. To perform the light generation and the setup alignment, more intense beams were required, that could be obtained using a higher repetition rate. In our case, the first alignment was performed at a repetition rate of 25 kHz; therefore, we chose to realize an SHG of a portion of the fundamental wavelength. As shown in Figure 4.1, before the WLC and SHG generation two polarizing beam splitters and half-wave plates are placed. This is because the sum-frequency generation is sensitive to the beam polarization and we must ensure to have the correct one, otherwise the up-conversion will not be generated. The half-wave plates also provide a control over the power used to produce each nonlinear process. As reported in the green box of Figure 4.1, the SHG at 515 nm is generated using a β-barium borate (BBO) crystal.

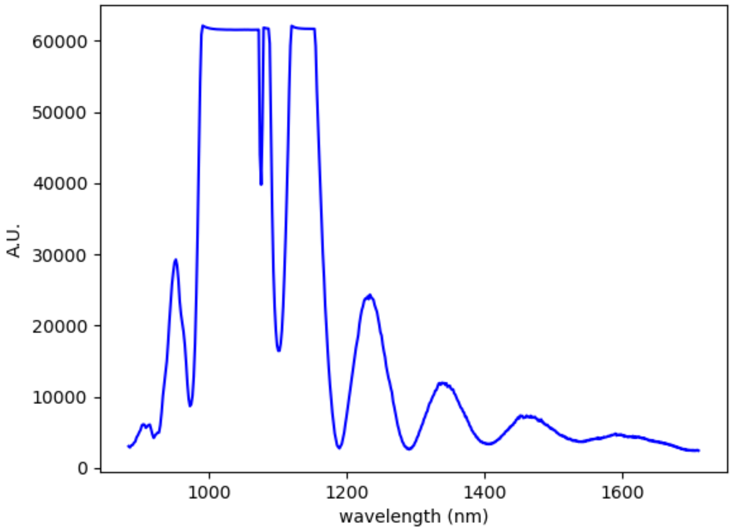

Figure 4.3: Infrared spectrum of the generated WLC.

This beam and the IR part of the WLC (filtered with a high-pass filter at 1000 nm) interact into a second BBO in a difference-frequency configuration, building a single-pass OPA [8]. To this aim, we chose a slightly noncollinear interaction geometry with focused beams. To make the interaction happen, it is fundamental that the optical paths of the two beams are identical. Therefore, we introduced a delay line on the SHG beam. To ensure finer control of the delay, the mirrors are placed on a micrometer stage movement.

[8]: [54] Francesco Gucci et al., *Optics Express*, pp. 48599–48609 (32), (2024)

The spectrum obtained by the amplification step is compared to the WLC one in Figure 4.4, where we can easily observe the amplification of the desired wavelength. In this first configuration, we decided to perform the Sum Frequency Generation (SFG) of the amplified beam and the overlapped residual pump, since it represents the simplest procedure to give a first proof of principle. To perform SFG, the amplified beam (and its residual pump) is focused (f=50 mm) into a third BBO crystal.

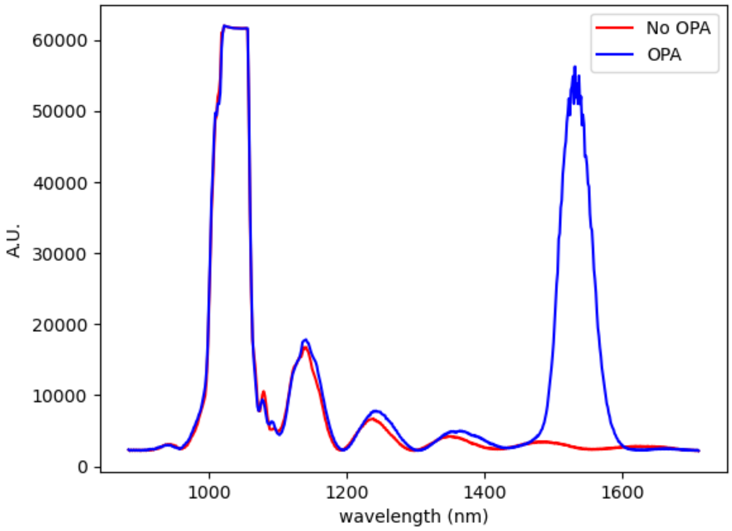

Figure 4.4: Infrared spectrum of the generated WLC overlapped to the OPA spectrum.

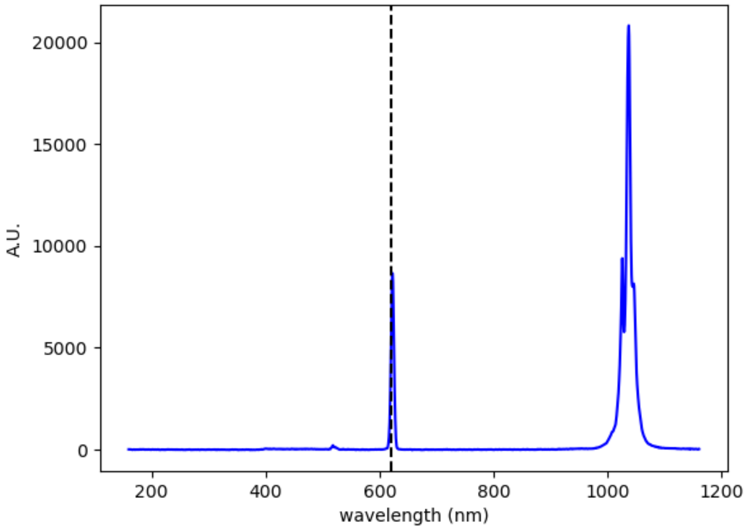

Figure 4.5: Spectrum measured after the up-conversion process.

The generated spectrum is reported in Figure 4.5, where we can observe the generated light at 621.7 nm and the residual pump as well. Since the spectrum is acquired with the Avantes oscilloscope, the residual of the 1550 nm beam cannot be observed in the plot.

The output wavelengths are then separated by a dispersion prism, so that only the generated red light reached the detector.

The detection part of the setup is represented by the light blue box of Figure 4.1. It is important to explicitly mention that in this context we did not perform any interferometric measurement. The light is split by a polarizing beam splitter (PBS) and collected by two SiPM detectors. The reason why we chose to use two detectors is that they give access to beam splitter correlations, which are a very powerful statistical tool. Before the PBS we placed a half-wave plate, that enables to balance the two PBS arms. To ensure the acquisition of the correct wavelength, in addition to the prism, we used two narrow filters (Thorlabs 620 ± 5 nm) placed in front of the achromatic doublets used to collect the light into the 1 mm core multimode optical fibers connected to the detectors.

What we described so far is the first experimental configuration we realized, aimed at evaluating the feasibility of the procedure and performing a first characterization of the generated light. In a communication context, the 1550 nm beam is supposed to be manipulated in order to encode some information, and such a manipulation should survive the up-conversion process. Such a modification should not affect the second field involved in the SFG process; therefore this cannot be the final configuration of such a setup. In fact, we overcame this issue by realizing a quasi-collinear SFG interaction using a portion of the fundamental beam at 1038 nm as the pump field in the SFG. A schematic representation of this second configuration is reported in Figure 4.7, where the part related to the generation of the 1550 nm beam has been simplified to give more emphasis to the quasi-collinear SFG. In fact, no modification has been implemented in the WLC generation, SHG, and OPA parts of the setup. The pump power at 1038 nm was set around 100 mW at 25 kHz during the alignment and kept fixed during the acquisition. Similarly to the OPA setup, also this one required the introduction of a delay line, so that the two optical paths resulted in the same length.

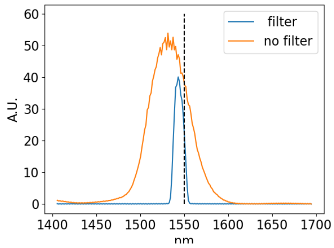

Figure 4.6: OPA output with and without the narrow filter.

On the other hand, in this case we wanted to extinguish the residual pump overlapped to the OPA output. Thus, we introduced a narrow filter (Thorlabs 1550 ± 6 nm) before the

SFG. A representation of the filtered spectrum of the 1550 nm beam entering the SFG process is reported in Figure 4.6.

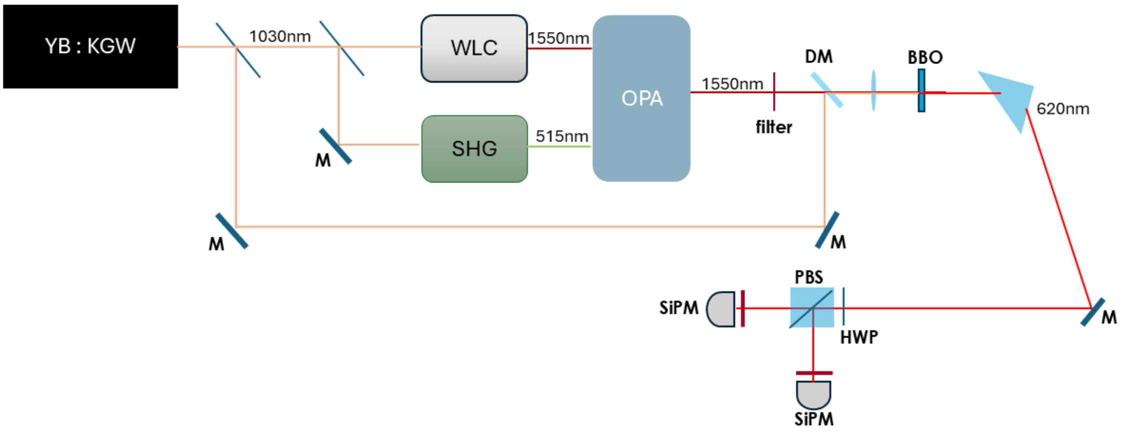

Figure 4.7: Sketch of the quasi-collinear experimental setup.

The use of a dichroic mirror, transmitting light at 1550 nm and reflecting light at 1038 nm, allowed us to perform an almost collinear SFG, as shown in the sketch above. The spectrum of the generated SFG, collected with one of the band-pass filters centered at 620 nm and placed in front of the fiber spectrometer, is reported in Figure 4.8.
Also in this configuration we used a prism and the two filters to remove any IR residual from the acquisition chain. Similarly to the first part of the setup, the acquisition chain had not been modified. For both the setups, the acquisition was performed at 3 kHz with the SiPM supply set at 56 V and the PSAU gain at 17 dB.

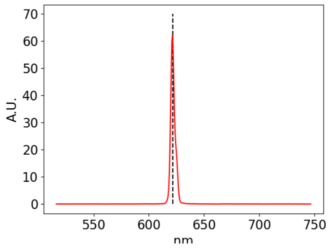

Figure 4.8: Spectrum of the SFG at 621.7 nm.

Before going to the results there are two considerations that are important to be made. The first one concerns the overall efficiency of this detector. To the best of our efforts, considering that we are not used to working at telecom wavelengths and our lab is poorly equipped with devices performing in this region, we used the spectrometer to measure the different intensity of the 1550 nm beam with and without the fundamental beam at the output of the third BBO. The measurement was performed keeping the tuning angle of the crystal fixed at the SFG phase matching angle, so that the

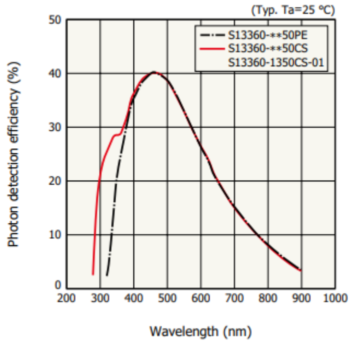

Figure 4.9: Photon detection efficiency for the SiPM in use in the experiment.

BBO absorption is fixed. The aim is to measure the amount of light involved in the nonlinear process. According to this measurement the SFG efficiency is about 10%. This has to be multiplied by the detectors' efficiency, which is around 25% according to the data sheet, as reported in Figure 4.9. This leads to an overall efficiency of about 2%. This is a lower estimation, since a proper measurement of the SFG efficiency could lead to a higher result, as well as some adjustments in the alignment of the setup. By the way, even if there is a lot of space for improvement, the efficiency of the setup is enough to perform suitable measurements.
The second consideration concerns the WLC, SHG and OPA part of the setup. As just mentioned, our lab is not provided with telecom equipment, such as a C band laser source; that is the only reason such a setup has been realized. It is of use in this proof-of-principle work, but for real applications a suitably pulsed laser source would be much more reliable and simpler to use.

4.3 Light source characterization

In this section we report the results obtained with the collinear configuration, where the SFG is performed between the OPA output and the overlapped residual pump. Since, as reported in the previous chapters, our final goal is to perform an interferometric detector to decode information from manipulated coherent states, from the 1550 nm generation process we expect to obtain coherent states, obeying a Poissonian photon-number distribution. In principle, WLC generation is not supposed to have a different statistic; the same holds for the OPA and SHG processes, that should not introduce any statistical modification to an input coherent state [9] [10][11]. On the other hand, when we started our measurements we had a very difficult time understanding why the measured fluctuations were so high that they would sometimes introduce PBS correlations. After several improvements in the isolation and stabilization of the setup in the laboratory that led to no significant improvements, we decided to test the power of the WLC pump. In fact, it is well known that it is a threshold process. We calculated the critical power (in terms of energy per pulse) for the generation, which is supposed to be less than 1 μJ. We decided to study the statistical properties of the detected states as a function of the WLC pump power.

Poissonian distribution

$$P(m) = \frac{\langle m \rangle^m}{m!} e^{-\langle m \rangle}$$

[9] [55] Leonard Mandel and Emil Wolf, *Cambridge University Press*, (), (1995)

[10] [56] Alessia Allevi and Maria Bondani, *Advances In Atomic, Molecular, and Optical Physics*, pp. 49–110 (66), (2017)

[11] [57] Werner Vogel, *Physical review letters*, p. 013605 (100), (2008)

We remind the reader that in this case we were just modifying the power of the 1038 nm beam focusing in the YAG crystal, but the light underwent all the nonlinear processes mentioned in the previous section and the characterization was performed acquiring the 621.7 nm up-converted beam. We acquired sets of data by varying the power of the laser intensity using the built-in attenuator. To perform the statistical characterization, not only did we reconstruct the probability distribution, but we also calculated the second-order Glauber auto- and cross-correlations [12]. The theoretical definition of the auto-correlation function reads:

$$g^{(2)}(n) = \frac{\langle : n^2 : \rangle}{\langle n \rangle^2} = 1 + \frac{F(n) - 1}{\langle n \rangle}$$

where $: \cdot :$ represents the normal ordering and $F(n)$ the Fano factor. We need to keep in mind that we are detecting photons, so we have access to the quantities $\langle m \rangle = \eta \langle n \rangle$, as explained in Chapter 1. Thus, the Fano factor for the detected photons becomes $F(m) = \eta F(n) + (1 - \eta)$. So, upon detection, the second-order auto-correlation function reads as:

$$g^{(2)}(m) = \frac{\langle m^2 \rangle}{\langle m \rangle^2} = 1 + \frac{F(m) - 1}{\langle m \rangle} + \frac{1}{\langle m \rangle}$$

that in the case of coherent states simplifies to:

$$g^{(2)}(m) = 1 + \frac{1}{\langle m \rangle}$$

Similarly, also the cross-correlation function can be obtained. This gives the correlation between the two outputs of the detection PBS [13]

$$g^{(1,1)}(m) = 1 + \frac{\langle m_1 m_2 \rangle}{\langle m_1 \rangle \langle m_2 \rangle}$$

For Poissonian statistics, it reduces to $g^{(1,1)}(m) = 1$. First of all we studied the second-order auto-correlation function for both the output channels as a function of the WLC input pump power. All the measurements had about the same mean number, around a mean number of 5 photons. The results are reported in Figure 4.10. On the x axis we have the measured input power (in μJ) related to each acquisition. Blue and red dots correspond to the two different SiPMs. The expected auto-correlation value is represented by the dashed lines.

[12] 12: [58] Roy J Glauber, *Physical Review*, p. 2529 (130), (1963)

[13] 13: [59] Alessia Allevi, Stefano Olivares, and Maria Bondani, *Physical Review A—Atomic, Molecular, and Optical Physics*, p. 063835 (85), (2012)

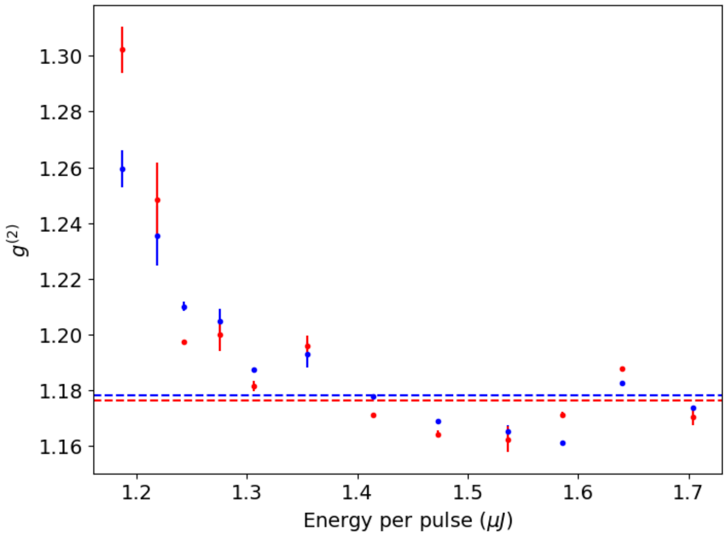

Figure 4.10: Second order auto-correlation function for ch1 and ch2 as a function of the WLC input power.

We can observe that as the pump power increases, the auto-correlation values get closer to the expected one. The data reported here are obtained by averaging the results of four different measurements for each pump intensity, in order to repeat the experiment and obtain a suitable error bar. We can observe that for pump values greater than 1.6 μJ the experimental data are the closest to the expected value.
This plot is meant to show the overall behavior at variance of the input power. The small discrepancies might be a consequence of the fact that the expected correlation value is calculated for an average mean value of the optical states, that is not exactly the same for each value of energy per pulse.
From the same dataset, we performed the study of the cross-correlation. The results are reported in Figure 4.11, where again the x axis represents the pump power in μJ. The blue dots are the correlation values calculated from the data, while the dashed black line represents the expected value, that for coherent states is equal to 1. Also in this case data are obtained by averaging four datasets and the overall behavior is the reduction of correlations as the pump increases. Similarly to the auto-correlation results, the values obtained for pump values greater than 1.6 μJ are in agreement with the expectations.

Let's notice that for low intensities the error bars result to be larger. This is a consequence of the large fluctuations displayed by the generated states.
A further analysis performed involves the reconstructed

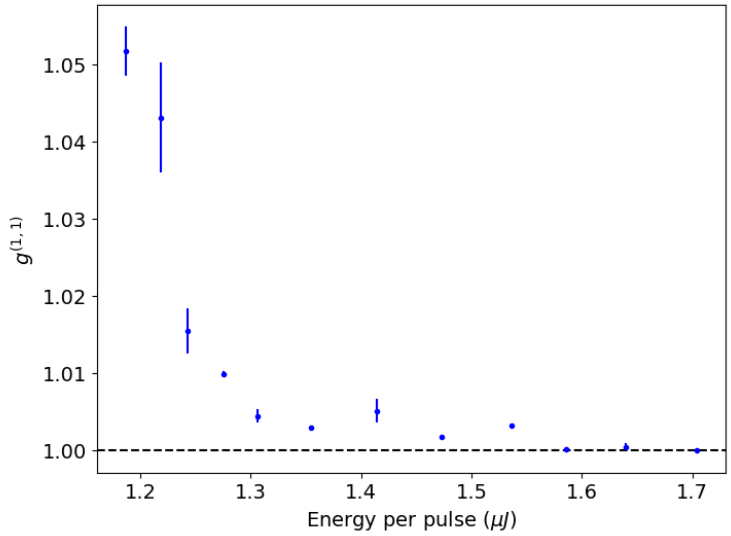

Figure 4.11: Second-order cross-correlation function as a function of the WLC input power.

statistics. Here we compare the distributions obtained for the two extreme sampled power values. Figure 4.12 refers to the first point of the previous two plots, corresponding to ~ 1.2 μJ while Figure 4.13 refers to the most intense power measured ~ 1.7 μJ. In the two figures the experimental distributions obtained by the measurements are represented as dots, while the theoretical expectations are represented by the blue line.

It is easy to observe that the agreement between the data and theory is better at higher power. To measure the agreement between data and expectation we use the fidelity, already presented in Chapter 2. We recall that the closer the fidelity value to 1 the better the agreement, as well as the fact that a good agreement should have $f > 0.999$.

The value of fidelity calculated for Figure 4.12 is $f = 0.99689$, which does not satisfy the goodness benchmark. On the other hand, the value obtained from Figure 4.13 is $f = 0.99994$, which is considered to represent a good agreement between data and theory.

Fidelity

$$f = \sum_n \sqrt{P_{exp}(n) P_{th}(n)}$$

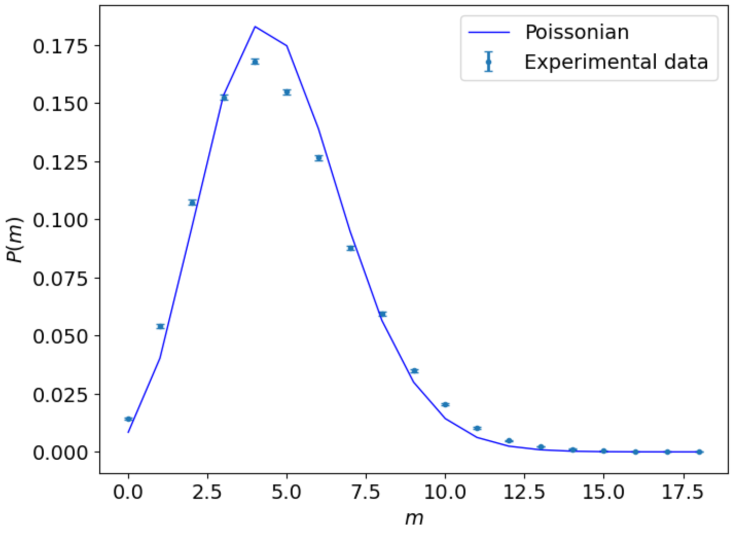

Figure 4.12: Reconstructed photon-number distribution for pump power ~ 1.2μJ. Dots represent the experimental data, line represents the theoretical expectation, $f = 0.99689$.

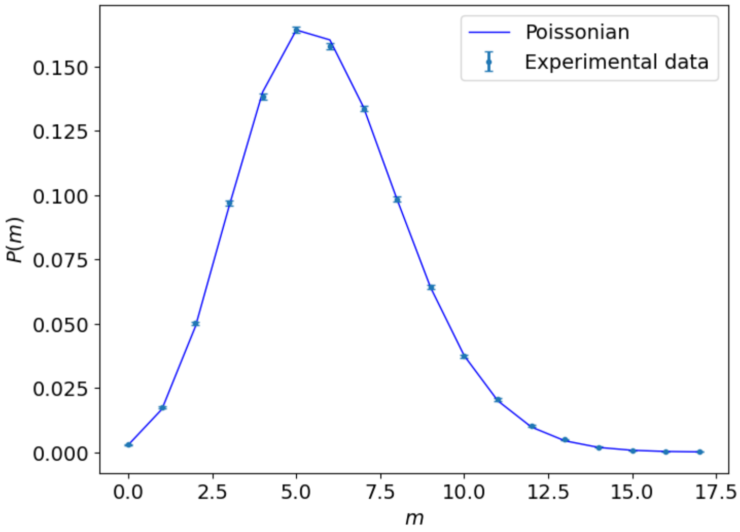

Figure 4.13: Reconstructed photon-number distribution for pump power ~ 1.7μJ. Dots represent the experimental data, line represents the theoretical expectation, $f = 0.99994$.

According to this analysis we can state that, even if the threshold power to generate WLC is provided, this is not necessarily stable. In fact, while trying to characterize coherent states with our up-conversion detector, we were able to observe the instability regime of the WLC generation. To the best of our knowledge this was the first characterization of WLC behavior in terms of photon-number statistics.

To ensure to have achieved the requirement of generating coherent states, we set the WLC pump power to ~ 1.7μJ and acquired some measurements as a function of the intensity. This variation is performed by introducing a variable neutral density filter on the SFG beam. The aim of this experiment is to compare the results with the ones obtained by acquiring the built-in second harmonic (515 nm) of the laser. The latter has been split at a balanced BS and acquired using the same SiPM detectors as a function of the intensity (using neutral density filters as well). In this case, the analysis is performed as a function of the mean value and we compare the auto-correlation behavior of the two sources with the expected coherent behavior. The results are compared in Figure 4.14, where we can observe that the up-converted data are in agreement with the built-in SHG and the theoretical expectation. Similarly to the previous analysis, the reported data are the average of four different datasets acquired in the same conditions.

Also in this context we calculated the cross-correlation for the up-converted data, the results are reported in Figure 4.15. We can observe that the cross-correlation data statistically fluctuate around one, which is the theoretically expected value for coherent states.

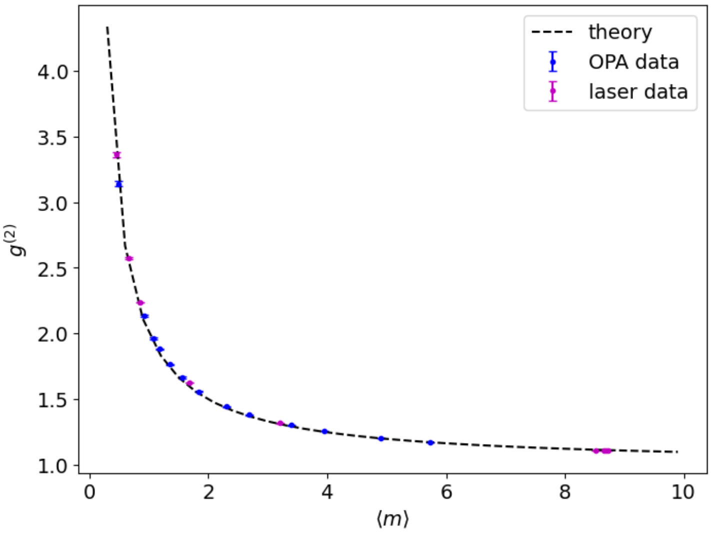

Figure 4.14: $g^{(2)}$ comparison between laser (magenta dots) and OPA (blue dots) beams. Dashed line represents the expectation according to theory.

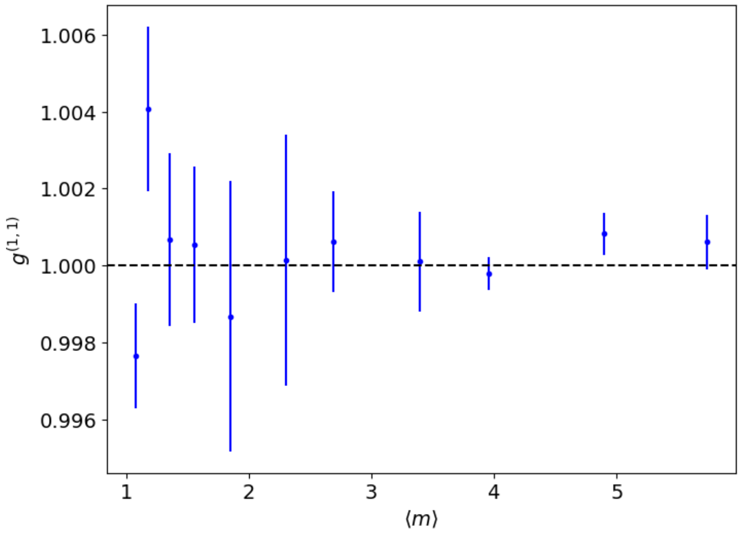

Figure 4.15: $g^{(1,1)}$ calculated for OPA data (blue dots) compared to theoretical expectation (black dashed line).

Finally, we conclude with the statistical reconstruction of the photon-number distribution in this regime. One distribution has already been reported in Figure 4.13, with a mean value of about 5.5 photons. Here, in Figure 4.16 and Figure 4.17, we report two other photon-number distributions reconstructed according to the same method, and their fidelity, which is $f = 0.99993$ for both of them.

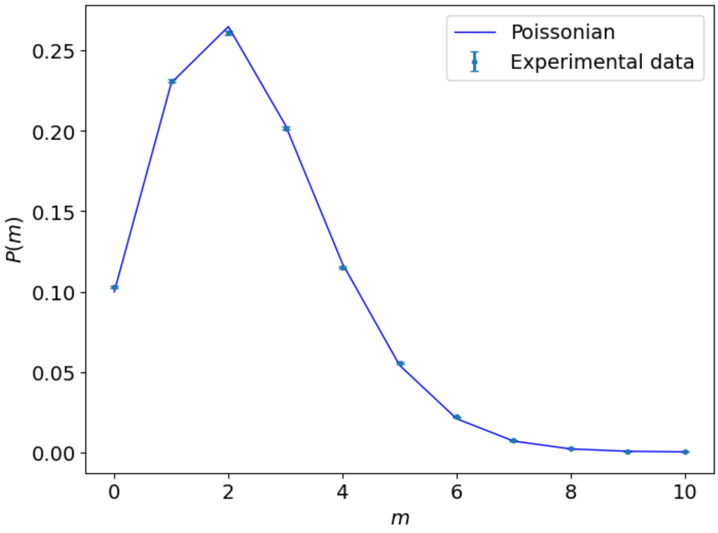

Figure 4.16: Reconstructed photon-number distribution for $\langle m \rangle = 2.30$. Dots represent the experimental data, line represents the theoretical expectation, $f = 0.99993$.

To summarize, in this section we put our attention on the first part of the experiment, where we tried to build a suitable coherent source. Under the condition of setting a sufficiently high pump power for the WLC, the setup seems to generate and be able to detect coherent states of light. In the following

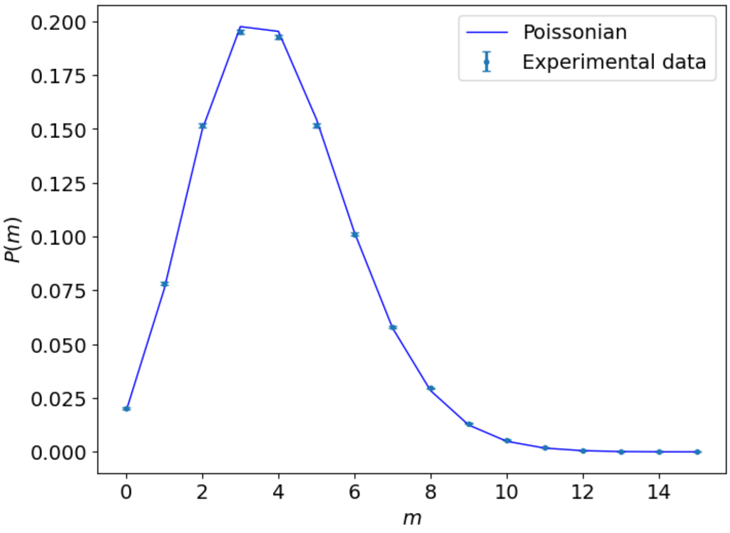

[h] **Figure 4.17:** Reconstructed photon-number distribution for $\langle m \rangle = 3.95$. Dots represent the experimental data, line represents the theoretical expectation, $f = 0.99993$.

section we will move the focus on the manipulation of the 1550 nm beam intensity and its detection.

4.4 Light manipulation

The manipulation [14] of the beam at 1550 nm and its correct reconstruction is a crucial point to verify the suitability of such an up-conversion detector in the context of communication. As already explained in the section related to the experimental setup, we realized a quasi-collinear SFG in order not to manipulate the up-conversion pump as well. First of all, we decided to perform a simple manipulation in intensity that displays a well-known behavior, such as Malus law. It means the variation of intensity as a consequence of the modification of the polarization of an optical field before its passage through a polarizer. In our case, the polarization of the beam at 1550 nm was set to be vertical. Hence, by placing a polarizer, it was possible to reduce, and eventually extinguish, the vertical component according to Malus law. Since the SFG phenomenon is generated only by the vertical component, by reducing it also the 620 nm beam should decrease in intensity, following as well Malus law. In other words, by introducing a polarizer on the C band beam we could apply a controlled modification of the generated SFG. The first step required was the characterization of the actual manipulation of the beam at 1550 nm. To this aim we used the Hamamatsu spectrometer placed beyond the BBO crystal.

[14] [60] Frédéric Grosshans et al., *Nature*, pp. 238–241 (421), (2003)

We remind the reader that Malus law obeys the following relation

$$I(\alpha) = I_0 \cos^2(\alpha)$$

The intensity values were acquired by changing the polarization angle in steps of 10 degrees. The obtained results are reported in Figure 4.18. The data shown in the figure, represented by the green dots + error bar points, are the average of three datasets. The data are subtracted of the experimental offset, and normalized to the initial intensity, so that their values are between 0 and 1, as expected for a $\cos^2(x)$ function. The data are then fitted with the theoretical model, using a function $f(x) = \cos^2(ax + b)$. Since Python sinusoidal functions are defined in radians, we converted the acquired angle from DEG into RAD. The obtained fitting parameters are $a = 1.001$ and $b = 0.1$. In this case the amplitude was set to 1 because the data were normalized to the initial intensity.

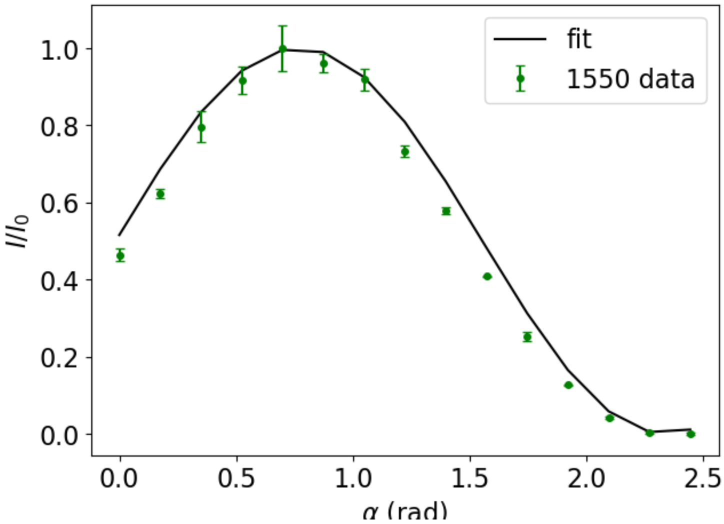

Figure 4.18: Malus law for the 1550 nm beam. Green dots represent the data, black line the fit model.

After having correctly reconstructed the behavior of the manipulated beam, we focus on the reconstruction of the up-converted beam modification. The results are reported in Figure 4.19, where the blue dots represent the experimental data averaged over four datasets. Also in this case the angles on the x axis are expressed in radians. Our first attempt was to fit the data with a $\cos^2(x)$ function, describing Malus law. The best fit obtained is shown as green line in Figure 4.19. Apart from a phase parameter that results to be very large ($b = 2.7$ rad), we can observe from the plot that the line overlaps the data only for the ascending part of the maximum, but then the curve results to be too large compared to the experimental outcomes.

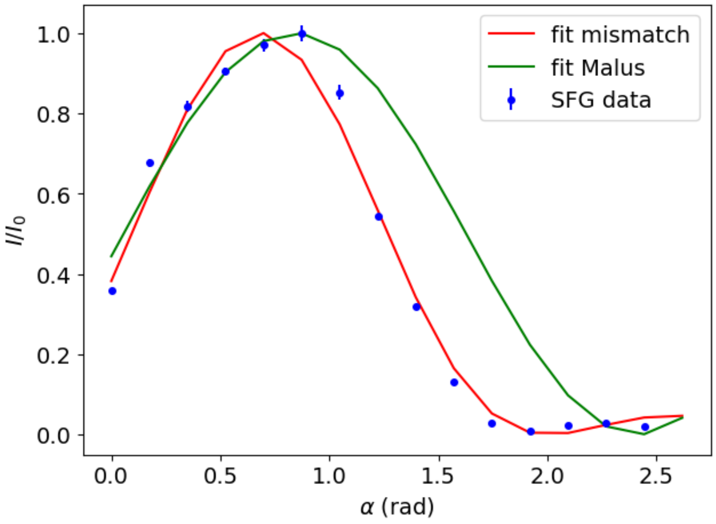

Figure 4.19: Malus law for the 620 nm beam. Blue dots represent the data, green line Malus law fit model and red line phase mismatch fit model.

Moreover, if we focus on the minimum, we can observe a very small increase in the data, similar to a local maximum. These two peculiarities suggest that another phenomenon overlaps on our manipulation, the phase mismatch [15], which is described by the function $f(x) = \left(\sin(x)/x\right)^2$. Thus, we tried to fit the data according to this theoretical model (red curve), and we can observe that the agreement is better for the data that do not obey Malus law. In fact, the mentioned function is narrower than the $\cos^2(x)$. Nevertheless, we needed to investigate what could introduce the phase mismatch in our setup. The answer came from the infrared polarizer extinction ratio, that is 10:1. This means that there is always some residual vertical polarization that interacts with the pump, even when the generation is supposed to be none. This explanation is in agreement with the obtained data, since we can observe that where the polarization attenuation is minimal, the contribution of the residual vertical component is negligible and the data follow Malus law. As the vertical residual becomes a more relevant part of the transmitted light, that is supposed to decrease in intensity up to zero, the phase-mismatch behavior begins to appear.
Hence, in this case we cannot state the perfect reconstruction of the manipulated beam because of the poor quality of the manipulation item itself. We assume that if a suitable polarizer were available in the laboratory, both the 1550 nm and 620 nm curves would be in agreement with Malus law.

[15] [28] Robert W. Boyd, *Academic Press*, (), (2008)

As a final part of this experiment we wanted to perform a further manipulation. The initial idea was to generate a thermal state on the 1550 nm beam that would have been then up-converted. This would have given the chance to observe and characterize a photon-number statistics different from the Poissonian one. Unfortunately, due to the lack of a scattering material suitable for this wavelength and the understanding that, probably, the intensity of the beam at 1550 nm could not be enough to generate a far-field speckle field intense enough to generate SFG, we gave up this plan. Nevertheless, keeping the idea of detecting a different photon-number distribution, we decided to perform another kind of modulation. We considered the case in which a set of amplitude-modulated coherent states are used to encode a message [16] [17]. In the case the acquisition chain is active during the modulation, a part of the dataset will belong to a distribution of mean value $\langle m_1 \rangle$ and another part to a distribution of mean value $\langle m_2 \rangle$. So the modulated distribution description is the weighted sum of the two Poissonian distributions:

$$p_{mod} = \sum_{i=1}^{2} p_i \frac{\langle m_i \rangle^m}{m!} e^{-\langle m_i \rangle}$$

where p_i are the weights of the first and second datasets, respectively. More in general, if we consider a number N of amplitude modulations to be performed in the acquisition window, we have the distribution

$$p_{mod} = \sum_{i=1}^{N} p_i \frac{\langle m_i \rangle^m}{m!} e^{-\langle m_i \rangle}$$

The first two moments of this distribution are

$$\langle m_{mod} \rangle = \sum_{m=0}^{\infty} m p_{mod}(m)$$

and

$$\langle m_{mod}^2 \rangle = \sum_{m=0}^{\infty} m^2 p_{mod}(m)$$

from which it is possible to obtain the variance $\sigma_{mod}^2 = \langle m_{mod}^2 \rangle - \langle m_{mod} \rangle^2$ and the Fano factor $F_{mod} = \sigma_{mod}^2 / \langle m_{mod} \rangle$. These quantities can be used to define the correlation coefficient, representing the measurable correlation at the two

[16] [61] Anthony Leverrier and Philippe Grangier, *Physical Review Letters*, p. 180504 (102), (2009)

[17] [62] Shouvik Ghorai et al., *Physical Review X*, p. 021059 (9), (2019)

outputs of the PBS in front of the SiPMs.

$$\Gamma = \frac{F_{mod} - 1}{F_{mod} + 1}$$

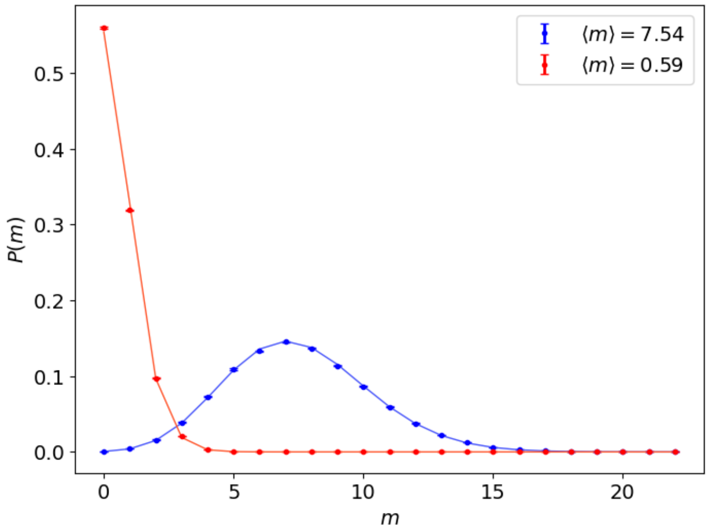

Figure 4.20: Reconstruction of the two photon-number distributions having $\langle m_1 \rangle = 15.08$ and $\langle m_2 \rangle = 1.18$, respectively.

First of all, we start from the simplest case in which the modulation, as explained above, is performed considering two different mean values. The chosen coherent state distributions are reported in Figure 4.20. The most intense one has mean value $\langle m_1 \rangle = 15.08$ while the weakest one has mean value $\langle m_2 \rangle = 1.18$ photons.

Let's suppose that our acquisition slot has a fixed number of measurements, while p_1 and p_2 are the weights according to which the two states are acquired. Dividing these numbers by n, we can describe the system in terms of probability.

Here we want to perform a series of measurements as a function of p_1 and $p_2 = 1 - p_1$. In this case the correlation coefficient reads

$$\Gamma = \frac{p_1 p_2 (\langle m_1 \rangle - \langle m_2 \rangle)^2}{p_1 p_2 (\langle m_1 \rangle - \langle m_2 \rangle)^2 + 2(p_1 \langle m_1 \rangle + p_2 \langle m_2 \rangle)}$$

where the state labeled as 1 is always the most intense and the state labeled 2 is the weakest. We remark that the mean values reported in this formula correspond to the ones of the original states, before the division at the PBS.

We decided to perform a first analysis as a function of the state probabilities. Since the current setup does not allow us to perform such a precise modulation during the acquisition, the two states have been acquired separately and merged in post processing.

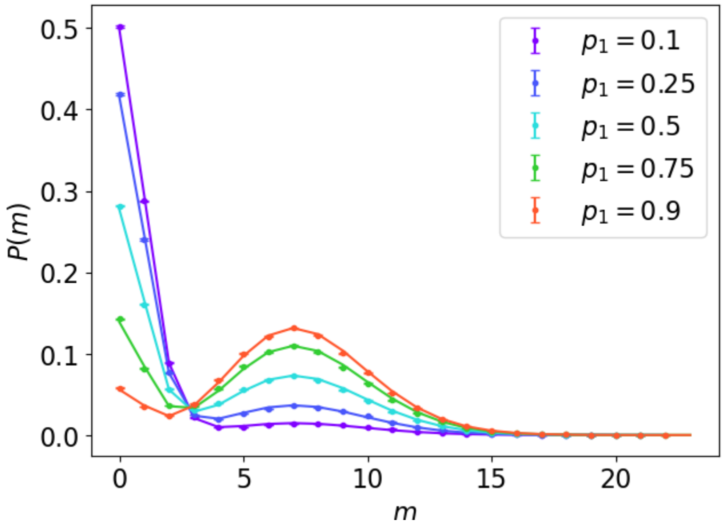

Figure 4.21: Statistical reconstruction of the modulated distributions at different values of p_1. Colored dots represent experimental data, solid lines represent the theoretical expectations.

The acquired statistical distributions are reported in Figure 4.21, as well as their theoretical curves, calculated as a weighted sum of two Poissonian distributions having the measured mean values. All the fidelities are above 0.9999. The experimental data have been produced by averaging four datasets. Of course, we calculated correlations as well and compared the obtained results with the theoretical expectations. Also in this case the data are the average of four datasets. The agreement between data and theory can be appreciated from Figure 4.22.

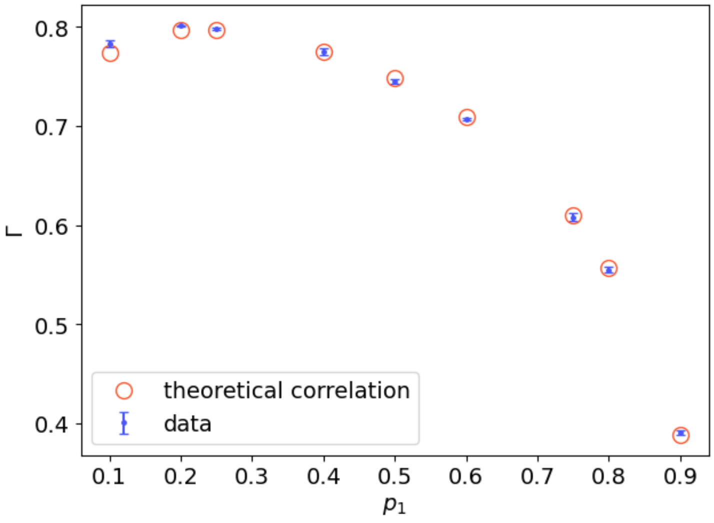

Figure 4.22: Correlation coefficient of the modulated distribution at different values of p_1. Full dots represent experimental data, open circles represent the theoretical expectation.

The last analysis we decided to perform is even fancier, considering a set of different possible intensity modulations. In fact, in this case we want to reconstruct the statistics of a different number of modulations in the finite acquisition window. Given n the number of modulations involved in a single dataset, all the states have the same probability $p = \frac{1}{n}$. Exactly like in the previous case, the coherent states were acquired separately and the merging was performed in post processing. In Figure 4.23 four different statistical distributions corresponding to the sum of 2, 4, 6 and 8 equally probable coherent states are shown, respectively. The two statistical distributions (blue dots) are the same used in the previous analysis having $p = 0.5$. In the case of the four-state modulation (light blue dots), we added to those states two other states having $\langle m_3 \rangle = 11.12$ and $\langle m_4 \rangle = 5.28$. In this case all the states have probability $p = 0.25$. To generate the six-state modulation (green dots), we introduced two further coherent states having $\langle m_5 \rangle = 13.3$ and $\langle m_6 \rangle = 2.38$. For the six-state modulation all the coherent states involved have probability $p \sim 0.167$. Eventually, we performed the eight-state modulation (orange dots), in which to the previous six states we added two further coherent states with $\langle m_7 \rangle = 7.58$ and $\langle m_8 \rangle = 5.52$. The probability of each state in this case is $p = 0.125$. Also in this last case the experimental data are the average of four different datasets.

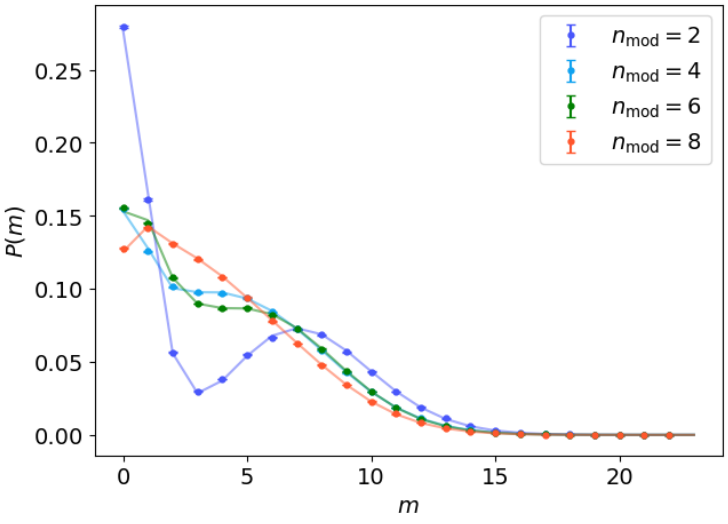

Figure 4.23: Statistical reconstruction of the modulated distribution as a function of the number of coherent states involved. Colored dots represent experimental data, solid lines represent the theoretical expectations.

The reconstruction of the statistical distributions is in good agreement with the data since all the fidelities are above

0.9999. We can observe that, by increasing the number of modulations, the distribution shape becomes flatter.

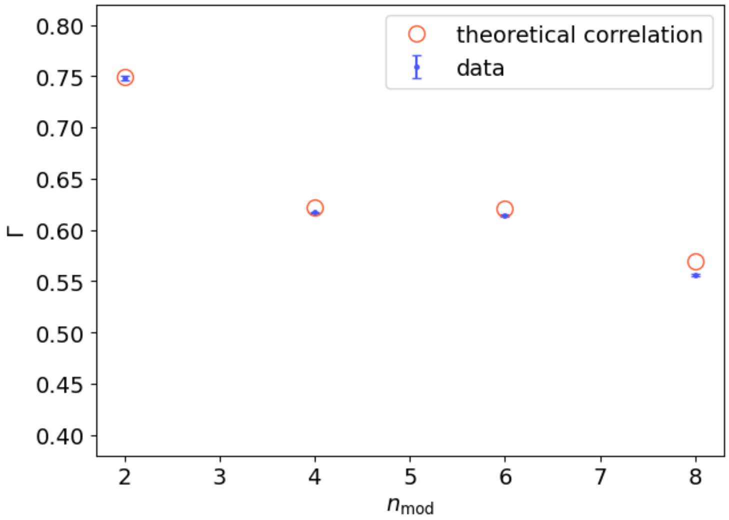

Figure 4.24: Correlation coefficient of the modulated distribution as a function of the number of coherent states involved. Full dots represent experimental data, open circles represent the theoretical expectations.

The calculated correlation coefficient is shown in Figure 4.24, where again the data (full dots) are obtained by averaging four datasets. In the plot they are compared to the theoretical expectation, represented as open circles. The lack of agreement between the experimental results and the expectation, as the number of modulations increases, is a consequence of the nonlinear spacing between the mean values of the coherent states. Anyway it is significant only in the case of 8 modulations.

4.5 Conclusions

In this chapter we developed an experimental setup in order to investigate the suitability of SiPMs for telecom wavelength communication. We created an up-conversion detector, that exploits nonlinear sum-frequency generation to convert the C band coherent states into a wavelength detectable with SiPMs. We verified that such a process not only does not introduce any modification to the encoded beam, but also enables us to reconstruct any manipulation it undergoes. We admit that this work has a lot of space for improvement, starting with the overall efficiency that is quite low at the moment (about 2%), as well as the improvement of some experimental equipment that does not perform at its best at this wavelength. Also, the bulk optics setup is not compliant with the telecom standards, which involve fiber optics propagation. Nevertheless, the proof-of-principle results obtained are encouraging to consider this work as a possible solution to implement in a hybrid detector to be operative at telecom wavelengths.

EXTRA CHAPTER

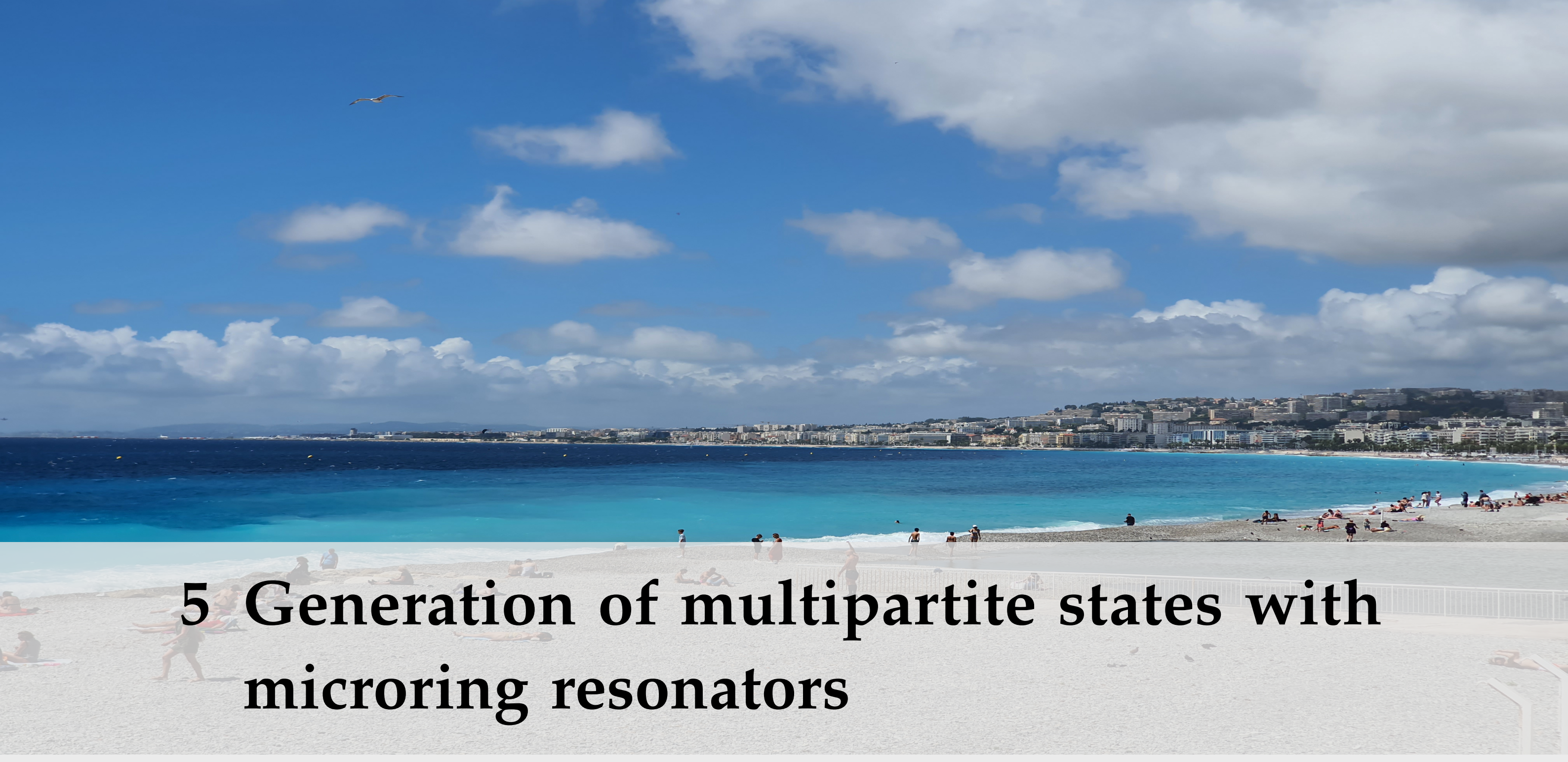

5 Generation of multipartite states with microring resonators

5.1 Disclaimer

According to the requirements of my PNRR scholarship, I spent a period of six months in Nice, at the Université de la Côte d'Azur. More precisely, at the Institut de Physique de Nice (InPhyNi), in the group of Photonics and Quantum Information (PIQ), under the supervision of prof. Virginia D'Auria.

During these months, I had the chance to work on a project that is considerably different from the one reported in the previous chapters, but potentially useful in the field of quantum technologies. The core of the project was the generation and characterization of multipartite states produced using a microring resonator (MRR). I am very grateful for the opportunity I have been given, because I had the chance to experience optical phenomena that were not accessible in the laboratory in Como, such as the generation of frequency combs at telecom wavelengths (1550 nm) and the performance of a χ^3 non-linear process such as four-wave mixing. Moreover, as shown in the following, the propagation of the pump laser was in optical fiber until the alignment to the Silicon Nitride (Si_3N_4) integrated chip. This was as well a strong difference with respect to the experimental setups previously described.

---

[0] Background photo: Nice beach seen from the Promenade des Anglais.

5.2 Introduction

Integrated optics has become more and more promising over the years, in particular due to its low energy cost, high efficiency and scalability. These main features have made integrated devices a breakthrough technology in different fields of optics, among which the most remarkable are: nonlinear optics, generation of quantum states, communication, metrology and quantum key distribution. For example, the results of nonlinear interactions are enhanced, due to the already mentioned high efficiency and the reduction of losses. Moreover, in the last decades, the performance of waveguide optics has been improved by the engineering of the configuration and the investigation of the behavior of different materials. In fact, while in the past Lithium Niobate was the most exploited material in this field, now the choice has become much wider, allowing to select the most suitable waveguide according to the specific application.[1]

In particular, the material chosen to perform the experiment reported in this chapter is Silicon Nitride (Si_3N_4) because of its high nonlinear refractive index at telecom wavelengths ($n_2 = 2.5 \times 10^{-5}$ cm^2/W) and the reduced propagation losses (< 0.5 dB/cm). [2] In the context of this experiment, we have obtained the generation of multipartite states of light by exploiting a micro-ring resonator. The input of a Si_3N_4 waveguide was coupled with a high power CV telecom laser, aiming to exploit the ring resonance in order to generate a four-wave mixing (FWM) phenomenon. In this particular nonlinear process, two photons from the pump generate signal and idler photons. The peculiarity of choosing this type of device is that it enables to have the two pumps at the same wavelength. In fact, the FWM is generated inside the waveguide (as a consequence of the nonlinearity of Si_3N_4) from the input pump and the portion of light coupled with the ring. Since it is well-known that micro-ring resonators have a behavior similar to that of optical cavities, the result of this configuration is the generation of a frequency comb symmetrical with respect to the pump frequency. All these phenomena will be better explained in the next section, where an overall theoretical introduction is given.

[1] 1: [63] Laurent Labonté et al., *PRX Quantum*, p. 010101 (5), (2024)

[2] 2: [64] Avik Dutt et al., *Physical Review Applied*, p. 044005 (3), (2015)

5.3 Theoretical Outlines

In this section the theoretical descriptions of the involved experimental phenomena are presented.

Let's begin with the description of the nonlinear phenomena exploited in this work. The first one is the already mentioned Four Wave Mixing (FWM), that is generated by the propagation of a suitably intense and polarized pump beam in the waveguide. This is a parametric, $\chi^{(3)}$ process, which obeys energy conservation and requires a phase-matching condition to be generated.
If we consider two fields, respectively oscillating at frequencies ν_1 and ν_2, in the third-order nonlinear medium, a refractive index modulation can occur at the difference frequencies, $\nu_3 = 2\nu_1 - \nu_2$ and $\nu_4 = 2\nu_2 - \nu_1$. A schematic representation of the process is reported in Figure 5.1. In the case in which two of the involved fields have the same frequency, the phenomenon is said to be degenerate. This is the specific case of the experimental implementation in this work, since the two pumps have the same wavelength.
It is worth noting here that the implemented setup is provided with just a single laser beam at the fundamental wavelength, performing as a first pump. The second pump is provided by the integrated optical circuit chosen to perform FWM. In fact, in our experiment, FWM is generated in a Si_3N_4 waveguide. The mentioned waveguide is coupled with another closed-loop one forming a micro-ring resonator (MRR). Due to the evanescent field, a part of the light in the bus waveguide can be coupled in the closed-loop one and then again in the bus waveguide.

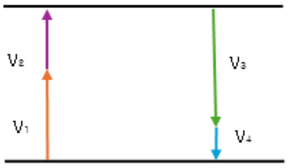

Figure 5.1: Four-wave mixing scheme.

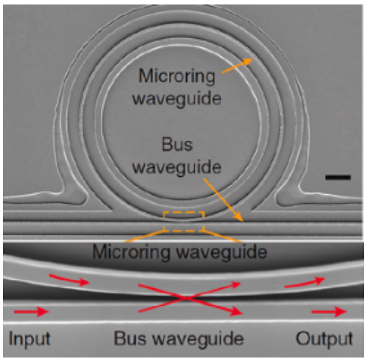

Figure 5.2: Microring resonator. Image from the article: Li et al., Nanophotonics 10, no. 11 (2021): 2799-2832

Figure 5.2 gives an idea of the way in which the light delayed by the ring recouples with the input light in the bus waveguide, behaving as a second pump. Moreover, the closed loop behaves like an optical cavity. In fact, for some wavelengths, the recoupled light is in phase with the input light so that they can sum in constructive interference. More precisely, the resonance condition is $L = m\lambda$, where m is an integer number and L is the optical path. In the ring case $L = 2\pi R n_{eff}$ with n_{eff} being the effective refractive index of the waveguide.

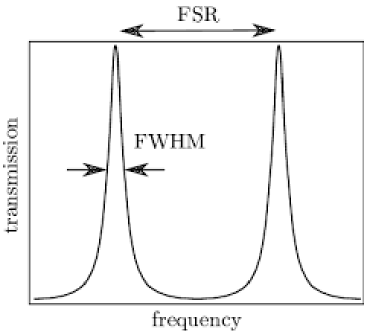

Figure 5.3: Schematic representation of resonant modes.

Similarly to any regular optical cavity, the resonant modes correspond to specific frequencies, and according to the ring features, each resonant frequency will be characterized by a certain width, $\delta\nu$, and they will be separated by a frequency range called Free Spectral Range, ν_{FSR}. This means that also for MRR it is possible to define the quality factor Q

$$Q = \frac{\nu}{\delta\nu}$$

and the finesse $\mathcal{F}$

$$\mathcal{F} = \frac{\nu_{FSR}}{\delta\nu}$$

In the section related to the description of the setup the details of the ring chosen to perform the experiment are presented.

Thus, the basic idea behind this device is the generation of a FWM comb in the nonlinear waveguide and the selection of some comb modes, under the resonance condition. Of course, as a consequence of the resonance condition, these modes will be characterized by a phase relation. The Hamiltonian of the process under the condition that each mode can behave as a pump reads as sidenote E. Gouzien et al., Phys. Rev. Res. 5, 023178, 2023

$$\hat{H} = \sum_{k,l,m,n} \delta_{k+l,m+n} \hat{a}_k^\dagger \hat{a}_l^\dagger \hat{a}_m \hat{a}_n$$

The presence of two creation and annihilation operators represents the two photons destroyed on one or two modes, and the generation of two photons on other two modes.

The theoretical model used to describe the quantum correlation between the generated modes is an original work of the group that hosted me in Nice, but since I did not take part in this research in person I will just limit to share an outline of the procedure and their results.

Starting from the Hamiltonian operator, we apply the evolution of the bosonic operators in the Heisenberg representation, choosing the pump rotating frame and linearizing the bosonic operators. The final aim is to write the Langevin equations for the covariance matrix and the field quadratures. It is, thus, possible to study the quantum behavior of the system in terms of logarithmic negativity, [3] which is defined as

$$\Sigma = -\sum_{i|n_i<1} \ln n_i$$

where n_i are the symplectic eigenvalues of the partially transposed covariance matrix, written in terms of a partition operator. According to this criterion of non-classicality, if

[3] [65] Adrien Bensemhoun et al., *Physics Letters A*, p. 129272 (493), (2024)

$\Sigma > 0$ the state is non-separable. In this work, some simulations of the system have been performed, taking into account intrusive phenomena such as dispersion, losses, decoupling and nonlinear effects. The study has been performed as a function of the pump power, in the above-threshold regime. Here we report the main results obtained.

In Figure 5.4 the simulated comb for each chosen pump power is shown. We notice that the latter is expressed in threshold power units. From the plots, we can observe that, increasing the pump power, not only does the number of generated modes increase but their intensity as well. In particular, it can be noticed in the case of the first couple of generated modes, ±1.

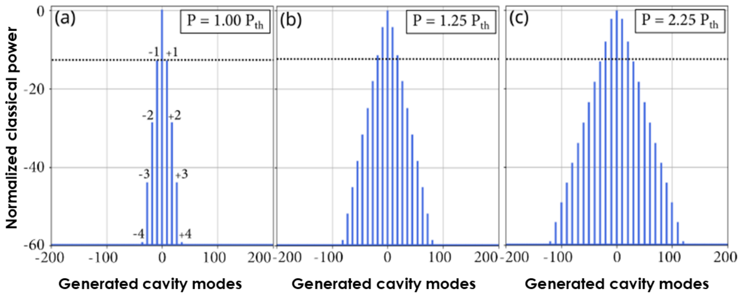

Figure 5.4: Simulated frequency combs according to the pump power, in units of threshold power

Moreover, the logarithmic negativity, which represents the quantum correlations between the modes, has been represented in a graphic and intuitive way, considering the correlations between five modes: the pump and the couples ±1 and ±2.

As reported in Figure 5.5, the logarithmic negativity is represented as a link between the modes, where the thickness of the link represents the value of the correlation. Thus the thicker, the more correlated the states.

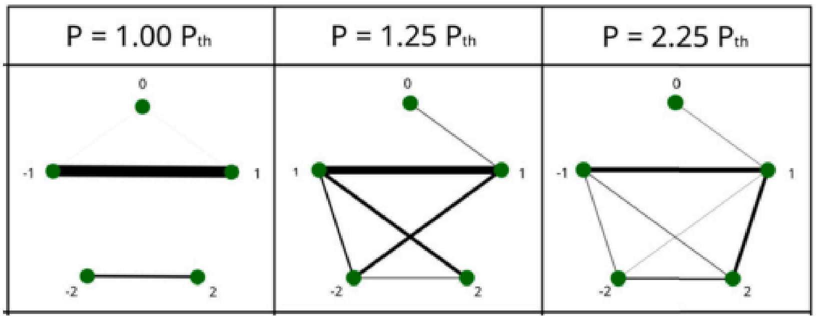

Figure 5.5: Logarithmic negativity represented as link between the generated modes.

Figure 5.5 shows two different regimes. The first one is what we call bipartite regime, and is exhibited at the cavity threshold power. In fact, in this case we can observe that the mode +1 is only correlated with the specular mode −1, and the same holds for ±2. Conversely, increasing the pump power, the system begins to present cross correlations, thus introducing the so-called multipartite regime. As the pump intensity increases, the distribution of correlation changes, as can be observed in the middle and right box of Figure 5.5.
The physical explanation of this behavior is related to the intensity of the generated comb modes. In fact, if the modes become intense enough, they can behave themselves as pumps to the system. In Figure 5.6 are reported some examples of generation scenarios: in the first one the pump generates photons in the other modes, in the second one a generated mode is intense enough to be considered as a further pump that generates photons in the adjacent modes, in the third one there are two different pumps at different wavelengths, being one the input pump and the other a generated mode [4] [5].

We note that in Figure 5.6 it was considered only the contribution of mode −1 to the generation of other modes, just to give the idea. Actually, as already mentioned, according to the theory reported, any of the generated modes could behave as a pump.

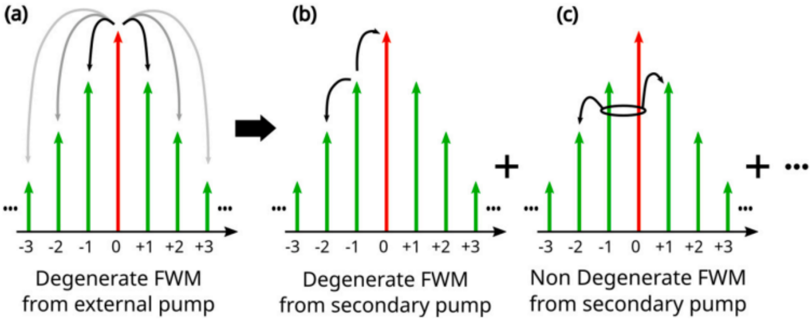

Figure 5.6: Examples of generation scenarios.

5.4 Data Acquisition and Experimental Setup

When I joined the project, the main issue was to acquire simultaneously all the four generated modes (±1, ±2), in order to calculate correlations and cross-correlations. Actually,

[4] [66] Maxim Karpov et al., *Nature Physics*, pp. 1071–1077 (15), (2019)

[5] [67] Yanne K Chembo, Elham Heidari, and Curtis R Menyuk, *Applied Physics Letters*, (123), (2023)

at the time the experimental setup only allowed the direct measurement of correlations between two channels.
In this section the experimental setup and the acquisition chain are described. The main characteristics and improvements implemented to obtain the results shown in the following paragraphs are explained. Moreover, in these pages the reader will find some information about the experimental procedure as well, with the aim to make the final results as clear as possible.

5.4.1 Micro-Ring Resonator

I did not take part in the characterization and choice of the most suitable MRR used in the experiment. Nevertheless, I report here the main characteristics of the employed chip. Specifically, the device chosen for this experiment is a custom chip realized by CEA-LETI in Grenoble.

The substrate material, as already mentioned, is Si_3N_4. For fabrication reasons, the height of the waveguide is set at 800 nm. The radius of the ring is 112 μm, in order to have a free spectral range of 200 GHz, compliant with the standard for telecom applications. The waveguide section dimensions are, respectively, 1.9 μm for width and 800 nm for height. The gap between the ring and the bus waveguide is 300 nm. These parameters have been deeply investigated in order to have the best performance for this experiment. In fact, the width of the optical fiber allows improving the quality factor (on the order of 10^6) since it has lower losses. At the same time, the distance between the guide and the ring has been proven to have a good coupling efficiency in the regime of interest although it requires a higher input power. For this device, the measured threshold power is P_{th} = 50 mW. It is worth mentioning that these devices are used to generate multipartite states in frequency, since the waveguide forces the generation in the same spatial mode.

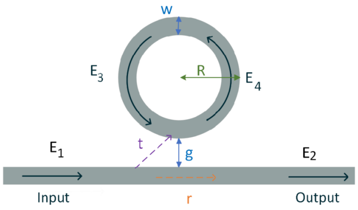

Figure 5.7: Scheme of a MRR.

5.4.2 Description of the Experimental Setup

Let us start with a general description of the first part of the experimental setup, before having a deeper view of the acquisition chain.

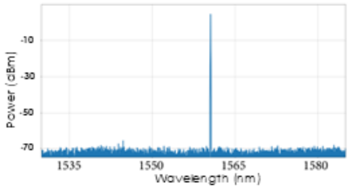

Figure 5.8: Laser spectrum obtained with the optical spectrum analyzer.

The light source chosen for this experiment is the RIO-ORION 1550 nm laser module, a continuous wave laser chosen for its tunability (around 40 pm) and for the low noise level. In fact this kind of measurement requires a shot-noise-limited laser. The output power of this source is on the order of tens of mW.

The power required at the chip input in order to generate the phenomenon of interest in the CW regime is considerably high, around 300–500 mW. This requires the amplification of the laser source, in particular we exploited an Erbium Doped Fiber Amplifier (EDFA) from KEOPSYS, typically set at 26.5 dBm. Since this device has an input limit of 1 dB, a variable attenuator is inserted between the laser source and the amplifier.

Let us point out that all the optical devices before the resonance chip are connected to each other through a Thorlabs single-mode optical fiber at telecom wavelengths. The output of the amplifier is connected to a polarization controller, in turn connected to a polarizing beam splitter. This allows introducing an intensity control on the chip input power. The second arm of the polarizing beam splitter is connected to a 99:1 beam splitter, whose less intense output is linked to a power meter, which is exploited as an input power monitor. This method allows, with suitable calculations, to estimate the chip input power in terms of threshold power. Of course,

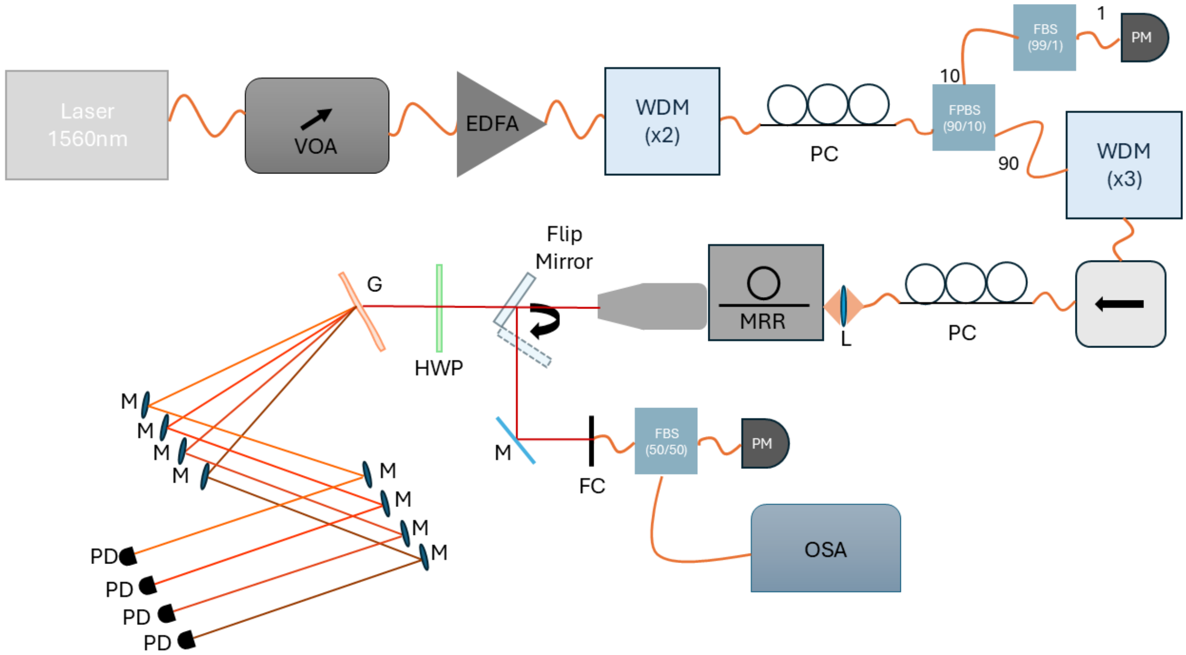

Figure 5.9: Sketch of the experimental setup

to implement this procedure, it is necessary to characterize every item in the setup in terms of losses.

In order to reduce the noise generated from the amplifier and the fiber propagation, some wavelength division multiplexer (WDM) filters are inserted in several parts of the setup, as well as an isolator whose aim is to reduce the light reflection along the optical path.

Since the microchip coupling is sensitive to the input light polarization, the coupling lens (1 μm focal length) is preceded by a polarization control. In particular, TM polarization has lower coupling losses but higher propagation losses, while for TE polarization it is the opposite. Due to the fact that correlation is a very delicate measurement and it is strongly affected by losses, we chose to reduce the losses in propagation at the cost of a higher but fixed coupling loss.

The chip is mounted on a thermoelectric cooler (TEC) that enables improving the emission stability by fixing the temperature. In our case it is set at 68.5 °C.

To place the microchip in the setup, a piezoelectric mount is used, so that it is easy to perform a fine alignment every time it is necessary.

The light propagation after the microring is in free space, the output is coupled with a microscope objective to collimate the beam and then separated by a high-efficiency diffracting grating and propagated to the detection apparatus. Before the grating, a half-wave plate is inserted with the aim to rotate the polarization in order to maximize the measured correlations.

After the microscope objective, a flip mirror is placed in order to send the light to the Optical Spectrum Analyzer (OSA) and a second power meter. This part of the setup is very useful to bring the system in resonance and perform a real-time check of the regime that is going to be measured.

A schematic image of the described setup is reported in Figure 5.9.

The detection part of the setup was the most investigated during my stay in Nice. It is important to point out that the measurements and the data analysis required the acquisition of the AC and DC component of the electric signal, separately.

Figure 5.10: Picture of the detection circuit.

Therefore, the low-noise photodiodes (FDGA05, Thorlabs) outputs are connected, each one, to a circuit that, through a

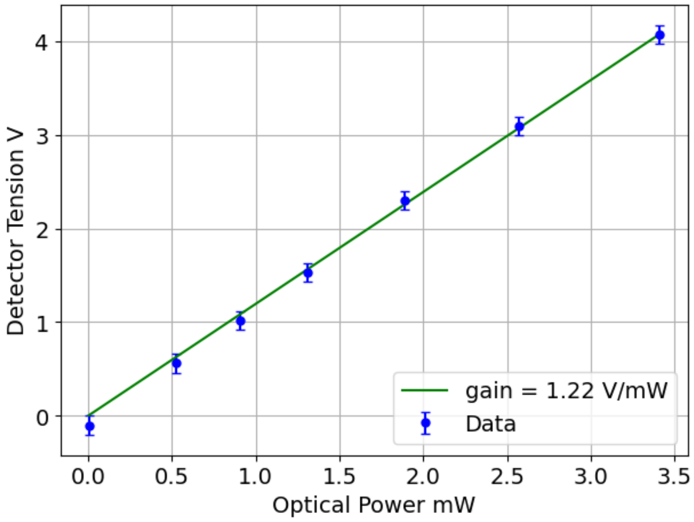

Figure 5.11: Gain characterization of the detector for the modes ±1

capacitor, separates the two components so that each of them can be properly amplified by a suitable operational amplifier (OpAmp). A picture of the photodiode acquisition circuit is shown in Figure 5.10.
It is important to bring to the reader's attention that the power of the first couple of modes generated in the comb (namely ±1) is much higher than the power of the second one (±2). It took several attempts to find the correct resistor and capacitor values to realize suitable detectors, characterized in terms of Signal to Noise Ratio (SNR). Even if they have the same scheme, some components are different in order to allow the detection of very different intensities. In fact the modes ±1 can reach intensities between 100 μW and 1 mW, while the modes ±2 typically stay below 100 μW. A characterization of the detector was required for both the AC and DC component. In the case of DC components, the output current was acquired at variance of the input power. In Figure 5.11 and Figure 5.12 we show the results of the characterization performed to obtain the DC component gain, respectively for modes ±1 and ±2.

Similarly, the characterization for the AC component has been performed using the ESA to observe the increase of the noise power at the variance of the input power. An example of ESA noise trace is represented in Figure 5.13.

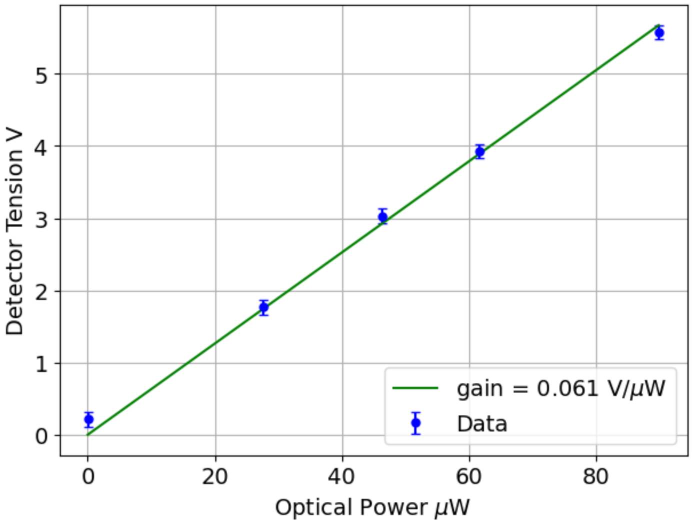

Figure 5.12: Gain characterization of the detector for the modes ±2

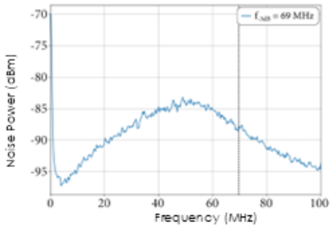

Figure 5.13: Noise Power as a function of the Frequency for the detector ±1

The results for the ±1 detector lead to a gain of 3 pW/mW (SNR 10 dB), while the ±2 detector has an AC gain of 85 pW/mW (SNR 6 dB for 100 μW), at a frequency of 4 MHz. Both the detectors are supplied with a 12 V battery.
In any setup configuration described, the DC component is acquired by a 4 channel, 8 bit oscilloscope terminated at 1 MΩ.
The first acquisition setup, as reported in Figure 5.14, enables the estimation of the correlation related only to two different detectors. The AC output of two detectors is connected to an analog subtractor, whose output is directly connected to the Electrical Spectrum Analyzer (ESA). Since the gain of the two detectors is not exactly the same, the most intense signal is attenuated, before the subtraction process, by means of a variable attenuator controlled by an Arduino hardware. The device parameters are set by a LabVIEW program allowing an attenuation up to 31 dB, by steps of 0.25 dB.

The correlation measurement implies acquiring the ESA trace at the same time as the DC component. The whole acquisition chain is entirely controlled by a LabVIEW program. The final acquisition chain, shown in Figure 5.15, that allows acquiring all the four channels simultaneously, in order to be able to study correlations between all the possible pairs of modes, implies the use of a second oscilloscope. In this case, it is a RTO1044 from Rohde & Schwarz, controlled, together with the DC oscilloscope, through a LabVIEW program. In this case there is no analog attenuation applied to any channel; every compensating step, including time delay, is performed in the data process.

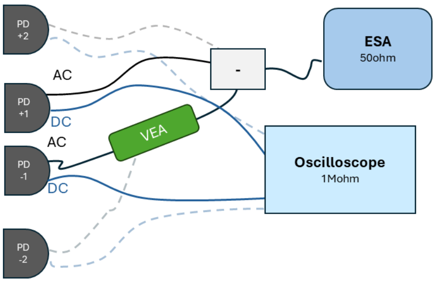

Figure 5.14: Sketch of the acquisition chain with the ESA

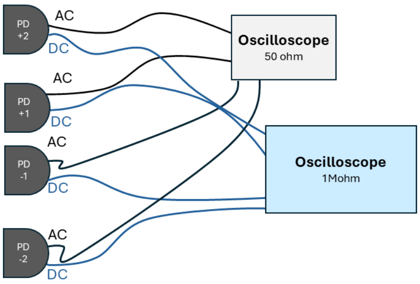

Figure 5.15: Sketch of the acquisition chain with two oscilloscopes

As already mentioned, the aim of the experiment is to evaluate if the correlations between the generated modes have a quantum nature. This characterization is performed in terms of shot noise (SN), meaning that if the noise on the correlated state is lower than the one expected from the laser noise, the state is sub-shot-noise, which is a quantum feature. Therefore, it is fundamental to acquire a reference of the laser shot noise so that it can be compared to the noise related to correlation measurement. This is the main reason why the chosen source, as reported at the beginning of this paragraph, must be shot-noise-limited. In fact, every correlation measurement is provided with a shot noise measurement, which relates the laser power to its noise. To perform this measurement the laser power is modified using the attenuator and collected through the same acquisition chain used for the correlation measurement. In Figure 5.16 a sketch of the shot noise measurement setup in the case of analog subtraction and ESA acquisition is reported in panel **a)**, while the direct measurement with the two oscilloscopes is shown in panel **b)**. It is worth clarifying that the shot noise measurement is collected separately for ±1 and ±2.

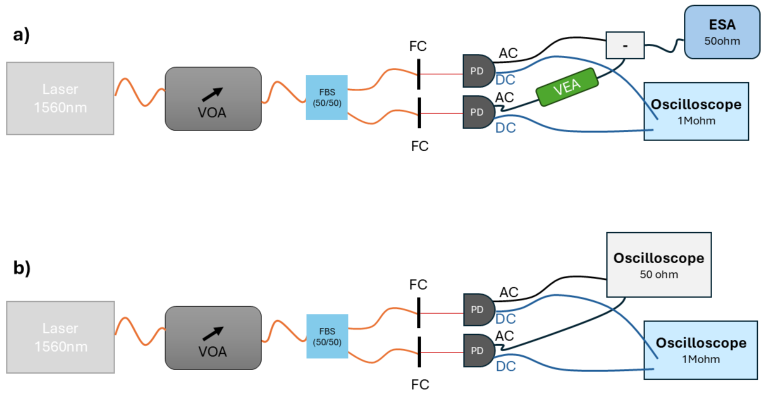

Figure 5.16: Sketch of the experimental setup for the shot noise measurement.

5.5 Experimental Procedure and Data Acquisition

After the description of the setup, I would like to give an insight into the procedure this experiment requires. As already mentioned, the measurement of correlations must be provided with a shot noise measurement. When the acquisition is performed with the ESA, the shot noise measurement is taken after the correlation one, because the real-time acquisition program allows monitoring the correlation value at variance of the Arduino variable attenuator, with the aim to maximize the correlation between the two modes. It is crucial that the shot noise measurement is collected with the same attenuation as the correlation measurement, otherwise the noise values could not be really comparable and the measured correlations would be compromised. Nevertheless, the acquisition with the ESA was only used as a double check while optimizing the oscilloscope acquisition. In fact, the ESA acquisition gave easy access to a trusted correlation value, which was suitable to test the post-processing procedure of the data acquired with the oscilloscope. It was very useful to perform the transition to the 4-channel acquisition with the oscilloscope. Therefore, all the results reported in this chapter are obtained with the acquisition chain described in Figure 5.15.

To perform shot noise measurements, the intensity (in terms of AC and DC) is acquired as a function of the optimal input power, as described by Figure 5.16. A few intensities are acquired in order to obtain a linear fit that will be used to extrapolate the expected shot noise value for each correlation measurement intensity.

To acquire correlation measurements, it is important to check the stability of the TEC temperature and set the laser to its central wavelength. After switching the amplifier on, a fine alignment using the piezoelectric stage must be performed at the beginning of each session of measurements. In this case, the power meter placed after the flip mirror can be used to improve the alignment. It is important to check the light polarization as well as a second polarizer control. The comb is generated by gently moving the laser wavelength, in the right direction, to the resonant one. The flip mirror should be in vertical position, so that the power meter can measure the output intensity, which is decreasing while tuning the resonance, while on the OSA a comb should appear. Once the comb is generated, the mirror can be flipped so that the light impinges on the detectors and can be acquired. During the acquisition the DC component is acquired by the oscilloscope in a text file, while the AC component is saved in a separate one according to the chosen acquisition chain. To create a dataset, the AC component is saved 50 times for every input wavelength.

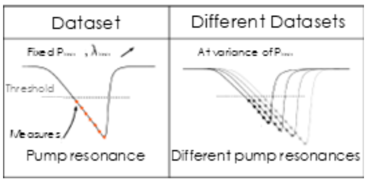

Figure 5.17: Figurative representation of the datasets acquisition.

Each dataset is collected at variance of the input wavelength, meaning at variance of the ring resonance. This condition is obtained approaching the minimum power, which implies maximum resonance, while the different datasets are acquired performing the same procedure at different input power values. Figure 5.17 might be of use to give the reader a better idea of the datasets acquisition. Both the acquisitions enable access to the whole spectrum of the Fourier transform of the signal, but the correlation is calculated only for the frequency where the detectors have a minimum of noise, which in our case corresponds to 4 MHz.

5.6 Data Analysis and Results

In this section the analysis procedure and the main results of the experiment are reported. First of all, let's remark that the oscilloscope traces are acquired in the time domain. The investigated correlations are expressed in terms of noise on the intensity difference, as already performed in some other works[6] [7]. Since the analysis we are performing is meant to be in the frequency domain, the first step of the post-processing procedure is to apply a Fourier transform. The transformed traces require some data processing to result less noisy, so the 50 acquisitions are averaged and then a moving average (involving about the 4% of data) is performed. This procedure was the best one among several attempts, whose results were compared to the ESA ones. In fact, the ESA output is subject to an internal filtering while the transformed data of the oscilloscope have no filtering, so the aim is to make the traces as similar as possible.

As already explained, every dataset is provided with its shot noise measurement. In this context, from the Fourier-transformed traces, we calculate the AC noise corresponding to the DC value. A linear fit is performed so that it is possible to evaluate the shot noise level for every correlation measurement intensity. Such a procedure is performed for each channel. An example of the outcomes is reported in Figure 5.18, where the transformed traces are reported on the left and the shot noise fit on the right.

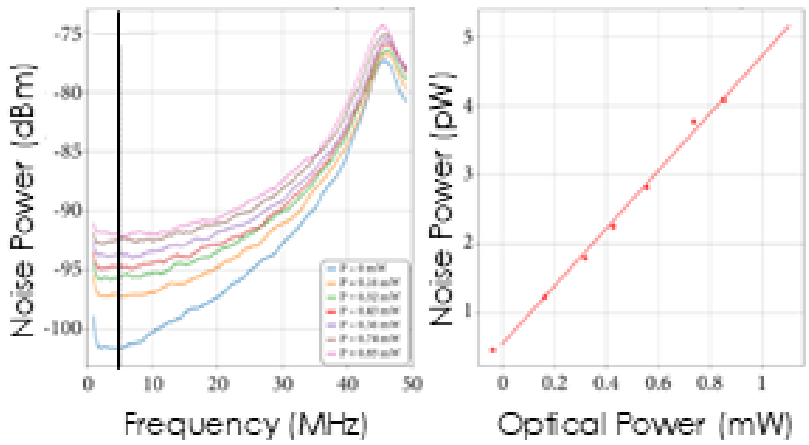

Figure 5.18: Averaged and smoothed Fourier-transformed traces on the left, shot noise measured at 4 MHz (in linear scale) on the right.

All the noise data (as well as the correlation ones) are then rescaled in dB units. As already explained in the setup description, the 4-channel acquisition with the oscilloscope has no attenuator to balance the channels. Keeping in mind that correlations are calculated between couples of channels, in this configuration also the balancing is performed in post processing by multiplying one of the two channels by a complex number $\beta = |\beta| e^{i\phi}$. By separately adjusting the values of $|\beta|$ and ϕ it is possible to compensate for amplitude and phase

6: [64] Avik Dutt et al., *Physical Review Applied*, p. 044005 (3), (2015)

7: [68] Yichen Shen et al., *Optica*, pp. 302–308 (12), (2025) unbalancing. This can be a compensation both for intensity imbalance and slightly different cable lengths.

The first step to calculate correlation between two channels is the calculation of the difference of the two Fourier transforms:

$$\mathscr{F}^{(i)}_{diff} = \mathscr{F}^{(i)}_{ch1} - \beta\mathscr{F}^{(i)}_{ch2}$$

where ch1 and ch2 could be any acquired channel (+1, +2, -1, -2). The index i represents the fact that the subtraction is performed for the single traces simultaneously acquired on the two different channels, while the average is performed as a second step.

The square modulus of the difference represents the variable we use to discriminate whether the correlation is quantum or not.

$$Var^{(i)}_{diff} = |\mathscr{F}^{(i)}_{diff}|^2 = \Re\left(\mathscr{F}^{(i)}_{diff}\right)^2 + \Im\left(\mathscr{F}^{(i)}_{diff}\right)^2$$

To effectively measure the quantum correlations, we perform an average over the 50 processed traces and transform the power in dB. The reason why we use the logarithmic scale is that, to compare the noise level to the shot noise one, it is enough to perform a subtraction

$$corr = Var^{dB}_{diff} - Var^{dB}_{SN}$$

where Var^{dB}_{diff} represents the modulus squared of the transformed traces, averaged and in dB scale, and Var^{dB}_{SN} represents the shot noise level averaged and in dB scale as well. If the obtained value is negative, then the correlations are sub-shot-noise.

Let's point out that the parameter β is estimated in series of loops where the amplitude and phase are optimized separately. The aim of the loop is to minimize the value of the calculated correlations. Three different loops are performed, each one with a narrower but thicker range of values triggered by the minimum value found in the previous loop. It is important to mention that once β is optimized for each correlation measurement, the same value is applied to the related shot noise measurement, so that the comparison is consistent.

Before showing the results obtained from this analysis, it is important to mention that the input power value affects the resonance shape, an idea of this phenomenon is represented in Figure 5.17. Therefore, the resonant modes wavelength could slightly change, as well as their FSR. In this case the investigated input power ranges between 1.08 and 1.18 times the threshold power P_{th} (that we repeat to be around 50 mW for this device) and the generated first modes (±1) space 14 FSR of the non-amplified spectrum from the pump frequency. Most of the results reported in this section have been published on Physical Review Research [8].

By changing the input power we calculate the correlations between the generated modes. Let's start by investigating the behavior of the bipartite regime, by calculating the correlation of ±1 and ±2.

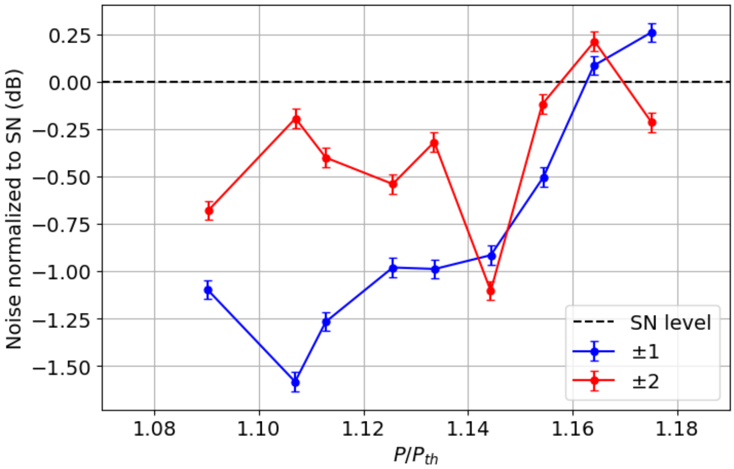

Figure 5.19: Correlations calculated for the couple of modes ±1 (blue) and ±2 (red). Dashed line represents SN level.

The results of the analysis are reported in Figure 5.19. The modes ±1 show quite strong correlations at lower powers. Such correlations seem to reduce as the pump power increases. Also the modes ±2 have a similar behavior, even if the minimum of noise is higher than the one related to the first two modes. This could be a consequence of the SNR of the detector, which is lower with respect to the one of the detectors for ±1. We could interpret this behavior as a passage from the bipartite to the multipartite regime. In fact, according to theory, in a multipartite regime we expect entanglement to be shared not only between symmetrical modes, but among any of their possible correlations.

Before moving forward to the crossed-modes analysis, I would like to mention that, to the best of my knowledge, we performed the first experimental measurements of the couple ±2 generated with such a device.

A similar analysis was performed for the other couples of modes. Of course, according to theory, it is possible to generate more symmetrical modes, but in these acquisitions we

[8] [69] Adrien Bensemhoun et al., *Physical Review Research*, p. 033173 (7), (2025)

chose a range of power in which the generation of ±3 was negligible, so that with the current setup and acquisition chain we are not missing any quantum correlation.

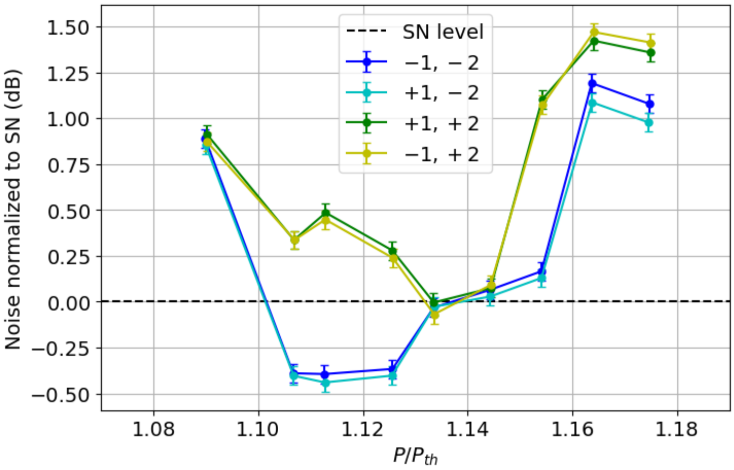

Figure 5.20: Correlations calculated for the couple of modes $-1, -2$ (blue) and $+1, -2$ (cyan), $-1, -2$ (green) and $-1, +2$ (yellow). Dashed line represents SN level.

The results of the crossed-modes analysis are reported in Figure 5.20. The first observable fact is that for the lowest power, all the correlations are above the SN level, giving space to the interpretation that the multipartite regime has yet to be reached. In the range between 1.1 and 1.15 times P_{th} we can observe a decrease of the noise values, meaning an increase in quantum correlations. The four curves present similar behavior even though the actual noise values are different. This could be due to an asymmetry of the dispersion inside the ring waveguides or some imprecision in the optical setup. After the decreasing range, we can observe an increment of correlation, from $1.15P_{th}$. We experimentally observed that in this region the modes ±3 begin to appear, thus reducing the correlation between symmetrical and non-symmetrical modes. Therefore, the description of the data in this range is incomplete in this case. In the referred work some further analysis of these data is presented. An operator $\hat{C}$ that represents a constant of the system evolution is introduced, this can be useful to describe the overall behavior of the quantum correlations. The reason why I chose not to report such an analysis is because it was performed after my leaving.

5.7 Conclusions

The work presented in these few pages is just the result of what I have studied and done in the six months I have been a guest at the Université de la Côte d'Azur. Much more work has been done before and after my presence in the lab, I decided to report the results we obtained while I was there. In these months we managed to assemble proper detectors for the characterization of sub-shot-noise measurements and implement the four-channel acquisition with an oscilloscope. These engineering procedures required a lot of time and effort, and finally allowed us to realize the measurement of the quantum correlations of the modes ±1 and for the first time of the modes ±2. Moreover, we gave a first characterization of the passage from the bipartite to the multipartite regimes in terms of quantum correlations. More detailed procedures concerning the characterization and a finer analysis are reported in the PhD thesis of Adrien Bensemhoun, the PhD student I assisted during my stay.

6 Conclusion and Future Perspectives

In this work a first experimental realization of a hybrid interferometric detector was presented. Such a detector is similar to a standard homodyne detector with the main difference that two photon-number-resolving devices are used to collect the interference signal. In this specific case we chose to use silicon photomultipliers (SiPMs), which we have already demonstrated being suitable to reconstruct photon number statistics and recognize sub-shot-noise photon-number correlations. At first, we characterized the intensity parameters in order to be able to mimic the standard homodyne behavior. In this context, the main issue is the intensity required to generate enough mutual information, but also the limitation due to the detectors' sensitivity. All these results are reported in Chapter 2, where we also characterized the possible post-processing procedure in case of binary phase shift keying (BPSK) of coherent states. After comparing three different post-processing strategies, we used the best one to mimic a communication channel between two parts, where a third part can steal information from the channel losses. All these results were compared to a simulated standard homodyne detector characterized by the same experimental parameters. Moreover, in Chapter 3, we tried to implement a more complex phase encoding, based on the use of four phases. Even though this is just the third chapter, this experiment has been performed at the end of my PhD, so the reported results are just the fruit of a preliminary study of feasibility. Nevertheless, in this chapter we characterized the phase noise and implemented a first 4-phase shift measurement as a function of the channel losses. Such a measurement has been compared to the BPSK, to understand in which limit it could bring advantages. Moreover, to make the results more consistent, we compared them with the expectation of a standard homodyne detection characterized by the same experimental parameters.

All results obtained in these two chapters involved the use of visible wavelengths, a spectral region in which SiPMs are very sensitive. This procedure is suitable for a proof-of-principle demonstration, as well as aiming at some kind of free space communication, but we are also interested in investigating whether our receiver could be suitable for telecom-compliant infrastructures. To this aim, we realized an up-conversion receiver to test the suitability of SiPMs in this context. The main idea here is to generate laser pulses in the C band (1550 nm), where the SiPMs are blind, and to up-convert the generated pulses by means of a nonlinear process (sum frequency generation) to 620 nm. We manipulated the beam at telecom wavelengths and managed to reconstruct the modulations with the detectors. In this experiment we did not test the hybrid detector, just the single SiPMs, in a direct detection scheme to prove their sensitivity to an up-converted beam. Also in this case, the experiment performed is meant to be a proof of principle, that still requires some optimization to be implemented in a real communication channel, but the obtained results are promising.

The fifth chapter is what I call an "extra chapter", since it had nothing to do with the project presented so far. In fact, it is about the six-month period spent in Nice (France), where I assisted another PhD student in his work. During this period I worked on the characterization of the quantum correlations among the frequency combs generated by a silicon nitride micro-ring resonator at different intensity regimes. Most part of the work was the realization of the four-channel acquisition chain.

To summarize, the main project of my PhD was the proof-of-principle realization of a hybrid interferometric detector based on SiPMs. The results obtained so far are promising, even though there is still a lot of work to do before being able to implement such a device on a real communication channel. First of all, it is necessary to implement a real-time analysis;

in this context we are already performing an analytic study to estimate a sufficient number of samples to reconstruct the encoded state. Such a result is very important to understand the maximum transmission rate our device provides. Such a repetition rate right now is limited by the acquisition chain, that is going to be modified. We have demonstrated that, also for this device, a multiphase encoding could bring advantages in terms of mutual information, but the phase noise currently affecting the detection represents the main limit to this implementation. Some improvements in this direction are definitely required to achieve results compatible with the ones already present in the literature for homodyne detection. Finally, we proved the suitability of SiPMs for standard telecom wavelengths, but also in this case some further improvements are required in order to be fully compliant with the current infrastructures. First of all, the implementation of optical fiber propagation that involves the generation of a completely different setup. Maybe integrated optics could be the final goal for our device.

In other words, this work opens the way to many possible implementations of such a high-potential device, but still there is much work to do in order to make it feasible in practical applications.

A List of publications

The list of articles published during my PhD is reported below.[1].

Published papers mentioned in this manuscript:

- ASSESSING A BINARY QUANTUM CHANNEL EXPLOITING A SILICON PHOTOMULTIPLIER BASED HYBRID RECEIVER
  A.Sanvito, S. Cassina*, M. Lamperti, M. N. Notarnicola, S. Olivares, A. Allevi
  Optics Express, Volume 32, Issue 22, Pages 39846 – 3985921, October 2024
- MULTIPARTITE QUANTUM CORRELATED BRIGHT FREQUENCY COMBS
  A. Bensemhoun, S. Cassina, C. Gonzelez-Arciniegas, M. F. Melalkia,, G. Patera, J. Faugier-Tova, Q. Wilmart, S. Olivier, A. Zavatta, A. Martin, J. Etesse, L. Labonté, O. Pfister, V. D'Auria* and S. Tanzilli
  Physical Review Research, Volume 7, Article number 033137, 2025
- SUM-FREQUENCY-BASED PHOTON-NUMBER-RESOLVING DETECTOR FOR TELECOM WAVELENGTHS
  Silvia Cassina*, Alex Pozzoli, Guglielmo Vesco, Marco Lamperti, Marco Marangoni, and Alessia Allevi
  Submitted to APL Photonics

---

[1] * stands for "corresponding author"

- Statistical characterization of discrete amplitude-modulated coherent states at telecom wavelengths by means of an upconversion-based photon-number-resolving detector
  Silvia Cassina*, Alex Pozzoli, and Alessia Allevi*
  Accepted by Optics Express

Published papers referred to other projects, not mentioned in the manuscript:

- On the use of superthermal light for imaging applications
  S. Cassina*, G. Cenedese, M. Lamperti, M. Bondani, A. Allevi
  Physics Letters, Section A: General, Atomic and Solid State Physics, Volume 49528, January 2024, Article Number 129300
- Application of superthermal light to imaging and quantum communication protocols
  S. Cassina, G. Cenedese, M. Bondani, A. Allevi*
  International Journal of Quantum Information, Volume 22, Issue 61, September 2024, Article number 2450025
- Speckled-speckle field as a resource for imaging techniques
  S. Cassina, G. Cenedese, A. Allevi*, M. Bondani
  Scientific Reports, Volume 14, Issue 1December 2024, Article number 15161
- On the application of a Silicon photomultiplier-based receiver for binary phase-shift-keying protocols
  S. Cassina, M. N. Notarnicola, S. Olivares, A. Allevi*
  Physics Letters, Section A: General, Atomic and Solid State Physics, 2025, Volume 541, Article number 130403
- Implementation of a hybrid SiPM receiver for applications to continuous-variable quantum key distribution with binary modulation
  A.Mazzocchi, M. N. Notarnicola, S. Cassina, M. Lamperti, S. Olivares and A. Allevi*
  submitted to International Journal of Quantum Information

Bibliography

Here are the references in citation order.

[1] Wei Luo et al. ‘Recent progress in quantum photonic chips for quantum communication and internet’. In: *Light: Science & Applications* 12.1 (2023), p. 175 (cited on page v).

[2] Thu Ha Dao et al. ‘Single-photon detectors for quantum integrated photonics’. In: *Photonics*. Vol. 12. 1. MDPI. 2024, p. 8 (cited on page v).

[3] Stefano Pirandola et al. ‘Advances in quantum cryptography’. In: *Advances in optics and photonics* 12.4 (2020), pp. 1012–1236 (cited on pages v, 9).

[4] Jan Provazník et al. ‘Benchmarking photon number resolving detectors’. In: *Opt. Express* 28.10 (May 2020), pp. 14839–14849. DOI: `10.1364/OE.389619` (cited on page v).

[5] Silvia Cassina et al. ‘Exploiting the wide dynamic range of silicon photomultipliers for quantum optics applications’. In: *EPJ Quantum Technology* 8.1 (2021), p. 4 (cited on page v).

[6] Marco Cattaneo, Matteo G. A. Paris, and Stefano Olivares. ‘Hybrid quantum key distribution using coherent states and photon-number-resolving detectors’. In: *Phys. Rev. A* 98 (1 July 2018), p. 012333. DOI: `10.1103/PhysRevA.98.012333` (cited on pages vi, 32).

[7] Cristpher C. Gerry and Peter L. Knight. *Introductory Quantum Optics*. 2004 (cited on page 2).

[8] Thomas M. Cover and Joy A. Thomas. *Quantum Communications*. 2005 (cited on pages 3, 31).

[9] Gianfranco Cariolaro. *Quantum Communications*. 2015 (cited on page 3).

[10] Stefano Olivares. *Lecture notes on quantum computing*. 2021 (cited on page 3).

[11] Alexander Semenovich Holevo. ‘Bounds for the quantity of information transmitted by a quantum communication channel’. In: *Problemy Peredachi Informatsii* 9.3 (1973), pp. 3–11 (cited on page 7).

[12] Fabian Laudenbach et al. ‘Continuous-Variable Quantum Key Distribution with Gaussian Modulation—The Theory of Practical Implementations (Adv. Quantum Technol. 1/2018)’. In: *Advanced Quantum Technologies* 1.1 (2018), p. 1870011. DOI: `https://doi.org/10.1002/qute.201870011` (cited on page 7).

[13] Frédéric Grosshans and Philippe Grangier. ‘Continuous Variable Quantum Cryptography Using Coherent States’. In: *Phys. Rev. Lett.* 88 (5 Jan. 2002), p. 057902. DOI: `10.1103/PhysRevLett.88.057902` (cited on page 10).

[14] Stefano Olivares et al. ‘Homodyne detection as a near-optimum receiver for phase-shift-keyed binary communication in the presence of phase diffusion’. In: *Phys. Rev. A* 87 (5 May 2013), p. 050303. DOI: `10.1103/PhysRevA.87.050303` (cited on page 10).

[15] Stefano Olivares. ‘Introduction to generation, manipulation and characterization of optical quantum states’. In: *Physics Letters A* 418 (2021), p. 127720. DOI: `https://doi.org/10.1016/j.physleta.2021.127720` (cited on pages 10, 28).

[16] Alessia Allevi et al. ‘Homodyne-like detection scheme based on photon-number-resolving detectors’. In: *International Journal of Quantum Information* 15.08 (2017), p. 1740016. DOI: `10.1142/S0219749917400160` (cited on pages 11, 27).

[17] Graciana Puentes et al. ‘Bridging Particle and Wave Sensitivity in a Configurable Detector of Positive Operator-Valued Measures’. In: *Physical Review Letters* 102.8 (2009), p. 080404 (cited on page 11).

[18] Gaia Donati et al. ‘Observing optical coherence across Fock layers with weak-field homodyne detectors’. In: *Nature communications* 5.1 (2014), p. 5584 (cited on page 11).

[19] Matteo Bina et al. ‘Homodyne-like detection for coherent state-discrimination in the presence of phase noise’. In: *Optics Express* 25.9 (2017), pp. 10685–10692 (cited on page 12).

[20] John G Skellam. ‘The frequency distribution of the difference between two Poisson variates belonging to different populations’. In: *Journal of the Royal Statistical Society Series A: Statistics in Society* 109.3 (1946), pp. 296–296 (cited on page 12).

[21] Matteo GA Paris. ‘The modern tools of quantum mechanics: A tutorial on quantum states, measurements, and operations’. In: *The European Physical Journal Special Topics* 203.1 (2012), pp. 61–86 (cited on page 13).

[22] Claudio Piemonte. ‘A new silicon photomultiplier structure for blue light detection’. In: *Nuclear Instruments and Methods in Physics Research Section A: Accelerators, Spectrometers, Detectors and Associated Equipment* 568.1 (2006), pp. 224–232 (cited on page 15).

[23] Ziraddin Sadygov, Azer Sadigov, and Sergey Khorev. ‘Silicon photomultipliers: Status and prospects’. In: *Physics of Particles and Nuclei Letters* 17.2 (2020), pp. 160–176 (cited on page 15).

[24] Marco Ramilli et al. ‘Photon-number statistics with silicon photomultipliers’. In: *Journal of the Optical Society of America B* 27.5 (2010), pp. 852–862 (cited on page 15).

[25] Itai Afek et al. ‘Quantum state measurements using multipixel photon detectors’. In: *Physical Review A—Atomic, Molecular, and Optical Physics* 79.4 (2009), p. 043830 (cited on page 16).

[26] Giovanni Chesi et al. *Optimizing silicon photomultipliers for quantum optics Sci.* 2019 (cited on page 18).

[27] Alberto Sanvito et al. ‘Assessing a binary quantum channel exploiting a silicon photomultiplier based hybrid receiver’. In: *Optics Express* 32.22 (2024), pp. 39846–39859 (cited on pages 18, 27).

[28] Robert W. Boyd. *Nonliner optics*. 2008 (cited on pages 19, 77).

[29] John H Marburger. 'Self-focusing: theory'. In: *Progress in quantum electronics* 4 (1975), pp. 35–110 (cited on page 23).

[30] Silvia Cassina et al. 'On the application of a Silicon photomultiplier-based receiver for binary phase-shift-keying protocols'. In: *Physics Letters A* 541 (2025), p. 130403 (cited on page 27).

[31] János A Bergou. 'Discrimination of quantum states'. In: *Journal of Modern Optics* 57.3 (2010), pp. 160–180 (cited on page 27).

[32] Carl W Helstrom. 'Quantum detection and estimation theory'. In: *Journal of Statistical Physics* 1.2 (1969), pp. 231–252 (cited on page 27).

[33] Shuro Izumi et al. 'Displacement receiver for phase-shift-keyed coherent states'. In: *Physical Review A—Atomic, Molecular, and Optical Physics* 86.4 (2012), p. 042328 (cited on page 27).

[34] Christian R Müller and Christian Marquardt. 'A robust quantum receiver for phase shift keyed signals'. In: *New Journal of Physics* 17.3 (2015), p. 032003 (cited on page 27).

[35] Michele N Notarnicola and Stefano Olivares. 'Employing weak-field homodyne detection for quantum communications'. In: *arXiv preprint arXiv:2405.14310* (2024) (cited on page 31).

[36] Ziwen Pan et al. 'Secret-key distillation across a quantum wiretap channel under restricted eavesdropping'. In: *Physical Review Applied* 14.2 (2020), p. 024044 (cited on page 31).

[37] Michele N Notarnicola et al. 'Optimizing state-discrimination receivers for continuous-variable quantum key distribution over a wiretap channel'. In: *New Journal of Physics* 25.10 (2023), p. 103014 (cited on page 32).

[38] Stefano Olivares, Alessia Allevi, and Maria Bondani. 'On the role of the local oscillator intensity in optical homodyne-like tomography'. In: *Physics Letters A* 384.17 (2020), p. 126354 (cited on page 39).

[39] Matthew T DiMario and Francisco E Becerra. 'Robust measurement for the discrimination of binary coherent states'. In: *Physical review letters* 121.2 (2018), p. 023603 (cited on page 41).

[40] Michele N Notarnicola, Matteo GA Paris, and Stefano Olivares. 'Hybrid near-optimum binary receiver with realistic photon-number-resolving detectors'. In: *Journal of the Optical Society of America B* 40.4 (2023), pp. 705–714 (cited on page 41).

[41] Matthew T DiMario et al. 'Optimized communication strategies with binary coherent states over phase noise channels'. In: *npj Quantum Information* 5.1 (2019), p. 65 (cited on page 49).

[42] Francisco E Becerra et al. 'Experimental demonstration of a receiver beating the standard quantum limit for multiple nonorthogonal state discrimination'. In: *Nature Photonics* 7.2 (2013), pp. 147–152 (cited on page 49).

[43] Francisco E Becerra, Jingyun Fan, and Alan Migdall. 'Implementation of generalized quantum measurements for unambiguous discrimination of multiple non-orthogonal coherent states'. In: *Nature communications* 4.1 (2013), p. 2028 (cited on page 49).

[44] Denis Sych and Gerd Leuchs. 'Coherent state quantum key distribution with multi letter phase-shift keying'. In: *New Journal of Physics* 12.5 (2010), p. 053019 (cited on page 49).

[45] Michele N Notarnicola et al. 'Probabilistic amplitude shaping for continuous-variable quantum key distribution with discrete modulation over a wiretap channel'. In: *IEEE Transactions on Communications* 72.1 (2023), pp. 375–386 (cited on page 50).

[46] Giulio Colavolpe et al. 'Impact of phase noise and compensation techniques in coherent optical systems'. In: *Journal of Lightwave Technology* 29.18 (2011), pp. 2790–2800 (cited on page 50).

[47] WeiJun Zhang et al. 'NbN superconducting nanowire single photon detector with efficiency over 90% at 1550 nm wavelength operational at compact cryocooler temperature'. In: *Science China Physics, Mechanics & Astronomy* 60.12 (2017), p. 120314 (cited on page 62).

[48] Joe C Campbell. 'Recent advances in telecommunications avalanche photodiodes'. In: *Journal of Lightwave Technology* 25.1 (2007), pp. 109–121 (cited on page 62).

[49] Enrico Pomarico et al. 'Room temperature photon number resolving detector for infared wavelengths'. In: *Optics express* 18.10 (2010), pp. 10750–10759 (cited on page 62).

[50] Kun Huang et al. 'Mid-infrared photon counting and resolving via efficient frequency upconversion'. In: *Photonics Research* 9.2 (2021), pp. 259–265 (cited on page 62).

[51] JL Debethune. 'Quantum correlation functions for radiation fields with stationary independent modes'. In: *Il Nuovo Cimento B (1971-1996)* 12.1 (1972), pp. 101–117 (cited on page 62).

[52] Pavel Chmela, Zbigniew Ficek, and Stanislaw Kielich. 'Classical theory of non-degenerate sum-frequency generation by incoherent nonlinear optical mixing of coherent and chaotic radiations: I. General solution'. In: *Czechoslovak Journal of Physics B* 39.5 (1989), pp. 509–528 (cited on page 62).

[53] Andrea Villa et al. 'Broadly tunable mid-infrared femtosecond pulses directly generated by an optical parametric amplifier'. In: *OSA Continuum* 4.11 (2021), pp. 2837–2844 (cited on page 63).

[54] Francesco Gucci et al. 'Spectral broadening of μJ-level pulses around 8 μm in a Germanium-based multi-pass scheme'. In: *Optics Express* 32.27 (2024), pp. 48599–48609 (cited on page 64).

[55] Leonard Mandel and Emil Wolf. *Optical Coherence and Quantum Optics*. 1995 (cited on page 68).

[56] Alessia Allevi and Maria Bondani. 'Nonlinear and quantum optical properties and applications of intense twin-beams'. In: *Advances In Atomic, Molecular, and Optical Physics* 66 (2017), pp. 49–110 (cited on page 68).

[57] Werner Vogel. 'Nonclassical correlation properties of radiation fields'. In: *Physical review letters* 100.1 (2008), p. 013605 (cited on page 68).

[58] Roy J Glauber. 'The quantum theory of optical coherence'. In: *Physical Review* 130.6 (1963), p. 2529 (cited on page 69).

[59] Alessia Allevi, Stefano Olivares, and Maria Bondani. 'Measuring high-order photon-number correlations in experiments with multimode pulsed quantum states'. In: *Physical Review A—Atomic, Molecular, and Optical Physics* 85.6 (2012), p. 063835 (cited on page 69).

[60] Frédéric Grosshans et al. 'Quantum key distribution using gaussian-modulated coherent states'. In: *Nature* 421.6920 (2003), pp. 238–241 (cited on page 75).

[61] Anthony Leverrier and Philippe Grangier. 'Unconditional security proof of long-distance continuous-variable quantum key distribution with discrete modulation'. In: *Physical Review Letters* 102.18 (2009), p. 180504 (cited on page 78).

[62] Shouvik Ghorai et al. 'Asymptotic security of continuous-variable quantum key distribution with a discrete modulation'. In: *Physical Review X* 9.2 (2019), p. 021059 (cited on page 78).

[63] Laurent Labonté et al. 'Integrated photonics for quantum communications and metrology'. In: *PRX Quantum* 5.1 (2024), p. 010101 (cited on page 88).

[64] Avik Dutt et al. 'On-chip optical squeezing'. In: *Physical Review Applied* 3.4 (2015), p. 044005 (cited on pages 88, 101).

[65] Adrien Bensemhoun et al. 'Multipartite entanglement in bright frequency combs out of microresonators'. In: *Physics Letters A* 493 (2024), p. 129272 (cited on page 90).

[66] Maxim Karpov et al. 'Dynamics of soliton crystals in optical microresonators'. In: *Nature Physics* 15.10 (2019), pp. 1071–1077 (cited on page 92).

[67] Yanne K Chembo, Elham Heidari, and Curtis R Menyuk. 'A perspective on nonlinear, microwave, and quantum photonics with Kerr microcombs'. In: *Applied Physics Letters* 123.24 (2023) (cited on page 92).

[68] Yichen Shen et al. 'Strong nanophotonic quantum squeezing exceeding 3.5 dB in a foundry-compatible Kerr microresonator'. In: *Optica* 12.3 (2025), pp. 302–308 (cited on page 101).

[69] Adrien Bensemhoun et al. 'Multipartite quantum correlated bright frequency combs'. In: *Physical Review Research* 7.3 (2025), p. 033173 (cited on page 103).